THE EFFECT OF ROCK PROPERTIES ON HYDRAULIC FRACTURE CONDUCTIVITY IN THE EAGLE FORD AND FAYETTEVILLE SHALES

A Thesis

by

TIMOTHY ARTHUR JANSEN

Submitted to the Office of Graduate and Professional Studies of
Texas A&M University
in partial fulfillment of the requirements for the degree of

MASTER OF SCIENCE

Chair of Committee,	Ding Zhu
Committee Members,	A. Daniel Hill
	Fredrick M. Chester
Head of Department,	A. Daniel Hill

December 2014

Major Subject: Petroleum Engineering

ABSTRACT

Hydraulic fracture treatments are used in low permeability shale reservoirs in order to provide highly conductive pathways from the reservoir to the wellbore. The success of these treatments is highly reliant on the created fracture conductivity. Optimizing fracture designs to improve well performance requires knowledge of how fracture conductivity is affected by rock and proppant characteristics.

This study investigates the relationship between rock characteristics and laboratory measurements of propped and unpropped fracture conductivity of outcrop samples. These samples are from the Eagle Ford shale and the Fayetteville shale. Triaxial compression tests were performed on core specimens in order to determine the Young's Modulus and Poisson's Ratio of the outcrop samples. A combination of X-ray diffraction and Fourier transform infrared spectroscopy was used to determine the mineralogy. Profilometer surface scans were also performed to characterize the fracture topography.

The results from this study show that the main factors affecting fracture conductivity are closure stress and proppant characteristics (concentration, size, and strength). For unpropped fractures, the fracture topography is the main factor in determining fracture conductivity. The topography interaction of the two surfaces determines the fracture width. A higher Young's Modulus helps maintain this fracture width by resisting deformation as closure stress increases. For propped fractures, the most influential factor in determining fracture conductivity is proppant characteristics

(concentration, size, and strength). At a proppant monolayer placement, the major mechanism for conductivity loss is proppant embedment, leading to decreased fracture width. A higher Young's Modulus reduces the proppant embedment and better maintains fracture conductivity as closure stress increases. For a multilayer proppant pack concentration, the effect of rock characteristics is negligible compared to the effect of proppant pack characteristics.

DEDICATION

To my parents, without whom none of this would be possible, and to the all the nuclear engineers who delayed retirement, without whom none of this would be necessary.

ACKNOWLEDGEMENTS

I would like to thank my advisers Dr. Ding Zhu and Dr. Daniel Hill for guiding me in this work. I would especially like to thank them for taking on an unemployed nuclear engineer and converting me into an employed petroleum engineer during my graduate studies at Texas A&M University. I would also like to sincerely thank Dr. Fred Chester for being a member of my graduate committee.

I would like to thank Junjing Zhang, Anton Kamenov, Kathryn Briggs, and James Guzek for helping me and providing a solid foundation on which to start my work and Paola Puente, Dante Guerra, and Mark McGinley for being brave enough to continue this work when I leave.

I would like to thank John Maldonado for always being willing to help with a smile, even though he has a million other things to do. Without him, I would probably still be troubleshooting equipment and would never graduate.

I would like to thank RPSEA for their financial support and Ellington and Associates (now ALS Ellington) for providing us with XRD and FTIR testing at discounted pricing.

I would like to thank all of my friends and roommates, for always providing an irresistible distraction.

I would finally like to thank my little brother, who somehow found a Master of Science degree in Engineering that doesn't require a thesis, for teaching me that life isn't fair.

NOMENCLATURE

A	Area (mm^2 or in^2)
E	Young's Modulus of elasticity (psi or MPa)
F	Force (kN or lbf)
$k_f w_f$	Fracture conductivity (md-ft)
$(k_f w_f)_0$	Fracture conductivity at zero closure stress (md-ft)
l_0	Initial length (mm or in)
Δl	Change in length (mm or in)
ϵ	Strain (-)
$\epsilon_{axial}, \epsilon_a$	Axial Strain (-)
ϵ_C	Circumferential Strain (-)
ϵ_r	Radial Strain (-)
$\epsilon_{transverse}$	Strain perpendicular to axial load (-)
ν	Poisson's Ratio (-)
σ	Stress (psi or MPa)
$\sigma_1, \sigma_2, \sigma_3$	Principal Stresses (psi or MPa)
σ_c	Fracture closure stress (psi)
σ_D	Stress difference or Deviator Stress (psi or MPa)

TABLE OF CONTENTS

Page

LIST OF FIGURES

Page

LIST OF TABLES

Page

1. INTRODUCTION

1.1 Hydraulic Fracturing in Shale Reservoirs

Hydraulic fracturing has made extraction of the hydrocarbon resources from massive shale reservoirs both technically and economically feasible. Shale reservoirs are characterized by ultra-low permeability that prevents sufficient production without stimulation. The stimulation of choice in these low-permeability reservoirs is hydraulic fracturing. The primary objective of hydraulic fracturing is to provide a highly conductive pathway that connects a larger portion of the reservoir directly to the wellbore. A hydraulic fracturing treatment involves the pumping of a specifically-designed fluid at high pressures in order to breakdown the rock which causes fractures. A propping material is then pumped into the fractures in order to prevent the cracks from closing after the injection ends. In many cases, this material is simply sand grains. In higher pressure environments, a man-made ceramic proppant may be used instead of sands. The propping materials sometimes are resin-coated to prevent flow back during production. The measure of transmissibility of a fluid through a fracture is called fracture conductivity. Fracture conductivity is defined as the product of the fracture width and fracture permeability. The fracture conductivity is a major focus of designing fracture treatments because it is directly related to the well performance.

As the costs of fracture treatments climb into the millions of dollars per well, optimizing fracture design becomes extremely important in controlling well costs while still maintaining production improvements. It is possible to have an excessively large

hydraulic fracture conductivity, particularly in low-permeability shale reservoirs. After a certain point, the fracture conductivity is essentially infinite when compared to the bulk reservoir. This leads to unnecessary costs. Fracture designs are constantly being optimized to improve production and lower costs. As an example of a successful major fracture design change, in 1997, Barnett shale operators switched from massive cross-linked gel treatments using large proppant concentrations to high rate slick-water treatments with lower proppant concentrations. These slickwater treatments only slightly improved well performance, but decreased completion costs by 65% (Ketter et al., 2008). These learnings were then applied to other unconventional reservoirs such as the Eagle Ford and Fayetteville shale (Matthews et al., 2007). Fracture design optimization can have a major effect on completion cost, well performance, and the overall economic success or failure of a shale well.

In order to best design fracture treatments, the interactions between rock, proppant, and fluids must all be understood. Slickwater fracture treatments are still used today in the Fayetteville shale (Harpel et al., 2012). However, in the Eagle Ford, slickwater treatments were not completely successful initially (Mullen, 2010). The fracture designs had to be modified to include cross-linked gel stages with high proppant concentrations based on lessons learned in the Bakken shale (McNeil et al., 2011). With the designs modified to the specific reservoir, successful fracture treatments were possible in the Eagle Ford. This shows how reliant fracture design is on the rock characteristics, and why it is important to study the relationship between rock properties and fracture conductivity.

1.2 Eagle Ford Shale Overview

The Eagle Ford shale is an Upper Cretaceous (Cenomanian to Turonian) age unconventional reservoir in South Texas. It covers approximately 19,500 square miles and varies from 4,000 - 14,000 feet in depth and 50 – 300 feet in thickness (Quirein et al. 2013). The reservoir is capable of producing oil, condensates, and dry gas (Centurion, 2011). Although it is called a "shale", it is technically a highly calcareous mudstone (Shelley et al., 2012). The Eagle Ford can be subdivided into five vertical facies. These facies are named facies A through E (from bottom to top). Facies B in the lower Eagle Ford is rich in organic content, and is of great interest to producing companies (Donovan and Staerker, 2010). Even within a single facies, the highly heterogeneous nature of the Eagle Ford means that there can be significant differences in formation properties laterally over the scale of a horizontal well. For this reason, the horizontal differences in rock characteristics and fracture conductivity were the focus of this portion of the study.

Eagle Ford facies B outcrop samples were obtained from a road cut of US Highway 90 west of Comstock, Texas. The samples were taken from seven points along the outcrop with around 100 to 200 feet between each of the points. Overall, the samples cover a 1,015 feet horizontal stretch of Facies B. Figure 1 shows the highway cut that the samples were taken from.

Figure 1 - Eagle Ford outcrop sample location

1.3 Fayetteville Shale Overview

The Fayetteville Shale is a Mississippian-age shale reservoir in the Arkoma Basin of Northern Arkansas. It is a geological equivalent to the Barnett Shale in Texas. Figure 2 shows the location of the Fayetteville shale. The formation varies in thickness from 50 to 550 feet and varies in depth from 1500 to 6500 feet. The Fayetteville shale reservoir is divided into three major vertical sections: the Upper, Middle, and Lower Fayetteville. The Lower Fayetteville is further divided into the LFAY, FL2, and FL3 zones and is rich in natural fractures. The FL2 zone is the main target interval for

operators because it has the lowest clay content and the highest gas porosities of the Lower Fayetteville (Harpel et al, 2012). The FL2 and FL3 zones are the zones of interest for this research. Outcrop samples of FL2 and FL3 were provided by Southwestern Energy. The main focus of the Fayetteville experiments is to study how the vertical heterogeneity across sub-layers affects the fracture conductivity.

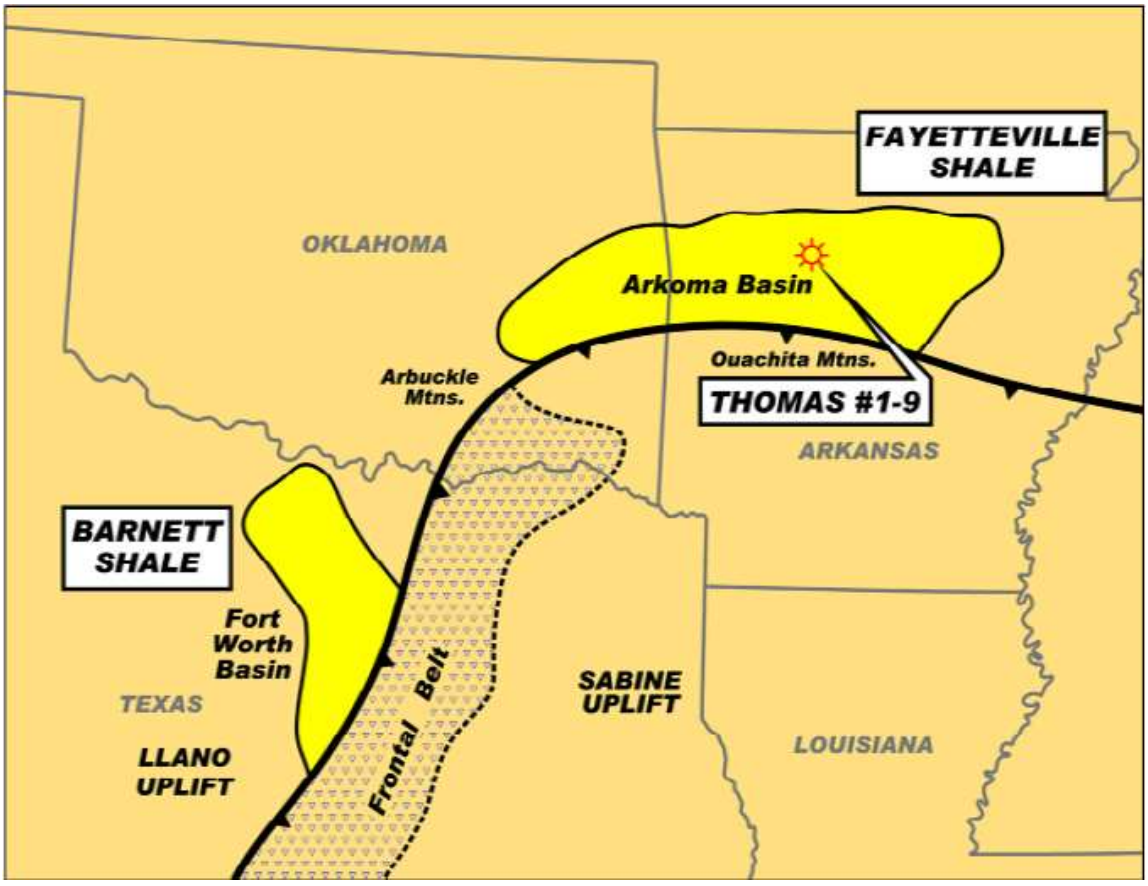

Figure 2 - Map of the Fayetteville shale location in the Arkoma Basin (Harpel et al, 2012)

1.4 Literature Review

The ultimate goal of any hydraulic fracture treatment is to create a flow path with sufficient fracture conductivity to increase well productivity. The conductivity of a hydraulic fracture is affected by many interrelated factors such as closure stress, temperature, proppant characteristics including strength, size, and areal concentration, fracture surface characteristics such as rock elastic properties, surface roughness, asperity size, strength, and distribution, proppant embedment resistance, and mineral composition. The fluids used in a fracture treatment can have a great effect on fracture conductivity due to proppant transport capabilities and rock-fluid interactions. It is virtually impossible to isolate the effect of any one variable on fracture conductivity from field studies. This results in literature containing decades-worth of fracture conductivity-related laboratory experiments in controlled conditions.

Numerous studies were focused on the characteristics of rock joints, which are essentially unpropped fractures. Bandis et al. (1983) investigated the deformation characteristics of rock joints under normal and shear loading, which closely resembles the deformation of unpropped fractures. Factors such as normal stress, joint surface roughness, initial actual contact area, initial flow aperture, and asperity size and strength were all investigated. Barton et al. (1985) coupled the joint deformation work of Bandis et al. (1983) with joint conductivity. They learned that, in general, smooth joints in weak rocks close easiest, while rough joints in strong rocks close the least. Olson et al (1993) studied the effect of shear displacement on conductivity in Austin Chalk samples. They learned that a small shear displacement, which is possible in hydraulic fracture

treatments, can have a permanent increase in conductivity due to the misalignment of asperities causing larger flow paths. Makurat (1996) identified that stress-dependent aperture, tortuosity, roughness, wall strength, normal stress, and shear displacement are all major factors on the permeability of single fractures in the absence of proppant.

The changing permeability and thickness of proppant packs under stress has major effects on propped fracture conductivity. Cooke (1973) studied the conductivity of fracture proppant in multiple layer packs. He studied the effects of closure stresses, sand size, and fluid type/temperature on the proppant pack. However, to isolate the effect of the proppant from rock effects, he used flat steel plates instead of rock samples. Penny (1987) studied the long term conductivities of a 2 lb/ft^2 areal concentration of 20/40 sand using both steel and flat sandstones. He determined that proppant embedment in the Ohio sandstone was a major factor in conductivity loss of proppant packs. Rivers (2012) studied the effects of high concentrations (4-8 lb/ft^2) of high strength proppant and high closure stresses on the conductivity of flat Berea sandstone samples. There are numerous other studies that investigate proppant pack conductivity.

In low permeability formations, low proppant concentrations with slickwater fracturing treatments are common in shale formations. Fredd et al. (2001) studied the fracture conductivity of low proppant concentrations (less than 1 lb/ft^2) on fractured Texas Cotton Valley sandstone cores. The rough fracture surfaces were kept intact for this study, which showed how the rock and proppant effects worked together to determine fracture conductivity. They introduced a concept of asperity- and proppant-dominated conductivity behavior. When proppant concentration is sufficiently low (or

fracture is unpropped), or closure stress is high enough, the rock properties such as asperity size, strength, and distribution, mechanical properties, and initial aperture dominate the fracture conductivity behavior. However, when proppant concentration increases, the proppant pack characteristics begin to control the conductivity. The conjunction of two conductivity behaviors is important when proppant concentration is low.

With the increase of shale hydraulic fracturing in recent years, studies looking at shale fracture conductivity have become prevalent. Rickman et al. (2008) demonstrated the effect of mechanical properties, mineralogy, and other petrophysical characteristics on deciding what sort of fracture treatment to perform. He suggests that high Young's Moduli and low Poisson's Ratios are beneficial in having a successful fracture treatment. The mineralogical composition determines the sensitivity of the shale formation to particular fracture fluids. It also has an important part in determining the mechanical properties. Li et al. (2013) agrees with Rickman et al. that a higher Young's Modulus and lower Poisson's ratio results in greater fracture treatment success. They also point out how coring depth can have a major effect on mechanical properties of the shale formation. This is something to take into account when using outcrop samples to conduct studies. Alramahi and Sundberg (2012) studied the effects of shale mechanical and mineralogical properties on flat shale samples. They found that a lower clay content (and as a result, a higher Young's Modulus) can significantly reduce proppant embedment. They were able to develop a power law expression for the proppant embedment effect as seen in Figure 3. They also measured the effect on Young's

Modulus on the fracture conductivity of smooth shale fractures. They determined that major conductivity differences start occurring at closure stresses greater than 3000 psi. At closure stresses less than 3000 psi, the differences are much less pronounced.

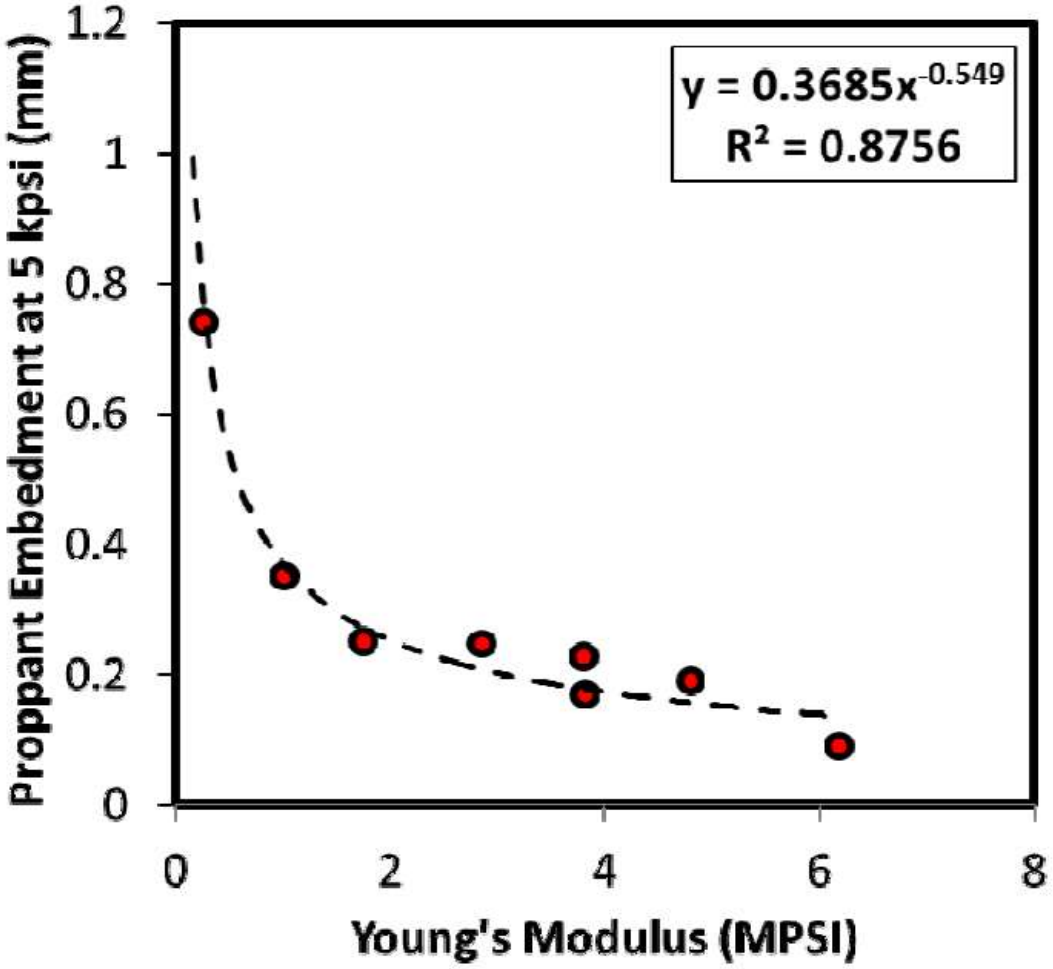

Figure 3 - Correlation for proppant embedment at 5 kpsi as a function of Young's Modulus (Alramahi and Sundberg, 2012)

Zhang et al. (2013) measured the fracture conductivity of rough fractures in Barnett Shale outcrop samples. They studied both natural and induced fractures that were either aligned or had shear displacement. They also studied the effects of proppant size and concentration (including unpropped) on the conductivity. Guzek (2014) and Briggs (2014) performed similar experiments on the Eagle Ford and Fayetteville shale outcrop samples, respectively. All three studies found that as proppant concentrations increase, the importance of the rock properties decrease.

The objective of this study is to relate the conductivity measurements of Guzek (2014) and Briggs (2014) to the rock characteristics of their corresponding outcrop samples to better understand the relationship between rock and proppant characteristics. Ideally, this relationship would continue beyond the Eagle Ford and Fayetteville shale to other shale formations such as the Barnett and Marcellus shale.

1.5 Problem Description

Hydraulic Fracturing is an integral and expensive part of the development of any shale well. In order to properly optimize a fracture treatment design, the characteristics of the rock must be taken into account. The effect of rock properties on effectively transporting proppant is relatively well known. Operators target brittle portions of hydrocarbon bearing shale in order to maximize propped fracture size and fracture network complexity. These brittle regions are characterized by a higher Young's Modulus and lower Poisson's Ratio. These more brittle shales usually also have lower clay content. These properties can be estimated with well logging along the horizontal

lateral. In ultra-low permeability formations, most of this optimization involves placing low concentrations of proppant as far away as possible from the wellbore in order to maximize the reservoir contact.

Another important factor in fracture design optimization is maximizing the effectiveness of the proppant that is placed. This study looks at the relationship between fracture conductivity of both propped and unpropped fractures and rock mechanical properties and mineralogy. Understanding this relationship can help to create desired fracture conductivity in shale reservoirs. Samples from the Eagle Ford Shale and Fayetteville Shale zones FL2 and FL3 are examined in this study to address these problems.

1.6 Research Objectives

The purpose of this research is to investigate the relationship between the fracture conductivity of collected outcrop samples and their respective rock properties. The main rock properties of interest are Young's Modulus and Poisson's Ratio, as well as sample mineral composition. These three parameters can be estimated with well logging technologies. If there a significant relationship between fracture conductivity and these rock properties, then the knowledge can be used to help optimize hydraulic fracturing design in the field.

There are two problem scales in this study. The "micro" scale is within a specific geologic zone of a shale reservoir. Horizontal shale wells that are fractured numerous times along the lateral can have significant variations in the same zone (Gardiner et al.,

2013). The “macro” scale is a comparison across geologic zones. The major objectives of this research are as follows:

1. Develop a singular experimental process to measure the elastic moduli of rock outcrop samples with a range of drastically different behaviors and characteristics. A standardized process must be used in order to compare not only within a geological zone, but also over several unique zones of different shale formations. The starting points for this process are ASTM D4543 – 08 (2008) and ASTM D7012 – 14 (2014) standards, but these will have to be modified.
2. Measure the Young’s Modulus and Poisson’s Ratio of shale samples from the Eagle Ford and Fayetteville shale (Zone FL2 and Zone FL3) via triaxial compression testing. Also measure the mineralogical composition of the samples with a combination of X-ray Diffraction (XRD) and Fourier Transform Infrared Spectroscopy (FTIR). In the case of the Eagle Ford samples, each specimen is directly associated with a conductivity measurement. In the two Fayetteville zones, the specimens are associated with the zone as a whole.
3. Determine if the small variations in rock properties have a significant effect on fracture conductivity within the Eagle Ford shale. Determine if the large variations in zone-averaged rock properties have a significant effect on fracture conductivity across the Eagle Ford, Fayetteville FL2, and Fayetteville FL3 zones. Both unpropped and propped fracture conductivities are of interest.
4. Determine the causes of fracture conductivity behavior outside mechanical and mineral composition. An example of another cause is surface roughness differences.

2. LABORATORY APPARATUS AND EXPERIMENTAL PROCEDURE

2.1 Description of Laboratory Apparatus

In order to characterize the mechanical properties of the shale formations, a triaxial rock testing system was used. The GCTS RTX-1500 Triaxial Rock Testing System is specifically designed to test rock parameters such as Young's Modulus and Poisson's Ratio while controlling confining and pore pressures. The system is capable of measuring the properties of rock samples with diameters up to 2 inches and sample lengths up to 4 inches. An axial load of up to 1500 kN can be applied to the rock. The system is capable of confining pressures of up to 20,000 psi. It is also capable of maintaining an internal rock pore pressure of up to 20,000 psi. For the purposes of this research, the full loading capabilities (axial, confining, and pore) were unnecessary. The pore pressure capabilities were not used at all. The major benefit of the GCTS RTX-1500 system is the deformation instrumentation and data acquisition. Internal instrumentation, using Linear Variable Differential Transformers (LVDTs), is able to measure axial and circumferential deformations as small as 0.001 millimeters. The RTX-1500 meets the specifications of the International Society of Rock Mechanics (ISRM) for rock sample triaxial tests.

The Triaxial test system consists of the following components:

- GCTS hydraulic load frame with 1500 kN capability
- GCTS High Pressure Triaxial cell with internal instrumentation
- Sealed piston/platen system for applying axial load to rock samples

- Two 140 MPa servo-controled pressure intensifier system cabinets for cell and pore pressure application and control
- Internal instrumentation consisting of three LVDTs
- Data acquisition system (SCON – 2000 Digital System Controller) that interfaces with a Microsoft Windows PC

As seen in Figure 4, a rock sample being tested is placed between the two metal platens. The bottom platen is threaded on the bottom so that it can be easily secured to the base of the high-pressure triaxial cell. The top platen is rounded at the top to account for imperfect rock samples or sample shifting. On both platens in the middle, there is a 1-inch diameter stand for the rock to be placed on. These stands have an O-ring groove for sealing purposes and a mounting groove for the internal instrumentation. Both platens also have small ports that can be connected to the pore pressure cabinet. For this research, those ports were sealed to prevent confining oil from infiltrating the rock cores. Rocks were sealed with a thin polyolefin heat-shrink wrap to prevent the confining oil from getting into the rock samples and causing an undesired pore pressure effect.

Figure 4 - Eagle Ford core in position between the two platens

The internal instrumentation is mounted onto the rock sample and platens. This can be seen in Figure 5. Two LVDTs are used to measure the axial deformation of the sample, while a third LVDT is used in a circumferential chain gauge around the rock to measure the circumferential deformation. The LVDTs are able to detect changes in the magnetic field caused by very small movements of ferromagnetic cores. They can detect movements as small as 0.001 mm. As an axial load is applied, the rock compresses in the axial direction and expands in the radial direction. The axial LVDTs are held by brackets that secured to the platen mounting grooves with spring-loaded set screws that prevent over tightening. The two LVDTs are mounted on opposite sides of the rock so that an average axial deformation can be measured. A chain gauge is used in the experiments

(Figure 6). The chain gauge consists of a series of rollers that are connected in series to two parts of a LVDT mounting block system. The chain is wrapped around the rock sample, where the two halves of the mounting block system can be held together with springs or rubber bands. The chain gauge must be tight enough to have sufficient contact with the rock sample without sagging, yet have the freedom to expand as the rock expands. These LVDTs signal outputs are passed from the sample to internal connections on the base of the triaxial cell. These signals are then passed through the cell wall to external connections to reach the data acquisition system.

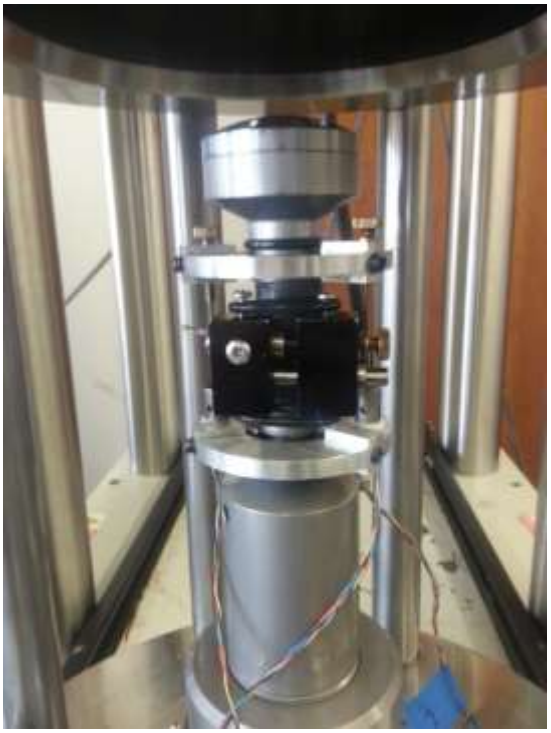

Figure 5 - Rock sample with deformation instrumentation mounted in triaxial cell

Figure 6 - Chain gauge for measuring circumferential deformation of rock samples

The Triaxial cell is integral to the ability to perform any tests involving high pressures and axial loads. Figure 7 shows the open triaxial cell with the rock sample in place. The entire cell is made of strong steel that can contain 20,000 psi of pressure. The triaxial cell consists of two main pieces. The base piece consists of a small, elevated cylindrical platform where the sample is mounted and instrumentation cabling is passed through. Around the small platform is a custom high-pressure seal that prevents leakage from where the top piece contacts the base. Figure 8 shows the bottom of the triaxial cell. The upper piece consists of a hollow cylinder with a flat top piece with a larger diameter. This piece is moveable so that the sample and instrumentation can be easily accessed. The sample sits in the hollow space of the upper piece when the upper piece is in the down position. The two components of the cell must be securely tightened to each other by the eight steel rods with nuts and washers which are around the triaxial cell. If

the cell is not securely tightened, there can be very dangerous leaks (oil with high pressure) that occur around the base seal as the cell is pressurized. Finally, the top piece has a circular opening that allows the load piston to pass through the cell top and contact the top platen of the sample apparatus. The load piston is flat on top to best contact the load frame piston, but has a concave bottom to fit with the rounded top platen. The opening has a seal around it to contain the pressurized oil from leaking through the piston/cell interface.

Figure 7 - Open triaxial cell with sample in place

Figure 8 - Triaxial cell base

In order to apply a confining stress, a cell pressure cabinet is used. Figure 9 shows the cell pressure cabinet. The cabinet has a hydraulic oil reservoir that holds enough oil to fill the hollow triaxial cell. The cabinet uses compressed air at approximately 80 psi to push the oil between the cabinet and the triaxial cell to fill and drain the cell for experiments. When the cell is full of hydraulic oil, it can be isolated from the reservoir and pressurized by the 140 MPa servo-controlled cell pressure intensifier. This intensifier is capable of maintaining cell pressures up to 20,000 psi. The cell pressure is measured using a pressure transducer that is accurate to +/- 0.1 MPa.

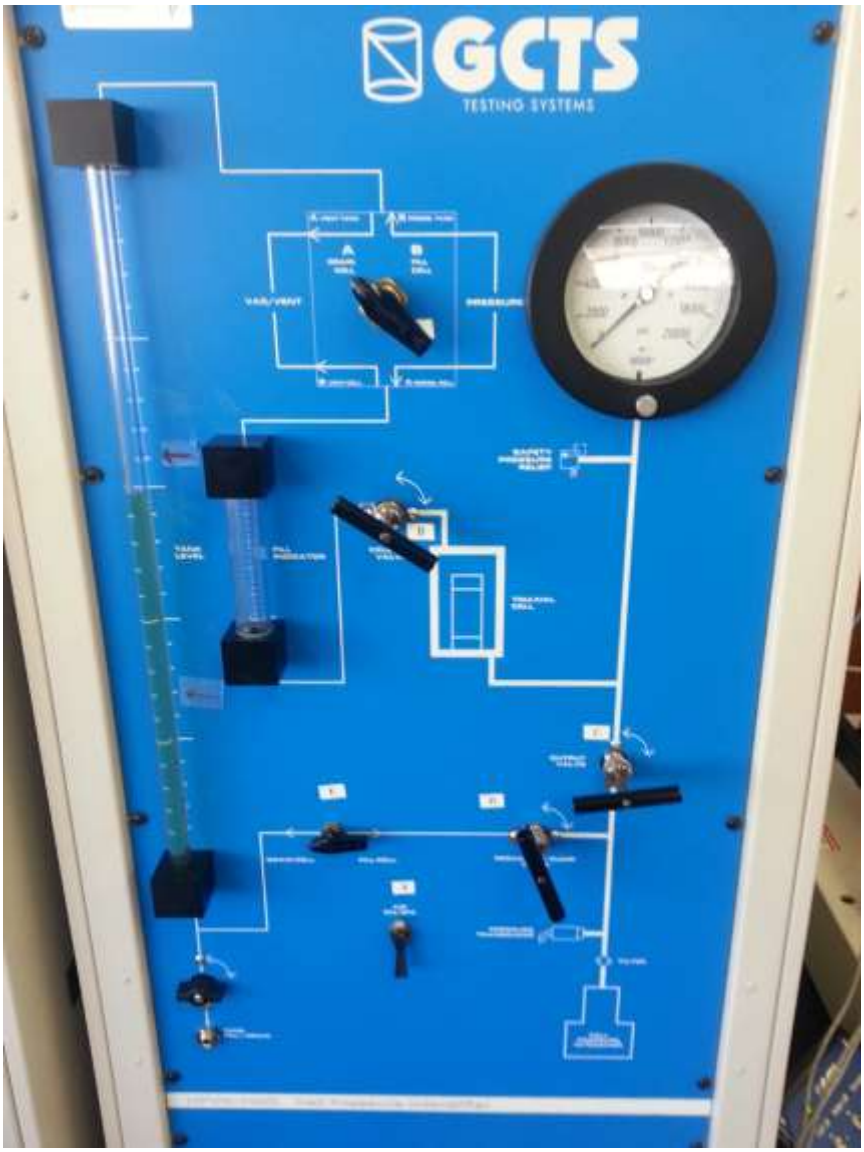

Figure 9 - Cell pressure cabinet with valves for oil control

While safety should always a top priority in experimental work, it is even more important while operating the GTX RTX-1500 system. Even at the low pressures that this work was dealing with, a lapse of concentration could result in equipment damage, massive oil leaks or sprays, or even injuring operators. Pressure containment must be

constantly monitored. An unnoticed rock sample failure could result in the complete destruction of the instrumentation due to continued load application or even worse, damage to the triaxial cell itself. Figure 10 shows an example of post-failure behavior (Patterson and Wong, 2005). In some failures, the rock is physically unable to withstand further application of stress and rapidly deforms. Any test must be stopped quickly in this situation. Great care must be taken while using the equipment.

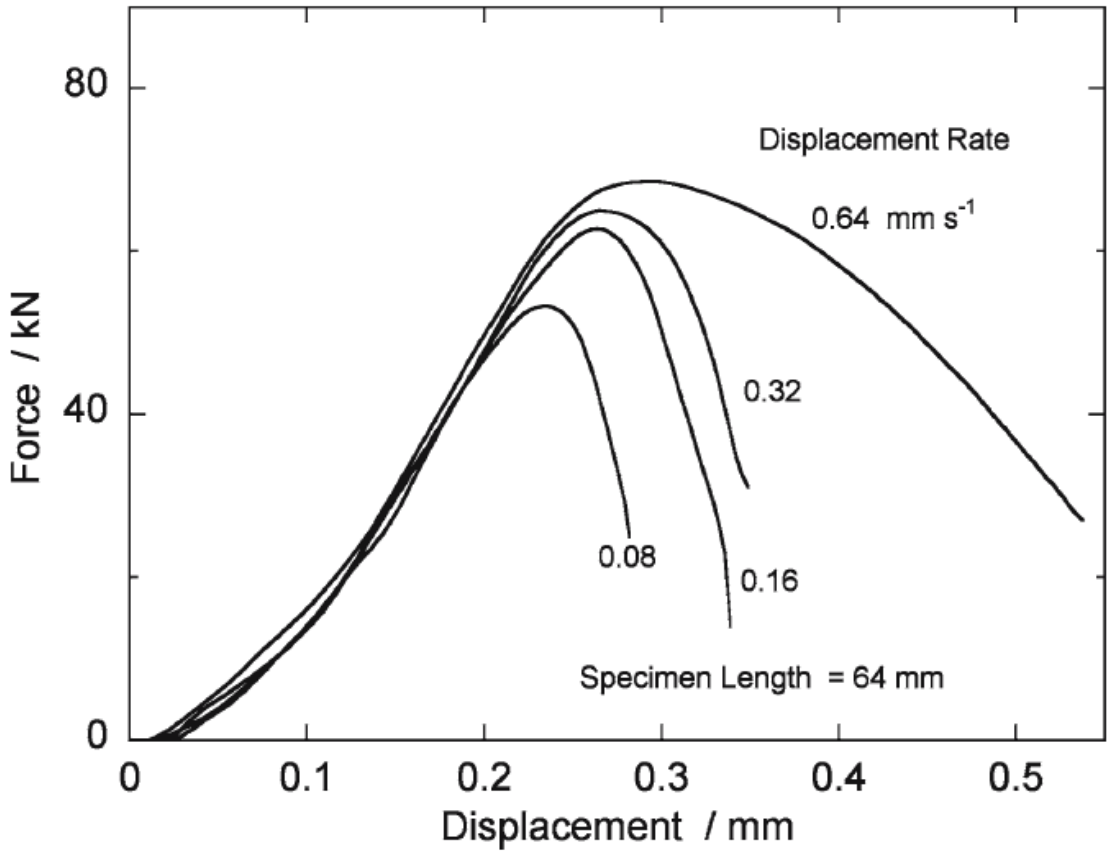

Figure 10 - Post-failure behavior of rock core (Patterson and Wong, 2005)

2.2 Experimental Procedure

The top priority in the experimental procedure design for this research was developing a consistent procedure that could be used across all samples in different shale zones of interest. Consistency across measurements for valid comparisons was the primary goal.

2.2.1 Sample Preparation

Cylindrical core samples for triaxial testing were cut from the bulk shale outcrop samples as close to the desired dimensions and tolerances as physically possible. The core sample size depends on the available rock source and will be described later. All core samples were cut so that the axial load would compress the bedding plane layers. Shale mechanical properties are anisotropic, so care must be taken to ensure that the mechanical properties measured are most applicable to the conductivity tests. In the conductivity measurements, the fractures are induced along the bedding planes with the closure stress applied to compress the fracture and bedding planes. The method of selecting what specific outcrop sample to cut the core samples from depends on the zone. For the Eagle Ford cores, samples were cut from the same horizontal outcrop locations as the fracture conductivity samples that were tested. This would allow for comparisons between the localized conductivity and mechanical properties. In the Fayetteville zones, the outcrop samples were so fragile, that the cores had to be cut from the best rocks available. As such, the Fayetteville zones were treated as large sample

points. This prevented associating a specific rock core with a specific conductivity measurement.

ASTM International (formally known as the American Society for Testing and Materials) has standard practices for preparing rock cores for mechanical testing. ASTM D4543 – 08 (Standard Practices for Preparing Rock Core as Cylindrical Test Specimens and Verifying Conformance to Dimensional and Shape Tolerances) defines the tolerances for the cut rock cores as follows (2008):

- A Length-to-Diameter ratio (L/D) of 2.0 to 2.5
- Minimum Diameter is 1-7/8 inches
- The Cylindrical surfaces of the specimen shall be generally smooth and free of abrupt irregularities with all the elements straight to within 0.020 inches over the full length of the specimen
- The ends of the specimen shall be cut parallel to each other and at right angles to the longitudinal axis. The end surfaces shall be surface ground or lapped flat to a tolerance not to exceed 0.001 inch.
- The ends of the specimen shall not depart from perpendicularity to the axis of the specimen by more than 0.25 degrees.
- The parallelism tolerance is the maximum angular difference between the opposing best-fit straight line on each specimen end by 0.13 degrees.

These standards are very strict to ensure that specimen shape is not affecting the measurements made in the triaxial tests. However, due to the nature of the bulk outcrop

samples, these standards are practically impossible to meet for all cores. The ASRM standards call for 2 inch diameter cores (which then require 4 inch tall cores) and require surface grinding to ensure proper shape. Due to the size limitations of the Fayetteville shale outcrop samples, smaller 1 inch diameter cores, with a 2 inch height had to be used for all three zones of interest. The Eagle Ford core samples were very consolidated and easy to cut to the desired tolerances. The Fayetteville FL2 samples were more difficult to cut to the standards, but were generally close to the tolerances. The Fayetteville FL3 samples were impossible to cut within the tolerances. Due to the highly laminated nature of the FL3 samples, any attempt to flatten the end surfaces resulted in the destruction of the core. This resulted in having to account for the core deficiencies in the results analysis.

Once the core specimen was obtained, it was ready to be prepared for use in the triaxial cell. The detailed procedure is as follows:

1. Measure the height and diameter of the rock sample. Take three readings of diameter along the height of the sample to ensure an accurate quantification of the diameter.
2. Place rock sample on bottom test platen.
3. Measure and cut a piece of polyolefin heat-shrink tubing that will overlap the O-rings on both the top and bottom platens.
4. Manually work-out the creases in the initially-flat heat-shrink to make it as circular as possible before heat application. This will help prevent uneven shrinking of the heat-shrink.

5. While stabilizing rock sample from the top, begin slowly shrinking the heat-shrink from bottom-up with the use of a heat gun. Even shrinking is necessary for accurate results. Avoid melting the heat-shrink. Continue until heat shrink has constricted the rock sample to the bottom platen.
6. Place the bottom LVDT holder ring around the sample, letting rest on bottom platen.
7. Place the top LVDT holder ring around the sample, ensuring that the instrumentation holes align properly with the bottom ring (i.e. ring is not upside down).
8. Place the top test platen onto the rock sample and finish heat shrinking until the heat-shrink is completely constricting the rock sample and overlaps the top O-ring.
9. Allow the apparatus to cool and the heat-shrink to "set" for several minutes.
10. Once cool, screw the bottom platen into the triaxial cell base. Ensure that the platen is fully screwed in.
11. Place the LVDT top brass components in the top LVDT holder ring.
12. Mount the top holder ring to the top platen mounting groove by finger tightening the three set screws. Be careful not to puncture the heat-shrink.
13. Place the circumferential chain gauge on the center of the rock sample and use two springs to apply tension. Ensure that the chain is snug and perpendicular to the sample's longitudinal axis.

14. Place the LVDT detectors into the bottom holder ring. Mount the bottom holder ring to the bottom platen mounting grove in the same way as the top ring. Make sure that the LVDT components will align.
15. Thread the LVDT ferromagnetic cores into the brass components.
16. Make final adjustments to the instrumentation mounting:
    a. Ensure the LVDT holder rings are centered around the core
    b. Ensure the LVDT holder rings are secure to the platens to prevent shifting during testing
    c. Ensure the LVDT ferromagnetic core is able to move through the detector with no friction.
17. Connect the LVDT wiring to the correct instrumentation ports
18. Using the brass components, adjust the initial position of the LVDT cores in the detectors so that there will be sufficient measurable range. (Set Axial Deformations to -1.5 mm, Circumferential deformation to +0.5 mm.)

At this point, the sample instrumentation setup is complete, and the testing procedures can begin.

2.2.2 Rock Mechanical Property Measurement

The goal of the mechanical property measurements is to obtain the Young's Modulus and Poisson's Ratio of the three different zones. ASTM D7012 – 14 (Standard Test Methods for Compressive Strength and Elastic Moduli of Intact Rock Core

Specimens under Varying States of Stress and Temperatures) deals with the standard methodology for this experiment (2014).

The experimental procedure that was actually used in this research differs from the standards. The procedure was developed while testing 2-inch diameter Eagle Ford cores, but consistency had to be kept when testing the cores of varying sizes from different zones. If the experimental procedure was changed between zones, the data would not be comparable across the zones.

Normally, the Young's modulus and Poisson's ratio of a rock sample is measured with a uniaxial compression test. However, in order to hold the rocks together under failure, all tests were run with a 2 MPa confining stress. This would help prevent damage to instrumentation in a potential rock burst event and hold together the fragile cores (especially Fayetteville samples), but would not be too large to avoid major effects on the results. By using a confining stress, the Young's Modulus and Poisson's ratio are not actually being measured. Rather, the Elastic moduli at a 2 MPa confining stress is being measured. The addition of a confining stress will increase the "Young's Modulus" and decrease the "Poisson's Ratio". For simplicity, these moduli will be referred to by their normal terminology. The most important point is that the same confining stress is applied over all of the tests to allow for a like-to-like comparison.

The measured elastic moduli of the rock samples can be affected by the rate at which stress is applied. As such, the rate must be consistent across all samples. Because of the brittleness of shale, a slow ramp rate of 2 MPa/minute was selected to prevent sudden rock failure. Since the load is applied under stress control, not strain control, a

sudden rock failure could result in an uncontrolled strain and equipment damage. The maximum differential stress (stress difference between the axial stress and confining stress) applied to the rock sample during the test was on the order of the maximum closure stress applied to the fractured samples during the conductivity experiments. For the Eagle Ford samples this maximum stress was 45 MPa (6527 psi) and for the Fayetteville samples this maximum stress was 30 MPa (4351 psi). The maximum closure stress for conductivity tests was 6000 psi for the Eagle Ford samples and 4000 psi for the Fayetteville samples (although most samples were only tested up to 3000 psi).

After the sample was loaded to the correct maximum stress, the sample was then slowly unloaded at the same rate back down to a 1 MPa contact stress. Due to the uncorrectable imperfections in several of the shale cores, each core was loaded and unloaded several times in order to remove non-elastisities from the rock. This process helps to account for the imperfections by essentially removing them. Once the load curves reach equilibrium (stress-strain curve follows the previous curve), then the test can be considered to be complete, and the elastic moduli can be determined from the most recent curve.

The detailed procedure for measuring the elastic moduli of the rock samples after sample preparation is as follows:

1. Turn on the hydraulic pump that provides pressurized oil to drive the servos.
2. Carefully lower the upper piece of the triaxial cell using the cell lift. Ensure that no wires or other objects get caught in the seal around the lower platform.

3. Disconnect the cell lift from the upper triaxial cell and raise the cell lift to a safe position.
4. Use the cell rod nuts on 8 cell rods and tighten in a star pattern.
5. Double check that all nuts are fully tightened. If even one is loose, then there will be a dangerous, high pressure oil leak.
6. Carefully insert the piston into the circular hole on top of the triaxial cell. Ensure that the piston has made contact the rounded surface of the top platen.
7. Use the cell roller lift to move the triaxial cell into position under the axial load frame. Figure 11 shows the triaxial cell in position.

Figure 11 - Sealed triaxial cell ready to receive axial load

8. Using the servo controller, move the axial load piston down, until it is almost in contact with the cell piston.
9. Apply a 1 MPa contact deviator stress with the axial load piston. At this point in the procedure, the rock sample has a force applied to it. Use caution.
10. Using the cell pressure intensifier cabinet, fill the triaxial cell with hydraulic oil from the reservoir using the pressurized air.
11. Isolate the triaxial cell from the oil reservoir by shutting the appropriate valves.
12. Using the cell pressure intensifier servo controller, apply a constant confining stress of 2 MPa. Allow all systems to reach equilibrium before continuing.
13. Input specimen dimensions into the GCTS software for proper strain calculations.
14. Set all LVDT deformation sensors to zero.
15. Run the triaxial test program (data collection starts here):
    a. Ramp up the differential stress at a rate of 2 MPa per minute until the desired maximum differential stress is reached.
    b. Decrease the differential stress at a rate of 2 MPa per minute until the differential stress is back to 1 MPa.
    c. Hold a constant differential stress of 1 MPa for at least one minute to allow the system to reach equilibrium again.
    d. Repeat steps 15a – 15c until the stress-strain curves are repeating.

16. End the triaxial test program.
17. Set the differential stress to 3 MPa in preparation to drain the cell. This provides an extra cushion to prevent the piston from getting pushed out by the cell pressure while draining.
18. Lower the cell pressure to 0.5 MPa.
19. Open the valves in the cell pressure cabinet to enable the cell to drain.
20. Drain the cell using the air pressure.
21. After draining the cell, turn off the applied air pressure, and allow the internal cell air pressure to reach atmospheric pressure.
22. Lower the differential stress to 1 MPa.
23. Carefully raise the axial load piston, making sure that there is no residual air pressure that is pushing the cell piston out.
24. Use the cell roller lift to move the triaxial cell out from under the axial load frame.
25. Carefully remove the cell piston from the cell. At this point, the cell is in a safe, unpressurized condition.
26. Unscrew the 8 cell rod nuts and use the cell lift to raise the upper triaxial cell.
27. Examine the sample and instrumentation to ensure that no oil infiltrated the sample and that no instrumentation shifted during the test.
28. Remove the instrumentation from the sample, and the sample from the cell.
29. The experimental data can now be exported from the data acquisition system and the elastic moduli of the sample can be determined.

2.2.3 Elastic Deformation

The general mathematics behind elastic deformation is relatively simple. Whenever a force is applied to an object, there is some deformation. If the deformation is elastic, when the force is no longer applied, the object will return to its initial dimensions. If the deformation is non-elastic, the object will have been permanently deformed. In order to best quantify the deformation of an object, the concept of strain is used. Strain is defined as:

$$\epsilon = \frac{\Delta l}{l_0} \quad \text{(2-1)}$$

where l_0 is the initial length of an object in the direction of the force and Δl is the change in length of the object from the force. The amount of deformation is dependent on the force applied *F*, the cross-sectional area *A*, and the material properties. The applied stress on an object is defined as:

$$\sigma = \frac{F}{A} \quad \text{(2-2)}$$

In the elastic region of deformation, stress and strain are linearly related:

$$\sigma = E\epsilon \quad \text{(2-3)}$$

where *E* is the elastic modulus known as Young's Modulus. When a compressive stress is applied to an object, there are also resultant strains in the transverse direction. The Poisson's ratio of a material is defined as follows:

$$\nu = -\frac{\epsilon_{transverse}}{\epsilon_{axial}} \quad \text{(2-4)}$$

or, in the case of a cylindrical sample:

$$\nu = -\frac{\epsilon_r}{\epsilon_a} \quad \text{(2-5)}$$

where ϵ_r is the radial strain and ϵ_a is the axial strain. In this research, the radial strain is calculated by measuring the circumferential deformation with the chain gauge. The relationship between the circumferential deformation and radial deformation is as follows:

$$\epsilon_C = \frac{\Delta C}{C_0} = \frac{2\pi\Delta r}{2\pi r_0} = \frac{\Delta r}{r_0} = \epsilon_r \quad \text{.....(2-6)}$$

where C_0 is the initial circumference of the rock, ΔC is the change in the circumference of the rock due to the axial load, r_0 is the initial radius of the rock, and Δr is the change in the radius of the rock.

The major experimental portion of this work involves measuring the elastic moduli, E and ν, of the rock samples by triaxial compression. Figure 12 shows the stress condition of a cylindrical rock sample undergoing a triaxial test (Patterson and Wong, 2005).

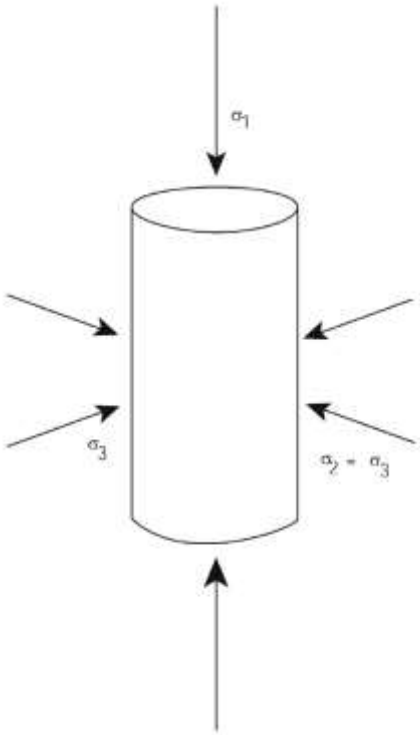

Figure 12 - System of stresses in a conventional triaxial test (Patterson and Wong, 2005)

In this three-dimensional situation, there are three principal stresses applied to rock samples. The greatest principal stress is σ_1, the intermediate principal stress is σ_2, and the smallest principal stress is σ_3. In a triaxial test where pressurized fluid is used as the confining stress, σ_2 is equal to σ_3. The confining stress is applied both radially and on the top and bottom of the rock specimen. The confining stress is also acting on the load piston, trying to push it upward. This means that the hydraulic load frame must apply a stress of at least σ_3, to prevent a cell breech. The measure of how much greater the applied stress compared to σ_3, is called the Differential Stress:

$$\sigma_D = \sigma_1 - \sigma_3 \quad \text{(2-7)}$$

The differential stress is sometime called the deviator stress. This terminology is used in the GCTS software package. Modifying Equation (2-3) to include the deviator stress, and solving for the modulus of elasticity, the following equation is obtained:

$$E = \frac{\Delta(\sigma_1 - \sigma_3)}{\epsilon_a} = \frac{\sigma_D}{\epsilon_a} \quad \text{(2-8)}$$

If σ_D were to be plotted on the y-axis and ϵ_a on the x-axis, the slope of the linear portion of the stress-strain curve would be the Elastic modulus. For this research, a linear least-squares curve fit will be applied to the linear portion of the data in order to determine the elastic properties. In a similar way, the Poisson's ratio can be determined by plotting ϵ_a on the x-axis and ϵ_r on the y-axis and performing a linear curve fit. Figure 13 shows a series of stress-strain curves for Wombeyan marble as confining pressure is increased (Patterson and Wong, 2005). All of these stress-curves start out in the linear, elastic deformation regime, and then reach a yield point. In this research, the yield point is to be avoided to prevent damage to the limited number of samples. It is also important to note that the addition of a small confining stress does not have a discernable effect on the Young's modulus of the Wombeyan marble. The confining stress would have an effect on the Poisson's Ratio of the rock because the confining stress is directly inhibiting the expansion of the rock transverse to the axial load.

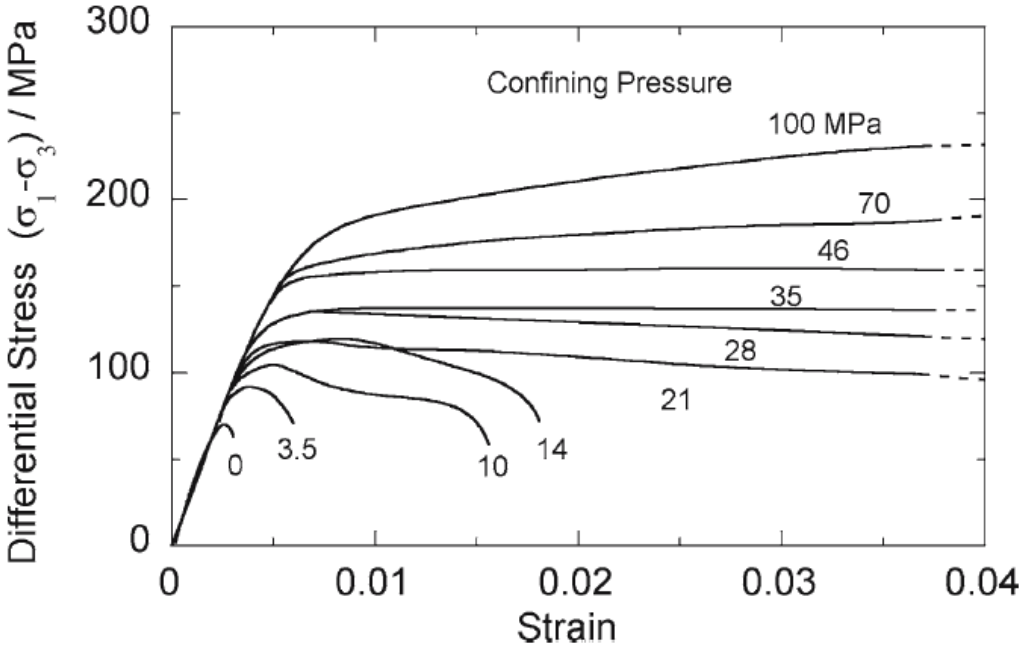

Figure 13 - Stress-strain curves of Wombeyan Marble (Patterson and Wong, 2005)

2.2.4 Permanent Deformation

When the stress in a material is high enough, the deformation can become permanent. Deformation past the yield point involves permanent deformation instead of just elastic deformation. It is important to note that the deformation occurring in the fracture conductivity tests does involve permanent deformation. At a specific point on the fracture surface (for example, an asperity), the localized stress can be significantly higher than the fracture closure stress. This is due to the physical contact area between the two fracture faces being a fraction of the overall fracture surface area. In these points, the stress may exceed the yield stress, and permanent deformation will occur. Proppant embedment is another example of permanent deformation. After the closure

stress is removed, permanent embedment marks are left behind, indicating that permanent deformation occurred. Interestingly, the Young's Modulus of a rock is related to the compressive strength (D'Andrea et al., 1965). A larger Young's Modulus generally results in a higher yield stress. The actual yield stresses of the rocks were not measured due to limited rock availability. By investigating the effect of Young's Modulus on fracture conductivity, it must be understood that any relationship might also be caused by changing the threshold for permanent deformation.

2.2.5 Rock Mineralogical Composition Measurement

An outside contractor, Ellington and Associates, Inc., was used to perform Fourier transform infrared spectroscopy (FTIR) analysis on the shale samples in order to obtain the relative percentages of major mineral compositions. The major mineral compositions of the shale samples are Quartz, Carbonates, Clays, and Feldspars. The FTIR results were verified by performing X-ray Diffraction (XRD) analysis on every 5-10 samples (depending on the zone).

The samples that were provided to Ellington were at least 5 grams of shale from conductivity samples used in testing. The surfaces of the outcrop samples have significant weathering that could have drastically changed the measured composition of the samples from those actually being tested. Care was taken to ensure that no foreign substance such as proppant or epoxy coating contaminated the FTIR/XRD samples.

2.3 Laboratory Shale Fracture Conductivity Measurements

The laboratory shale fracture conductivity measurements used in this study were obtained from shale outcrop samples with rough fracture surfaces. The complete test characteristics for measuring fracture conductivity can be found in Kamenov (2013), Guzek (2014), and Briggs (2014).

Eagle Ford conductivity samples were taken from seven different lateral locations over a 1,015 foot long outcrop in South Texas. The following conditions were used in the Eagle Ford conductivity tests (Guzek, 2014):

- Unpropped Samples: Closure Stress (1000 psi – 4000 psi)
- Propped Samples: Closure Stress (1000 psi – 6000 psi)
    - 0.1 lb/ft^2 concentration of 30/50 mesh white sand
    - 0.2 lb/ft^2 concentration of 30/50 mesh white sand

Fayetteville shale conductivity samples were dug up from an outcrop in order to get to unexposed rock. The rocks came from two vertical geologic zones, FL2 and FL3 which consist of the two sample points for comparison (as opposed to the Eagle Ford which has 7 points). Multiple conductivity samples were taken from each zone. The following conditions were used for samples from both FL2 and FL3 (Briggs, 2014):

- Unpropped Samples - Closure Stress range of 500 psi – 3000 psi
- Propped Samples - Closure Stress range of 500 psi – 3000 psi
    - 0.03 lb/ft^2 concentration of 30/70 mesh Arkansas river sand
    - 0.01 lb/ft^2 concentration of 30/70 mesh Arkansas river sand

2.4 Experimental Design Matrix and Conditions

The scale of the rock properties tests was determined by the scale of the fracture conductivity measurements for each zone. In the Eagle Ford shale, the lateral changes within a single geologic zone were the main focus. Each of the seven outcrop sampling points had a complete set of conductivity measurements in an attempt to quantify the lateral differences. As such, the rock properties at each of these seven points were measured. Two triaxial tests were attempted at each of the seven locations to better quantify the mechanical properties. The mineral composition of each sample point was also measured to quantify the lateral differences. In order to perform cross-shale investigations, the measurements of all locations in the Eagle Ford were consolidated into whole zone properties.

In the two Fayetteville shale zones FL2 and FL3, the main focus on conductivity measurements was the cross-zone comparison. The outcrop samples were obtained from a single sample point (two different depths). This did not allow for the study of the lateral changes in the zone. As such, the rock properties of each zone as a whole were measured with several sample points in each zone for mechanical properties and mineralogical composition. This allowed for comparisons with other shale zones, but not within a specific Fayetteville zone.

Table 1 shows the experimental design matrix for this study. The proppant concentrations and mesh sizes come from the performed fracture conductivity measurements. These subsets are what will be compared between sample points or zones.

Table 1 - Experimental Design Matrix for Rock Characterization and Conductivity Measurements

	Sample Point	Goal Triaxial Tests	Mineralogical Test	Proppant Concentration [lb/ft^2]	Proppant Mesh Size
Eagle Ford	EF1	2	FTIR	unpropped 0.1 0.2	30/50
	EF2	2	FTIR		
	EF3	2	FTIR		
	EF4	2	XRD		
	EF5	2	FTIR		
	EF6	2	FTIR		
	EF7	2	FTIR		
Fayetteville	FL2	3	XRD - 1	unpropped 0.03 0.1	30/70
			FTIR - 4		
	FL3	3	XRD - 1		
			FTIR - 4		

3. EXPERIMENTAL RESULTS AND DISCUSSION

A series of triaxial compression tests and mineralogical quantification tests were performed in order to measure the rock properties of shale outcrop samples. These samples were collected from Eagle Ford and Fayetteville shale outcrops. In the Eagle Ford, seven sample points within Facies B were taken over 1,015 feet of highway cut. For the Fayetteville, samples were taken from the FL2 and FL3 zones to study the vertical heterogeneity. The relationship between the rock characteristics and measured fracture conductivity was then studied.

The raw experimental results from the Eagle Ford, Fayetteville FL2 and Fayetteville FL3 will be presented in sections 3.1, 3.2, and 3.3, respectively. For each zone, mechanical and mineralogical results will be presented, followed by a fracture surface roughness analysis. Then, the conductivity results will be summarized. An overall analysis of the relationship between rock characteristics and fracture conductivity on both "macro" scale (between average properties of geologic zones) and "micro" scale (between different Eagle Ford sample locations) is presented in section 3.4.

3.1 Eagle Ford Shale Results

Table 2 summarizes the Eagle Ford sample location names and their relative locations in feet from the starting point of the first sample, EF1. The sample names will be used as the identifier for all rock samples associated with the specific location.

Table 2 - Eagle Ford Sample Locations

	EF1	EF2	EF3	EF4	EF5	EF6	EF7
X-Location [ft]	0	190	335	455	635	835	1015

3.1.1 Eagle Ford Mechanical Properties

Triaxial compression tests were performed on multiple cores from Eagle Ford outcrop samples. Two triaxial tests were attempted from each of the seven sample locations. The Eagle Ford cores were very durable, so they were able to be cut to standards for cylindrical test specimens without breaking. The samples were tested up to a 45 MPa deviator stress. An example of a complete Eagle Ford triaxial compression test stress-strain curves for determining Young's Modulus can be seen in Figure 14. The associated axial-radial strain curves for determining Poisson's Ratio can be seen in Figure 15. This shows the three consecutive loads cycles on the sample. The complete triaxial results for all the Eagle Ford samples can be found in Appendix A.

Each of the Eagle Ford triaxial measurements took three full load cycles to determine the mechanical properties. The first load removed the majority of the inelastic behavior so that future loads would be elastic deformation. The second load was essentially elastic deformation. The third load was for confirmation of approximate equilibrium. Several of the stress-strain curves have initial behavior that does not fit the linear trend at higher stresses. This is likely due to very slight sample and instrumentation shifting under initial load. As such, the curve fits do not include the low

stress data on the last load. Most of the Eagle Ford stress-strain curves are generally linear overall.

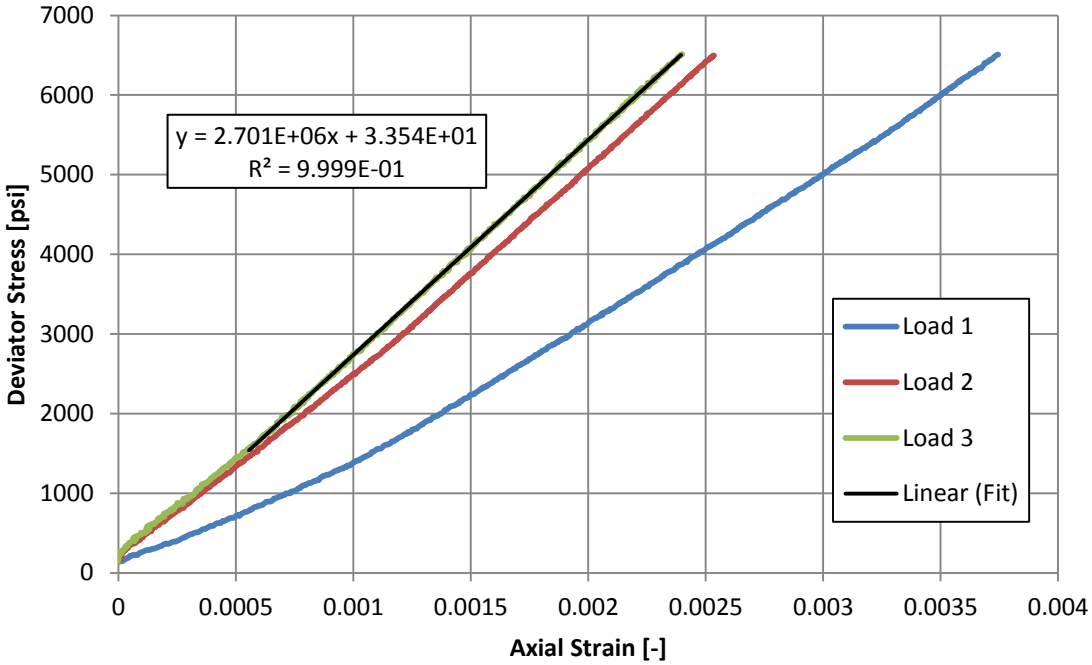

Figure 14 - Stress-strain curves for Eagle Ford sample EF1(2)

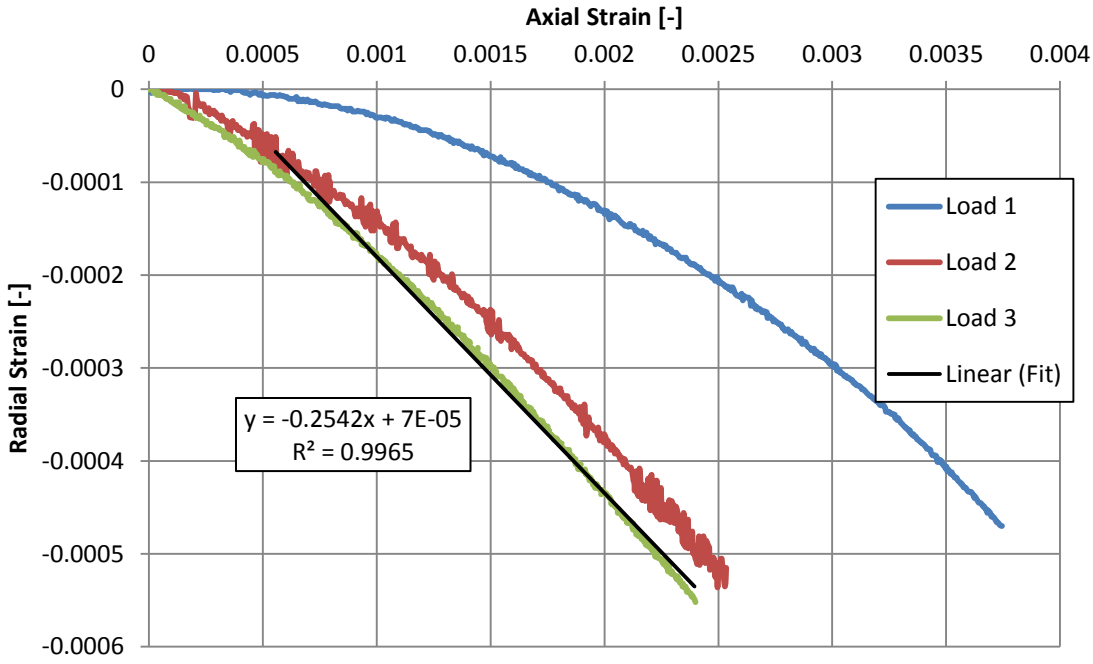

Figure 15 - Axial-radial strain curves for Eagle Ford sample EF1(2)

The axial-radial strain curves for determining the Poisson's ratio have more curvature than the mostly linear stress-strain curves. This extra curvature makes the selection of what portion of the curve to linear fit subjective. In order to be consistent, the fits are over the same range of the data as in the stress-strain curves in most cases. In the remaining cases, there are large amounts of initial effects in the radial strain measurements. In these cases, the fit range had to be manually selected.

Of the 14 triaxial tests that were performed, 13 were successful. One core failed under load, and the early data in the test was highly irregular. Table 3 summarizes the results of the mechanical tests on the Eagle Ford shale samples.

Table 3 - Summary of Eagle Ford Mechanical Properties

	Test Count	Average Young's Modulus [psi]	Standard Deviation [psi]	Percent Standard Deviation	Average Poisson's Ratio [-]	Standard Deviation [-]	Percent Standard Deviation
EF1	2	2.36E+06	4.84E+05	20.5%	0.225	0.041	18.4%
EF2	2	2.33E+06	2.35E+05	10.1%	0.212	0.031	14.8%
EF3	2	2.71E+06	4.99E+05	18.4%	0.208	0.023	10.9%
EF4	2	2.02E+06	3.54E+04	1.8%	0.197	0.005	2.7%
EF5	1	2.29E+06	N/A	N/A	0.198	N/A	N/A
EF6	2	2.14E+06	2.28E+05	10.7%	0.209	0.004	1.9%
EF7	2	2.11E+06	2.47E+04	1.2%	0.190	0.013	6.6%
Overall	13	2.28E+06	3.18E+05	14.0%	0.206	0.020	9.8%

There appears to be some variation in the Young's modulus values of the Eagle Ford locations, particularly at what appears to be a high average value of 2.71E06 psi at location EF3. This result was verified by repeating the measurement. This point introduces a large possible range of Young's modulus values in the Eagle Ford. Of course, if the value at EF3 is high due some geologic effect (such as a sample anomaly), the range in the conductivity samples could be significantly less. The apparent differences in Young's Modulus could have a significant effect on conductivity values. On the other hand, the Poisson's ratios are relatively close to each other. It would be very difficult to attribute any conductivity effects to these small differences in Poisson's ratio.

3.1.2 Eagle Ford Mineralogical Composition

In order to determine the mineralogical composition, a combination of XRD and FTIR tests were performed by an outside contractor. The seven Eagle Ford sample locations each had their mineralogy determined. Six of the samples had FTIR analysis performed on them. The seventh sample's composition was determined by XRD analysis to calibrate the FTIR method's results. Table 4 summarizes the data.

Table 4 - Mineralogical Results from Eagle Ford Shale Samples

	Test Type	Clay	Carbonate	Quartz	Feldspar
EF1	FTIR	2%	73%	24%	1%
EF2	FTIR	1%	74%	24%	1%
EF3	FTIR	1%	75%	23%	1%
EF4	XRD	4%	76%	20%	0%
EF5	FTIR	0%	73%	26%	1%
EF6	FTIR	1%	70%	28%	1%
EF7	FTIR	2%	66%	31%	1%
Overall Average		**2%**	**72%**	**25%**	**1%**

Overall, these Eagle Ford outcrop samples are very similar to one another. On the average, they are 72% carbonate and 25% Quartz. In order to give the differences in mineral composition perspective, Figure 16 shows how the values change over the 1,015 feet of the outcrop.

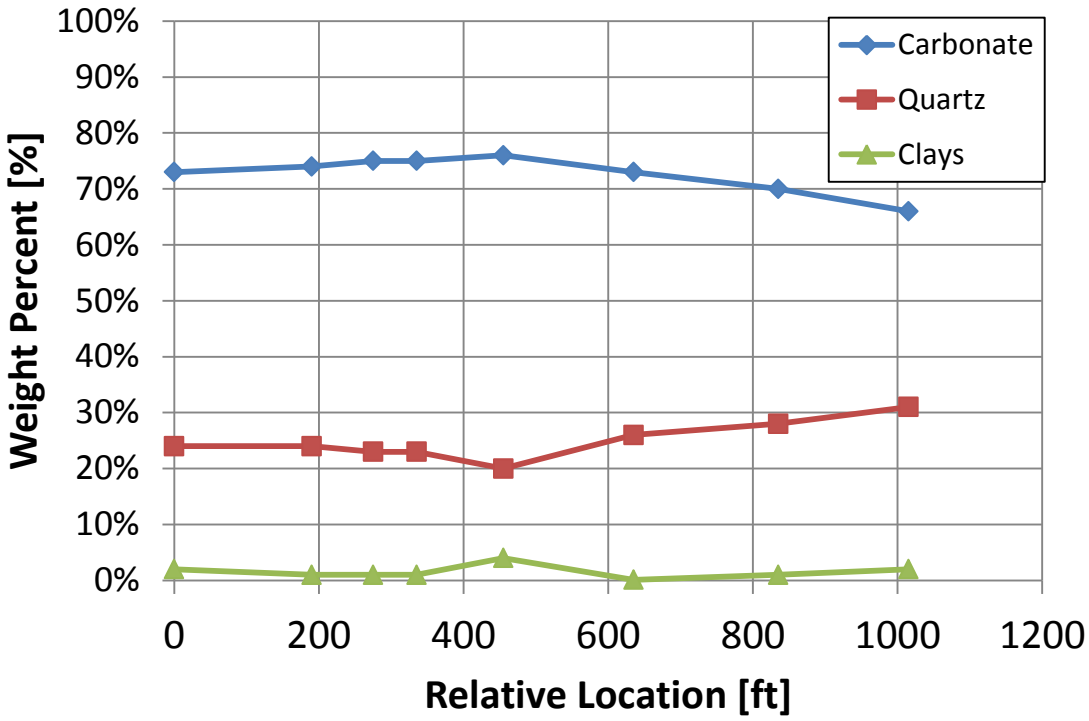

Figure 16 - Eagle Ford mineralogy over outcrop

There is an approximately a 10% decrease of carbonate content and increase of quartz content from EF4 to EF7 along the outcrop. However, the clay content, which is considered to have a large effect on rock behavior, is below 5% at all sample points and has minimal changes as well. There are no drastic composition changes that could have an obvious conductivity effect associated with it, unfortunately.

3.1.3 Eagle Ford Fracture Conductivity Summary

Fracture conductivity tests were performed on samples from each of the seven outcrop locations. The conductivity was measured with no proppant, 0.1 lb/ft^2 areal concentration of 30/50 mesh sand, and 0.2 lb/ft^2 areal concentration of 30/50 mesh sand. Figure 17 shows the average conductivity behavior of the Eagle Ford Shale as a whole. The complete conductivity results from the Eagle Ford testing can be found in Table 5 on the next page (Guzek, 2014). The results of the greatest interest in this study are the unpropped conductivity measurements because they can be directly compared with the unpropped conductivity results from the Fayetteville FL2 and FL3 zones.

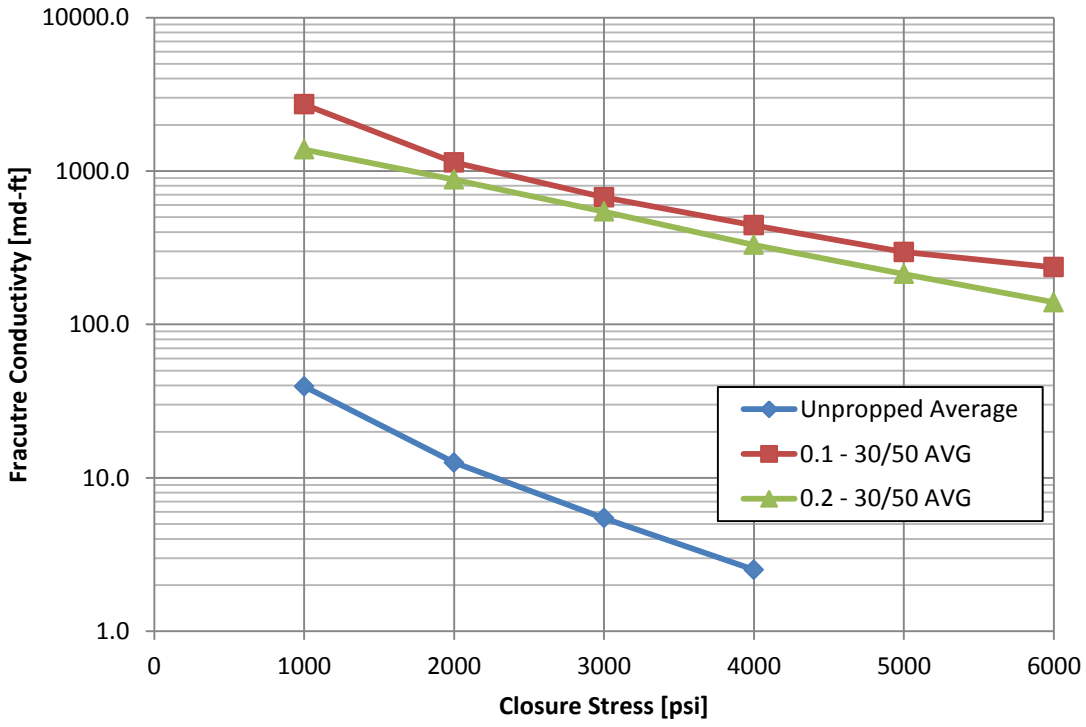

Figure 17 - Average fracture conductivity of Eagle Ford Samples (Guzek, 2014)

Table 5 - Complete Eagle Ford Conductivity Results (Guzek, 2014)

		EF1	EF2	EF3	EF4	EF5	EF6	EF7	Overall Eagle Ford		
Unpropped	**Closure Stress [psi]**	**k_fw_f [md-ft]**	**k_fw_f [md-ft]**	**k_fw_f [md-ft]**	**k_fw_f [md-ft]**	**k_fw_f [md-ft]**	**k_fw_f [md-ft]**	**k_fw_f [md-ft]**	**Avg. k_fw_f [md-ft]**	**Std. Dev. [md-ft]**	**Percent Std. Dev.**
	1000	47.1	122.1	35.5	15.6	17.3	24.7	13.7	39.4	38.4	97.4%
	2000	15.2	35.9	15.6	5.0	5.4	6.6	4.2	12.6	11.4	90.4%
	3000	6.8	15.4	9.4	1.4	1.6	2.4	1.3	5.5	5.4	98.1%
	4000	3.5	4.6	5.9	0.6	0.9	1.6	0.6	2.5	2.1	85.2%

		EF1	EF2	EF3	EF4	EF5	EF6	EF7	Overall Eagle Ford		
0.1 lb/ft^2 30/50 mesh sand	**Closure Stress [psi]**	**k_fw_f [md-ft]**	**k_fw_f [md-ft]**	**k_fw_f [md-ft]**	**k_fw_f [md-ft]**	**k_fw_f [md-ft]**	**k_fw_f [md-ft]**	**k_fw_f [md-ft]**	**Avg. k_fw_f [md-ft]**	**Std. Dev. [md-ft]**	**Percent Std. Dev.**
	1000	2936	3705	3683	1642	1947	3508	1597	2717	964.8	35.5%
	2000	1292	1487	1398	723	1014	1343	706	1138	323.8	28.5%
	3000	850	778	753	415	750	763	411	674	181.8	27.0%
	4000	511	515	502	280	584	432	274	443	121.4	27.4%
	5000	336	375	319	198	362	285	198	296	72.9	24.6%
	6000	242	287	252	190	262	242	177	236	39.2	16.6%

		EF1	EF2	EF3	EF4	EF5	EF6	EF7	Overall Eagle Ford		
0.2 lb/ft^2 30/50 mesh sand	**Closure Stress [psi]**	**k_fw_f [md-ft]**	**k_fw_f [md-ft]**	**k_fw_f [md-ft]**	**k_fw_f [md-ft]**	**k_fw_f [md-ft]**	**k_fw_f [md-ft]**	**k_fw_f [md-ft]**	**Avg. k_fw_f [md-ft]**	**Std. Dev. [md-ft]**	**Percent Std. Dev.**
	1000	1200	1292	998	2067	644	1780	1680	1380	491.6	35.6%
	2000	777	920	639	1320	425	1167	914	880	304.0	34.5%
	3000	554	551	445	840	326	591	505	545	157.5	28.9%
	4000	375	365	337	460	221	317	237	330	82.7	25.0%
	5000	209	246	245	343	132	159	157	213	72.6	34.1%
	6000	125	167	198	177	74	114	122	140	42.9	30.7%

3.2 Fayetteville FL2 Results

Fayetteville shale FL2 zone results are not associated with a particular fracture conductivity measurement like they are in the Eagle Ford. Due to this limitation, results are used as a representation of the overall FL2 outcrop samples. The samples for testing were taken from several rocks from the same location.

3.2.1 Fayetteville FL2 Mechanical Properties

Triaxial compression tests were successfully performed on three FL2 core specimens. These cores were tested up to a deviator stress of 30 MPa. These cores were fragile and it was not possible cut the cores to the required tolerances. All of the tested cores had at least one small fracture that was parallel to the bedding planes. These fractures would be compressed by the axial load during testing. This fragility prevented tolerance testing. Overall, the tested cores seemed to have flat, parallel ends, and the samples appeared round. Due to the outcrop sample limitations, there was a limit to the number of cores that could be attempted to be cut. The best three cores were tested. These cores were the most stable, and visually appeared to be close to the tolerances.

Each core took three full load cycles in order to determine the elastic properties. The first load involved a large amount of plastic deformation. This plastic deformation was caused by a combination of the imperfect sample shape and the small fractures being compressed. On the next loadings, the deformation behavior appeared to be much more elastic. Figure 18 and Figure 19 show an example of the stress-strain and axial-radial strain

curves for FL2 samples. Appendix B contains the full results of the FL2 mechanical testing. Table 6 summarizes the complete mechanical property results for FL2.

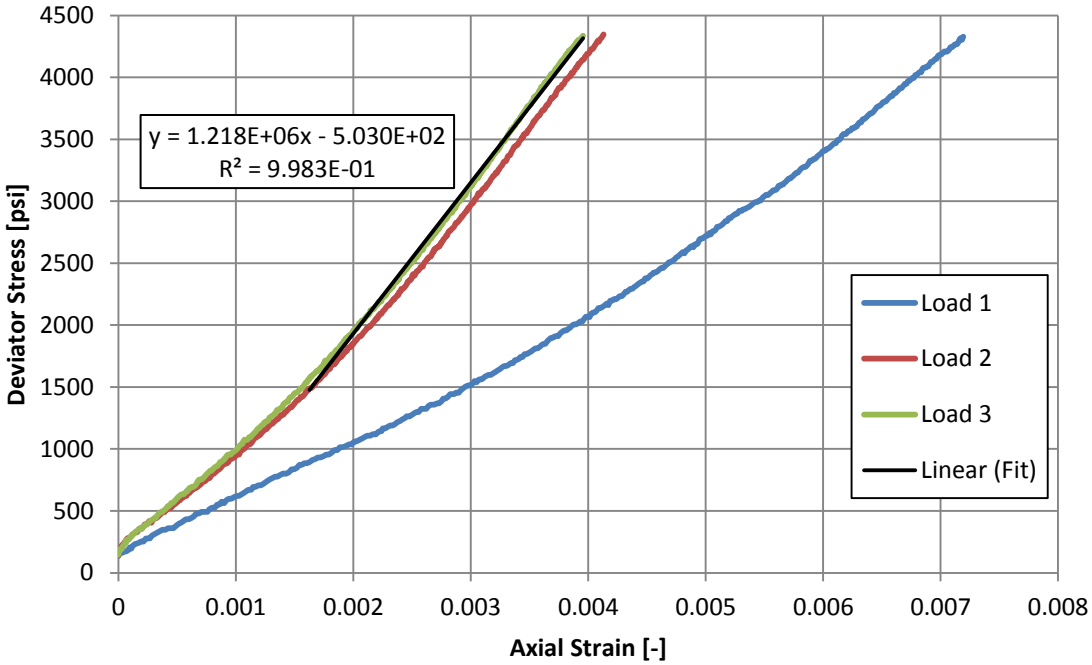

Figure 18 - Stress-strain curves for FL2(2)

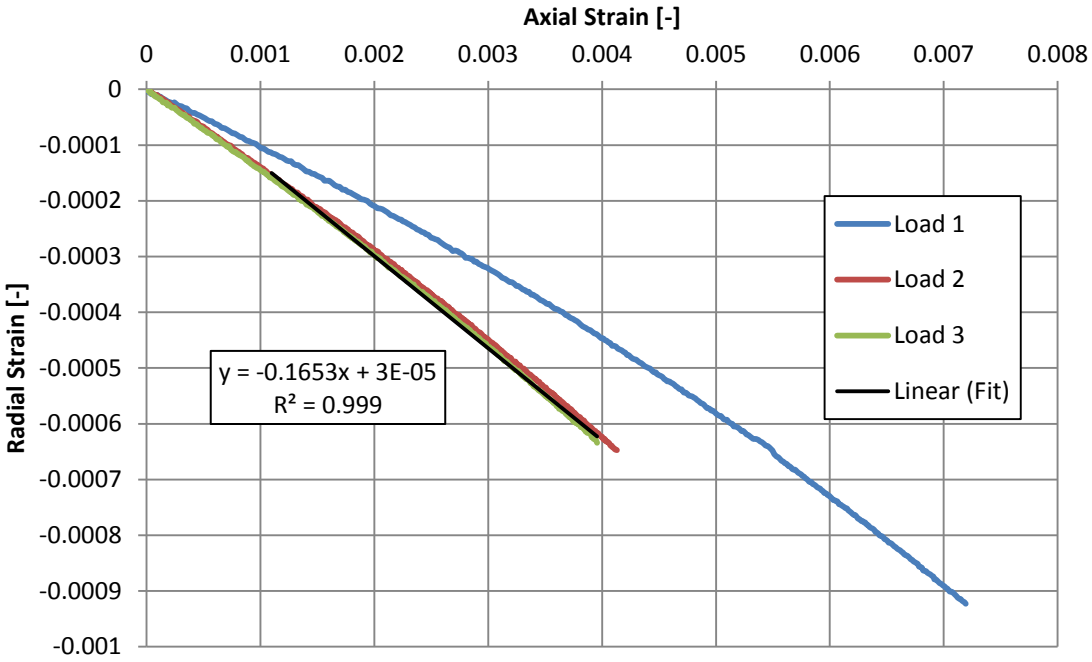

Figure 19 - Axial-radial strain curves for FL2(2)

Table 6 - Complete Mechanical Property Results for Fayetteville FL2

		Young's Modulus [psi]	Poisson's Ratio [-]
Samples	FL2 (1)	1.09E+06	0.185
	FL2 (2)	1.22E+06	0.165
	FL2 (3)	1.26E+06	0.133
Overall	Average	1.19E+06	0.161
	Std. Dev.	8.98E+04	0.026
	% Std. Dev.	7.56%	16.4%

3.2.2 Fayetteville FL2 Mineralogical Composition

In order to determine the average mineralogical composition of the Fayetteville FL2 zone, 4 FTIR tests were performed with one XRD test to calibrate the results. Samples for testing were taken directly from old conductivity samples. On the average, the FL2 samples are mostly Quartz and Clay. The results are summarized in Table 7.

Table 7 - Fayetteville FL2 Mineralogical Composition Results

	Test Type	Clay	Carbonate	Quartz	Feldspar
1	FTIR	36%	1%	57%	6%
2	FTIR	39%	2%	54%	5%
3	FTIR	37%	1%	57%	5%
4	FTIR	34%	4%	57%	5%
5	XRD	42%	0%	55%	5%
Overall Average		**38%**	**2%**	**56%**	**5%**

3.2.3 Fayetteville FL2 Fracture Conductivity Summary

Fracture conductivity tests were performed on four FL2 samples. Tests were run with unpropped fractures and propped fractures with 0.03 lb/ft^2 and 0.1 lb/ft^2 areal concentrations of 30/70 mesh sand. In each proppant grouping, three of the tests gave similar results, while the fourth result was significantly different than the other three and considered to be erroneous. Figure 20 shows the average conductivity behavior of the three successful conductivity measurements at all three proppant concentrations. Table 8 shows

the complete fracture conductivity results for the FL2 zone (Briggs, 2014). The red data was excluded from all analysis because of experimental failure.

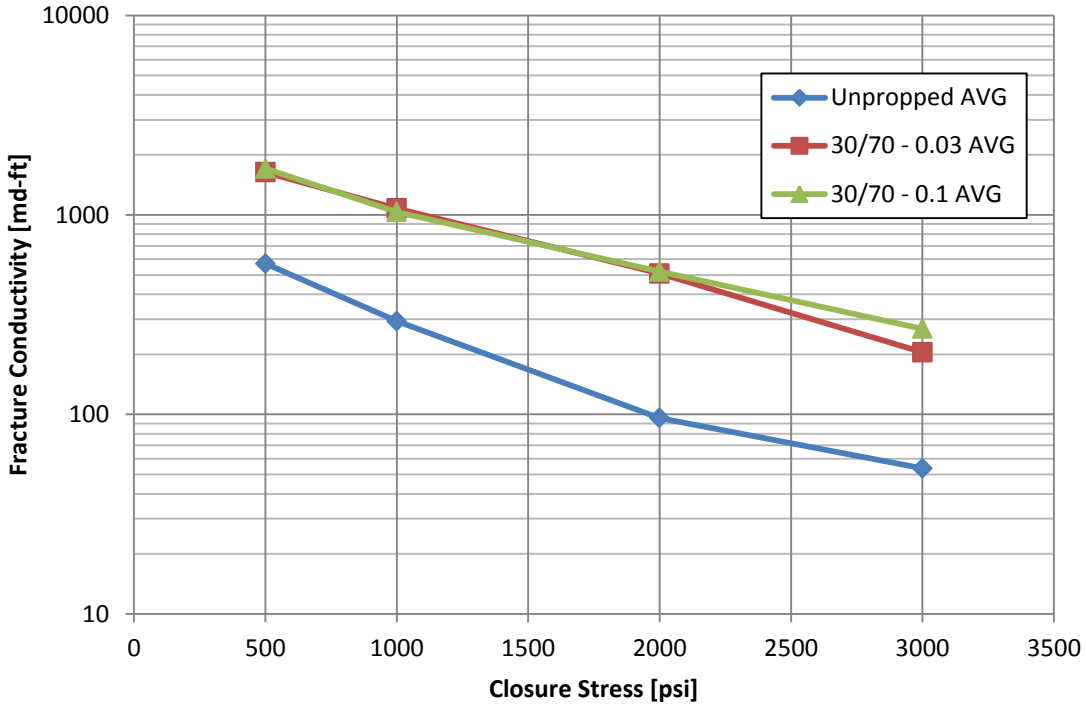

Figure 20 - Average fracture conductivity of Fayetteville FL2 samples (Briggs, 2014)

Table 8 - Complete Fayetteville FL2 Conductivity Data (Briggs, 2014)

		F13	F14	F17	F19	Overall Fayetteville FL2		
Unpropped	Closure Stress [psi]	k_fw_f [md-ft]	k_fw_f [md-ft]	k_fw_f [md-ft]	k_fw_f [md-ft]	Avg. k_fw_f [md-ft]	Std. Dev. [md-ft]	Percent Std. Dev.
	500	N/A	640	601	468	570	90.3	15.9%
	1000	1204	346	354	179	293	98.2	33.5%
	2000	212	92	128	67	96	30.7	32.1%
	3000	52	39	81	41	54	24.2	45.1%

		F13	F14	F17	F19	Overall Fayetteville FL2		
0.03 lb/ft^2 30/70 mesh	Closure Stress [psi]	k_fw_f [md-ft]	k_fw_f [md-ft]	k_fw_f [md-ft]	k_fw_f [md-ft]	Avg. k_fw_f [md-ft]	Std. Dev. [md-ft]	Percent Std. Dev.
	500	1294	141	2061	1555	1637	389.9	23.8%
	1000	856	92	1410	966	1078	293.4	27.2%
	2000	445	41	610	470	508	89.0	17.5%
	3000	187	29	212	216	205	16.0	7.8%

		F13	F14	F17	F19	Overall Fayetteville FL2		
0.1 lb/ft^2 30/70 mesh	Closure Stress [psi]	k_fw_f [md-ft]	k_fw_f [md-ft]	k_fw_f [md-ft]	k_fw_f [md-ft]	Avg. k_fw_f [md-ft]	Std. Dev. [md-ft]	Percent Std. Dev.
	500	2035	1779	N/A	1308	1707	368.7	21.6%
	1000	1032	1126	1930	946	1035	90.4	8.7%
	2000	467	518	999	572	519	52.7	10.1%
	3000	223	249	631	334	269	58.5	21.8%

3.3 Fayetteville FL3 Zone Results

The Fayetteville FL3 samples came from a single location, so the measured rock properties are associated with the zone as a whole and not a particular fracture conductivity measurement. In this regard, the FL3 is the same as the FL2. These results will be compared with the overall Eagle Ford and the FL2 results.

3.3.1 Fayetteville FL3 Mechanical Properties

Triaxial tests were very difficult to perform on the FL3 core specimens. The FL3 outcrop samples are extremely laminated, and very prone to falling apart along those laminations. As such, it took five attempts just to run two tests, with much more bulk rock to cut five somewhat-stable cores. The core specimens that the tests were able to be run on did not meet the defined tolerances for cylindrical test specimens. The samples were rough on the cylinder ends because any shear force (such as sanding or grinding) would result in the whole layer coming off. The samples also could not be rounded properly without causing total sample failure. As soon as an FL3 core was unsealed from its protective packaging, the sample's length and diameter were quickly measured, and the rock was placed in the heat shrink wrap. Only two of the samples were able to survive this process and actually have a triaxial test performed on them.

In addition to only testing two cores, the triaxial tests of these cores were very difficult to perform. At initial loading, there appeared to be an uncontrolled strain. This was due to both the excessive laminations of the core samples and the rough ends being compressed. This uncontrolled strain would occur the first time the sample experienced a certain deviator stress level. On subsequent loadings, a repeatable elastic trend was visible in the stress range that the rock had already experienced. When the rock exceeded that stress, the uncontrolled strain would start again. In order to ensure safe experimentation, the maximum axial strain on a load cycle was manually limited to around 1%. After reaching 1% axial strain, the sample was unloaded back to the contact stress, and the sample dimensions were updated. Then, the sample would be loaded

again until a 1% strain was reached. This process was repeated until the LVDT range was exceeded due to the excessive sample deformation. This meant that the desired maximum deviator stress of 30 MPa could not be reached. Figure 21 shows an example of an FL3 stress-strain curve.

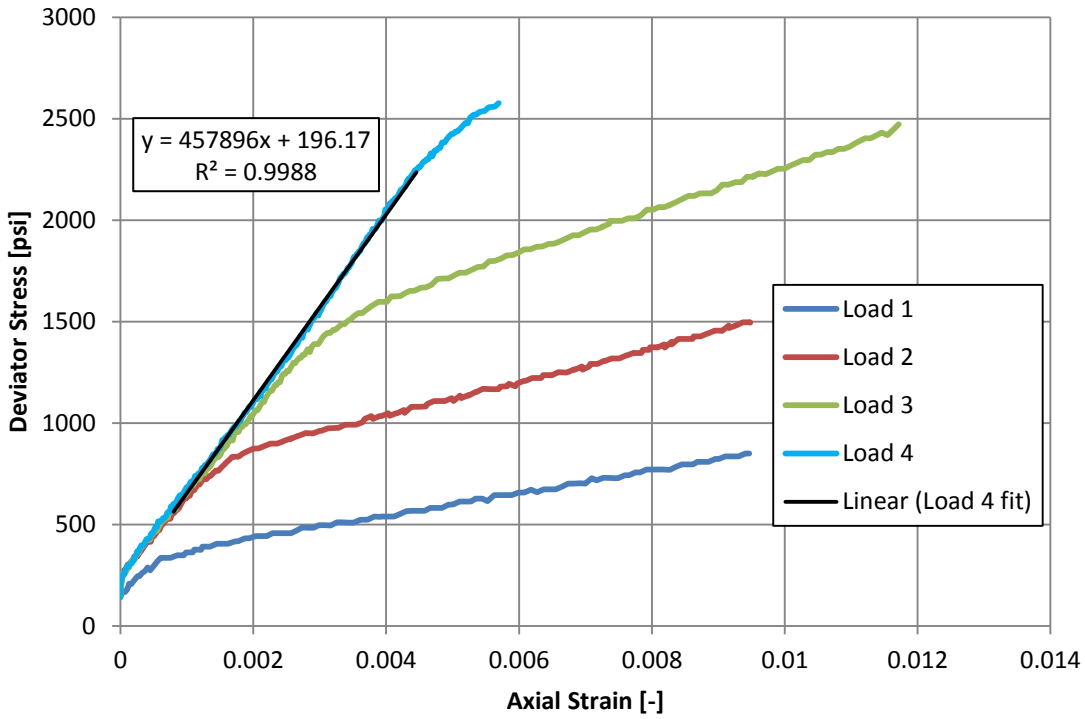

Figure 21 - Stress-strain curves for FL3(2)

In order to determine the Poisson's Ratio, the curve fit of the axial-radial strain curve had to be performed differently than in the Eagle Ford and FL2. Instead of fitting the linear portion of the curve at the end of the last loading phase, the fit is performed on

the portion toward the beginning of the curve that corresponds with the elastic behavior on the stress-strain curves. This gave a reasonable value for the Poisson's ratio. Figure 22 shows the axial-radial strain curves for an FL3 sample. Appendix C contains the full results of the FL3 mechanical testing. Table 9 summarizes the mechanical property results for FL3. It is less than ideal to only have two data points to represent the entirety of the FL3 zone, but it was essentially unavoidable.

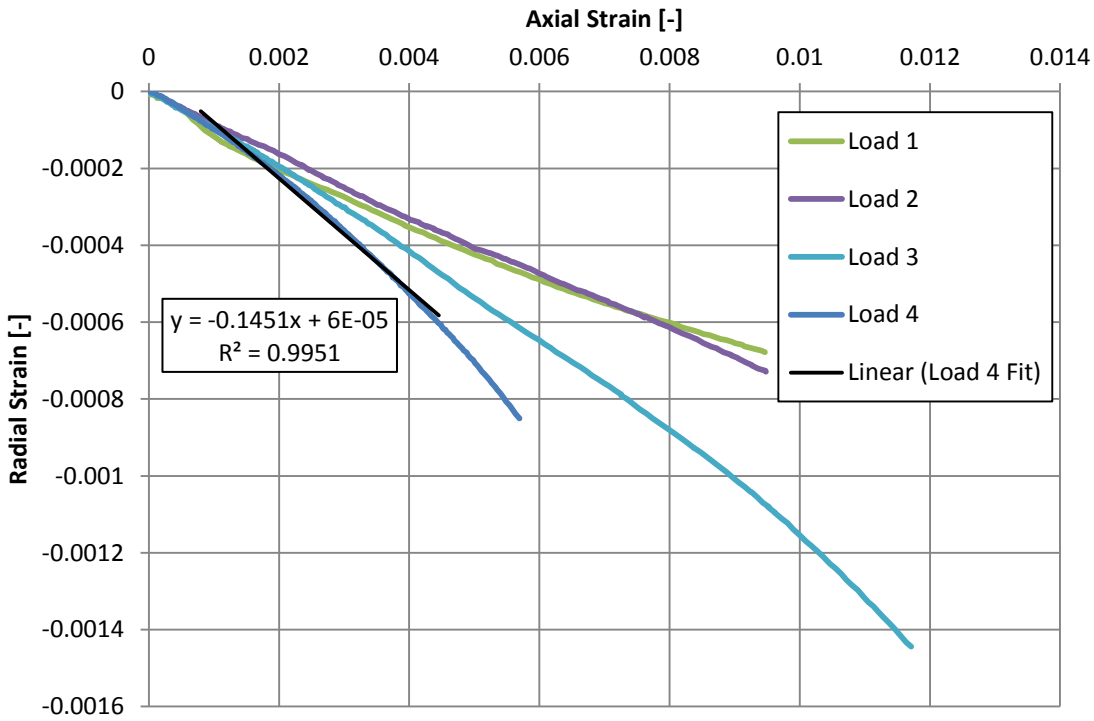

Figure 22 - Axial-radial strain curves for FL3(2)

Table 9 - Complete Mechanical Property Results for Fayetteville FL3

	Young's Modulus [psi]	Poisson's Ratio [-]
FL3 (1)	5.16E+05	0.167
FL3 (2)	4.58E+05	0.145
Average	4.87E+05	0.156
Std. Dev.	4.11E+04	0.015
% Std. Dev.	8.44%	9.9%

3.3.2 Fayetteville FL3 Mineralogical Composition

The mineralogical composition of the FL3 was determined in the same way as the FL2: with 4 FTIR tests and 1 XRD test for model calibration. The results were used to determine the average mineral content in the FL3 zone. Samples were taken from old conductivity samples. Table 10 summarizes the results.

Table 10 - Fayetteville FL3 Mineralogical Composition Results

	Test Type	Clay	Carbonate	Quartz	Feldspar
1	FTIR	26%	33%	37%	4%
2	FTIR	35%	28%	35%	2%
3	FTIR	34%	31%	33%	2%
4	FTIR	38%	28%	32%	2%
5	XRD	10%	38%	50%	2%
Overall Average		**29%**	**32%**	**37%**	**2%**

3.3.3 Fayetteville FL3 Fracture Conductivity Summary

The FL3 conductivity experiments were performed with the same parameters as the FL2 conductivity experiments in order to compare the vertical differences between the two zones. Both unpropped and propped (0.03 lb/ft^2 and 0.1 lb/ft^2 areal concentration of 30/70 sand) experiments were performed. Four conductivity tests were performed at each proppant concentration level. Figure 23 shows the average conductivity for the FL3 zone. Table 11 shows the complete conductivity data for the FL3 zone (Briggs, 2014).

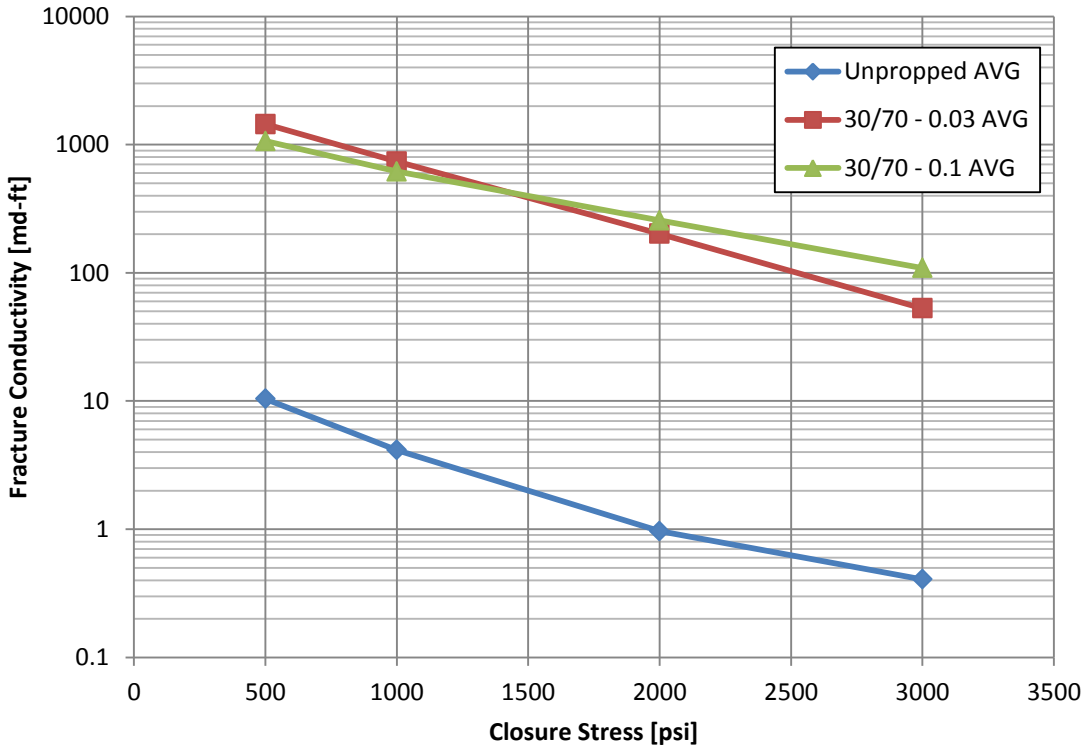

Figure 23 - Average conductivity values in Fayetteville FL3 zone (Briggs, 2014)

Table 11 - Complete Fayetteville FL3 Conductivity Data (Briggs, 2014)

		F02	F03	F04	F15	F16	Overall Fayetteville FL3		
Unpropped	Closure Stress [psi]	k_fw_f [md-ft]	k_fw_f [md-ft]	k_fw_f [md-ft]	k_fw_f [md-ft]	k_fw_f [md-ft]	Avg. k_fw_f [md-ft]	Std. Dev. [md-ft]	Percent Std. Dev.
	500	11.3	17.0	2.9	254.2	N/A	10.4	7.1	68.2%
	1000	3.5	7.1	1.8	75.6	N/A	4.1	2.7	66.1%
	2000	0.8	1.6	0.6	20.5	N/A	1.0	0.5	56.1%
	3000	0.3	0.5	0.5	8.4	N/A	0.4	0.1	34.5%

		F02	F03	F04	F15	F16	Overall Fayetteville FL3		
0.03 lb/ft^2 30/70 mesh	Closure Stress [psi]	k_fw_f [md-ft]	k_fw_f [md-ft]	k_fw_f [md-ft]	k_fw_f [md-ft]	k_fw_f [md-ft]	Avg. k_fw_f [md-ft]	Std. Dev. [md-ft]	Percent Std. Dev.
	500	823	N/A	1654	1965	1336	1444	487.4	33.7%
	1000	530	N/A	655	1250	511	737	348.4	47.3%
	2000	156	N/A	193	357	100	201	110.6	54.9%
	3000	46	N/A	69	65	31	53	17.9	33.9%

		F02	F03	F04	F15	F16	Overall Fayetteville FL3		
0.1 lb/ft^2 30/70 mesh	Closure Stress [psi]	k_fw_f [md-ft]	k_fw_f [md-ft]	k_fw_f [md-ft]	k_fw_f [md-ft]	k_fw_f [md-ft]	Avg. k_fw_f [md-ft]	Std. Dev. [md-ft]	Percent Std. Dev.
	500	380	N/A	969	2126	787	1065	748.7	70.3%
	1000	257	N/A	588	1189	436	618	404.4	65.5%
	2000	137	N/A	257	472	159	256	153.0	59.7%
	3000	84	N/A	128	148	76	109	34.7	31.8%

3.4 Effect of Rock Properties on Fracture Conductivity

In order to best understand the effect of rock properties on fracture conductivity, it is important to first quantify the differences in rock properties across the three distinct zones. Table 12 summarizes the mechanical properties of the three zones and Figure 24 shows the differences in the mineralogy of the three zones.

Table 12 - Average Mechanical Properties of the Three Zones

	# of Samples	Young's Modulus		Poisson's Ratio	
		Average [psi]	% Std. Dev.	Average [-]	% Std. Dev.
Eagle Ford	13	2.28E+06	14.0%	0.21	9.8%
FL2	3	1.19E+06	7.6%	0.16	16.4%
FL3	2	4.87E+05	8.4%	0.16	9.9%

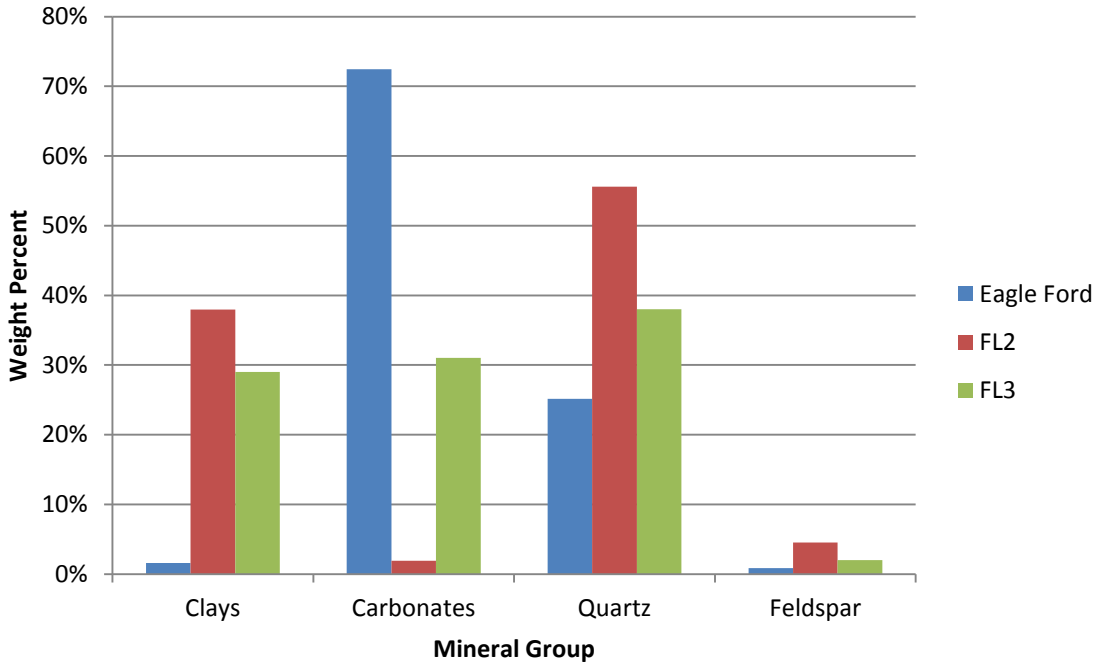

Figure 24 - Average mineral composition of the three zones

Each of the three zones has a distinct Young's Modulus and mineralogy. The Eagle Ford has the highest Young's Modulus by a factor of 2 over FL2 and a factor of 5 over FL3. The Eagle Ford also has the highest Poisson's Ratio. The Fayetteville zones do have approximately the same Poisson's Ratio which is about 75% of the Poisson's Ratio of the Eagle Ford. The mineral composition of the Eagle Ford is mostly carbonates with some quartz, while the FL2 is mostly quartz with a large amount of clays and the FL3 is relatively evenly split between quartz, carbonates, and clays.

3.4.1 Effect of Rock Properties on Unpropped Fracture Conductivity

The best place to start in this analysis is the unpropped fracture conductivities of the three zones. In these measurements, the only factors are the rock properties. Figure 25 shows the average unpropped fracture conductivities of the three zones.

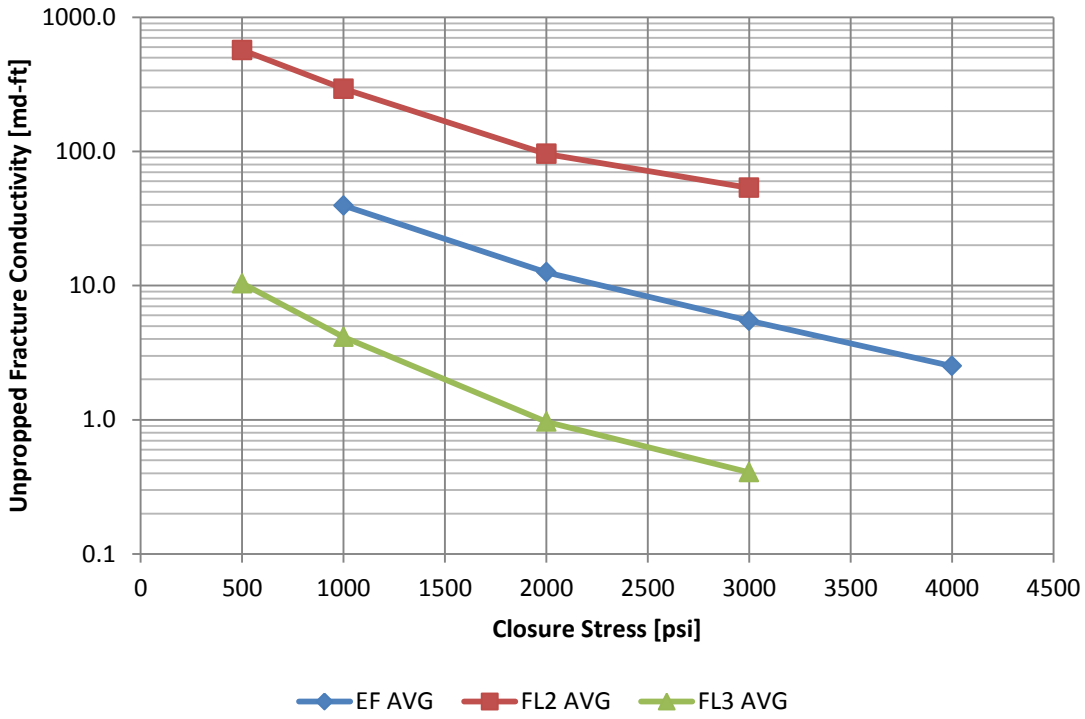

Figure 25 - Average unpropped fracture conductivities of the three zones

The average unpropped conductivities for the three zones are distinct from one to another. The Fayetteville FL2 has by far the highest unpropped conductivity. The Eagle Ford conductivity is one order of magnitude below FL2, and the FL3 conductivity is an

order of magnitude below the Eagle Ford. This fact cannot be explained by any one rock characteristic. There were numerous failed attempts at correlating the fracture conductivity as a function of the rock characteristics. As such, this direction was quickly abandoned because there must be another factor controlling the unpropped conductivity.

According to the literature, the unpropped fracture conductivity is heavily related to fracture surface properties such as initial flow aperture, surface roughness, and asperity size and strength (Makurat, 1996). A visual inspection of the fracture surfaces of samples from each of the three zones showed that there are significant differences in surface topography. When a fresh FL2 sample was fractured, large particles broke off from the rough fracture surface and remained in the fracture for the unpropped test. The Eagle ford sample is smoother than the FL2 sample, but has noticeable asperities all along the surface. The FL3 sample is extremely flat with only surface roughness causing any variation in the fracture surface. Figures 26, 27, and 28 show photos of the fracture surfaces of Eagle Ford, FL2, and FL3, respectively.

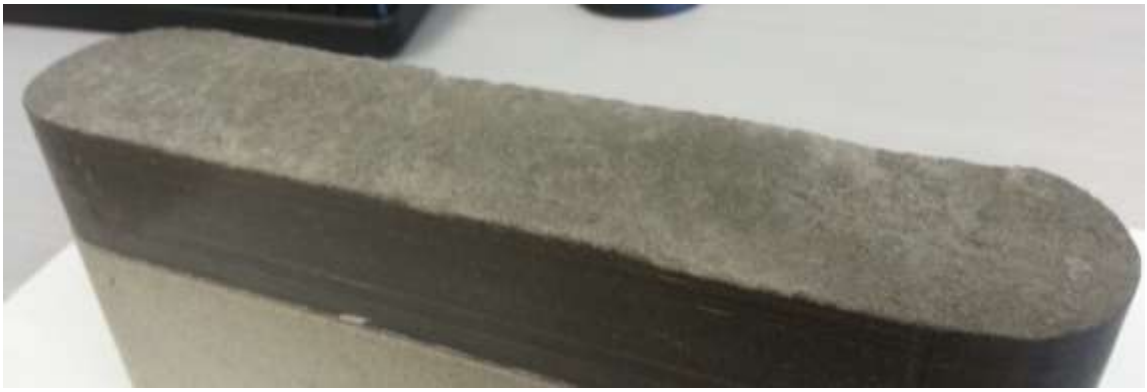

Figure 26 - Eagle Ford fracture surface

Figure 27 - FL2 fracture surface

Figure 28 - FL3 fracture surface

In order to quantify the surface topography, scans of the conductivity sample fracture surfaces were performed with a laser profilometer. These scans provided a series of thickness measurements over the entire fracture surface. These measurements do not account for a fracture surface that is skewed from the horizontal plane. In order to account for this, the best-fit plane through the fracture surface was determined by a least-squares regression. The deviation of the actual fracture surface from this best-fit plane is an excellent representation of fracture surface roughness. This deviation was quantified by the Root Mean Square (RMS) error of the fit. Table 13 summarizes the results of the scans.

Table 13 - Surface Profilometer Scan Results

	Z-axis measurement Distribution	
	Average [in]	RMS Error [in]
Eagle Ford	0.89383	0.01035
FL2	0.82391	0.05914
FL3	0.01464	0.00049

The profilometer results confirm that there are drastic differences in the surface topography of fractures in the three zones. The FL2 has the roughest fracture surfaces of the three zones. This, combined with the large pieces of loose shale that remained in the fracture during the unpropped conductivity tests, results in the highest unpropped

fracture conductivity. The Eagle Ford is significantly smoother than FL2, and has lower unpropped fracture conductivity. The FL3 sample was extremely flat, and as a result, has the lowest fracture conductivity of the three zones. If the two pieces of a fractured sample were to fit perfectly together, the surface roughness would likely cause a negative effect on conductivity by forcing the fluid to flow over peaks as opposed to straight through. However, these samples do not fit perfectly. Any slight shear displacement (even unintended) or partial fracture surface degradation due to particle transfer during the physical fracturing process would create significantly larger flow paths in a rougher fracture. In the FL3, the only flow paths that can be created in an unpropped fracture are created by the small, localized surface roughness.

In order to best quantify the relationship between rock mechanical properties and fracture conductivity, the effect of closure stress on the conductivity was investigated. By definition, the Young's Modulus and Poisson's Ratio describe how a material deforms under increasing stress. A sample with a higher Young's Modulus would be expected to better maintain flow channels than a softer sample (given the same surface characteristics). The sample also likely has a higher compressive strength before yielding, which resists permanent deformation. In order to investigate the effect of Young's Modulus on fracture conductivity, the two Fayetteville zones FL2 and FL3 were compared. These zones were determined to have different Young's Modulus, yet very similar Poisson's ratios. This should isolate the effect of Young's Modulus. Figure 29 shows the average unpropped fracture conductivities of the FL2 and FL3.

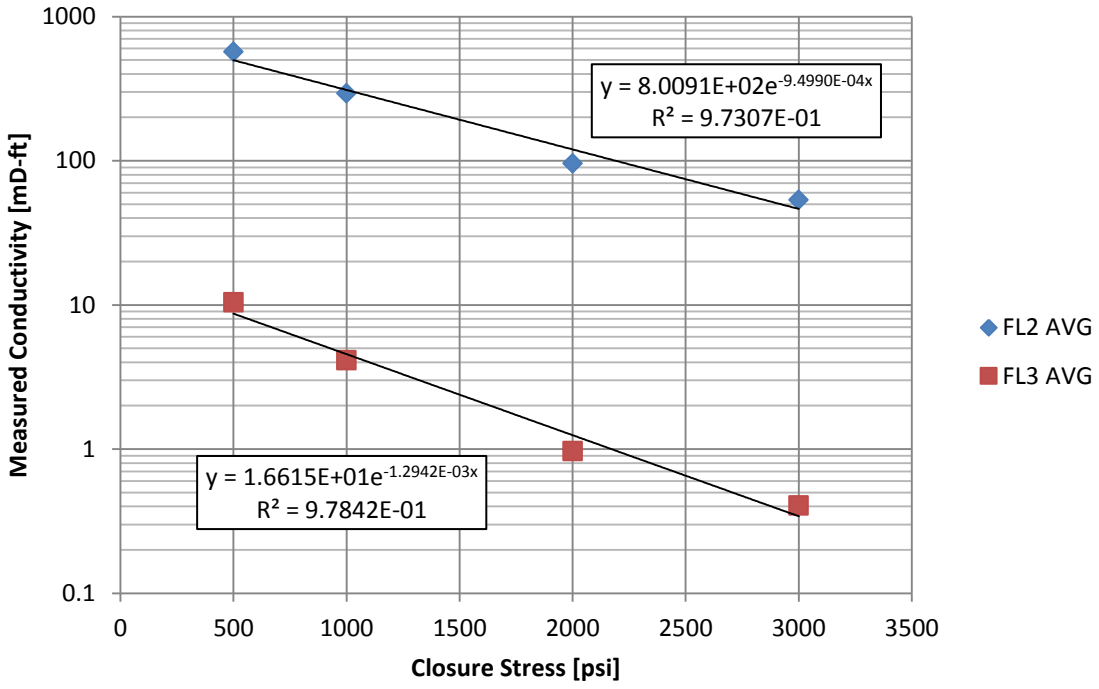

Figure 29 - Average unpropped fracture conductivity of FL2 and FL3 with exponential fits

The conductivity loss with increasing closure stress is approximately linear on a semi-log plot. For this reason, an exponential decline trendline was selected to describe the behavior over the tested closure stress range. These trendlines have the following form:

$$(k_f w_f) \cong (k_f w_f)_0 e^{-\lambda \sigma_c} \quad \text{.....(3-1)}$$

where $(k_f w_f)_0$ is an estimate for the fracture conductivity under no load, σ_c is the closure stress (in psi), and λ is the exponential decline constant (in psi^{-1}). These trendlines are not meant to extrapolate beyond the curve fit. The conductivity behavior

likely deviates greatly from the trend as closure stress approaches 0 psi or increases past 3000 psi. The exponential decline constant is what is of greatest interest in this study.

Based on the curve fits in Figure 29, the unpropped decline constant of FL2 (9.5E-04 psi^{-1}) is smaller than that of FL3 (1.29E-03 psi^{-1}). This supports the idea that a higher Young's Modulus lowers the decline rate of the conductivity. Because there are only 3 samples included in each of the unpropped conductivity data sets, it is important to verify that this effect is not being caused by a single sample's results skewing the perceived decline constants. The decline constant for each individual conductivity experiment was determined. Figure 30 shows the distribution of these decline constants for FL2 and FL3 unpropped fractures. The error bars are +/- one standard deviation.

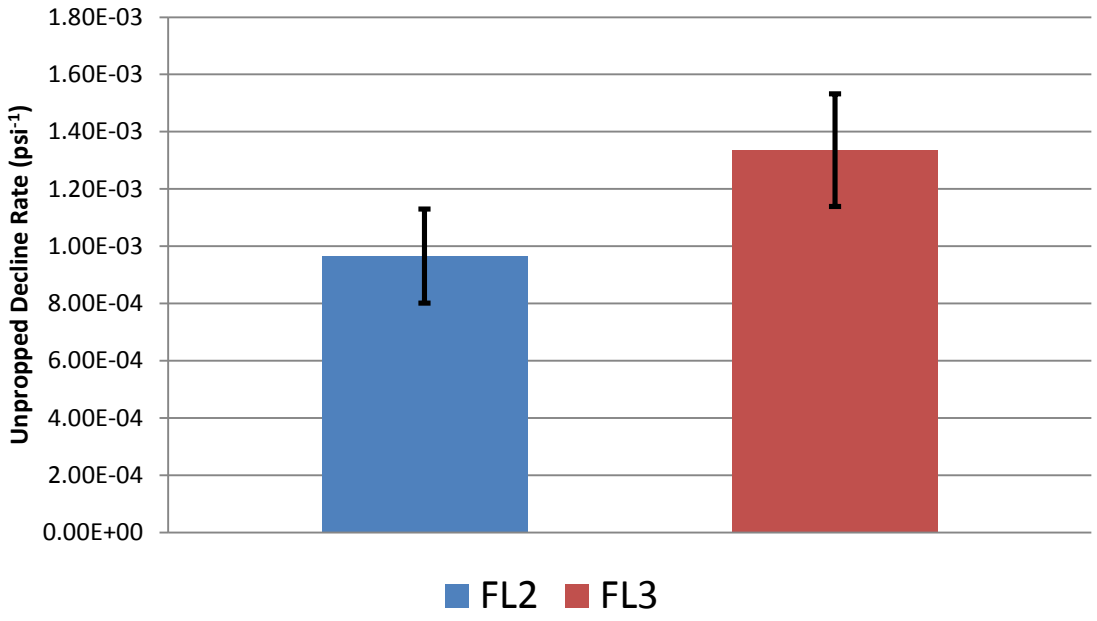

Figure 30 - Decline rate constant distributions for unpropped FL2 and FL3 fractures

Looking at the individual sample decline rates shows that there is a difference between the two decline rate distributions. This suggests that a higher Young's Modulus does reduce the rate at which conductivity is lost as closure stress increases. Quantifying the exact effect is not possible with this data due to the surface topography differences between FL2 and FL3. The extra roughness on the FL2 surfaces suggests that the contact area between the two fracture faces is actually less than in FL3. This suggests that the slope difference caused by the difference in Young's Modulus could be greater in reality than is seen in these experiments because the actual stress in the rock at the contact points is higher in FL2. Even without accounting for topography differences, this small difference in decline rate could result in significant difference in conductivity at higher closure stresses. Figure 31 shows a theoretical example that assumes a $(k_f w_f)_0$ of 1 for a "hard" and a "soft" rock using the decline rates from the FL2 and FL3 average conductivity curve fits. The graph also shows the conductivity improvements at 3000, 4000, and 6000 psi. What appears to be a small change in decline rate can actually result in almost doubling fracture conductivity at 3000 psi.

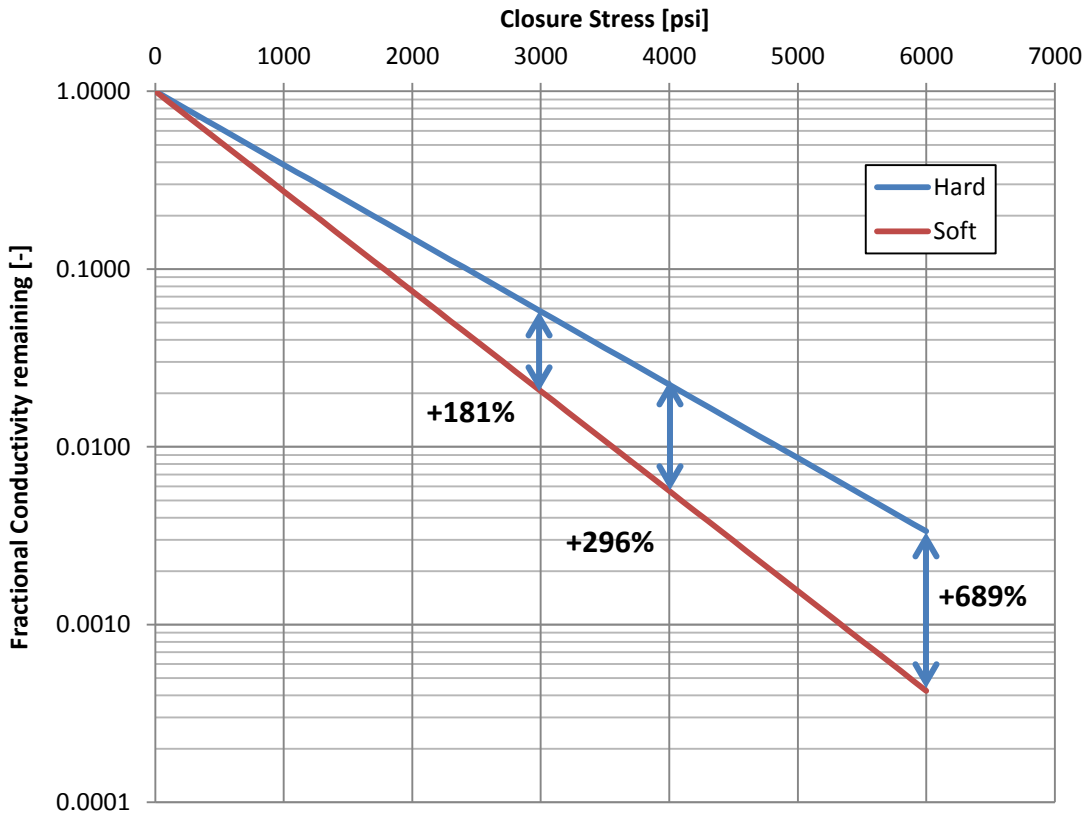

Figure 31 - Potential conductivity improvements from a small decrease in decline rate

Next, the Eagle Ford unpropped conductivity results are incorporated into the existing analysis. The Eagle Ford's Young's modulus is approximately twice as large as the FL2 Young's Modulus. However, the Poisson's Ratio is larger than those in the Fayetteville. In order to make a valid comparison, only unpropped data in the overlapping closure stress range of 1000 - 3000 psi will be examined. The Fayetteville data at 500 psi and the Eagle Ford data at 4000 psi will be excluded. Figure 32 shows the exponential curve fits of the overlapping unpropped conductivity data.

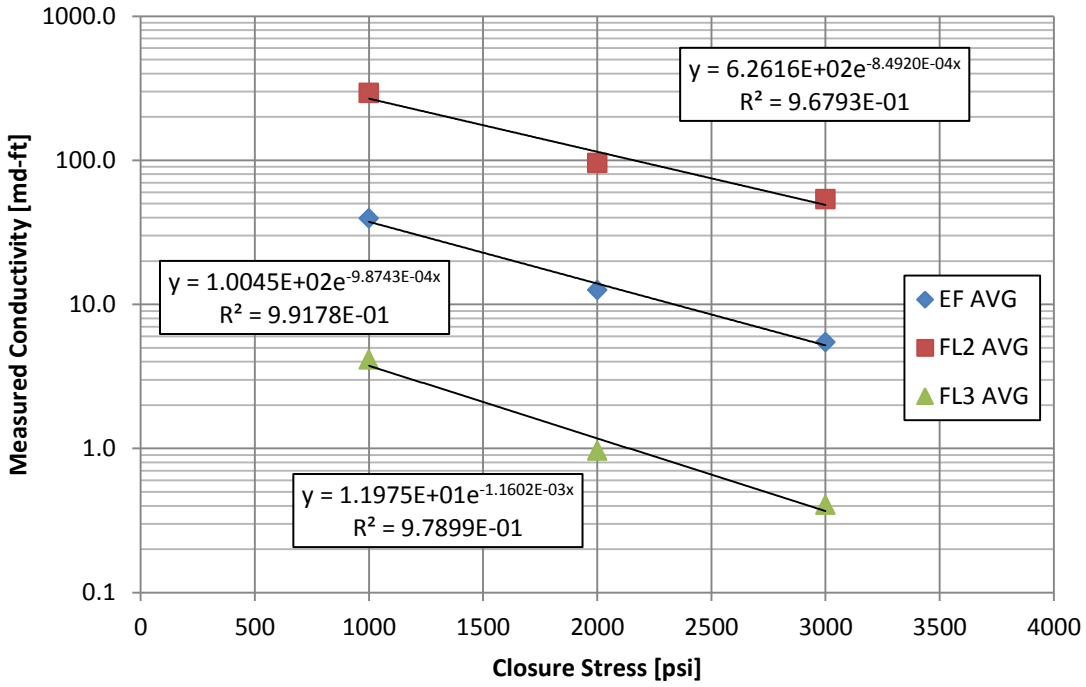

Figure 32 - Overlapping average unpropped conductivity data with exponential fits

Even though the Eagle Ford has a higher Young's Modulus, it does not have the slowest decline rate. Its decline rate is in between that of the FL2 and FL3, which is somewhat surprising. Figure 33 shows the distributions of the decline rates from the three zones. The error bars are +/- one standard deviation.

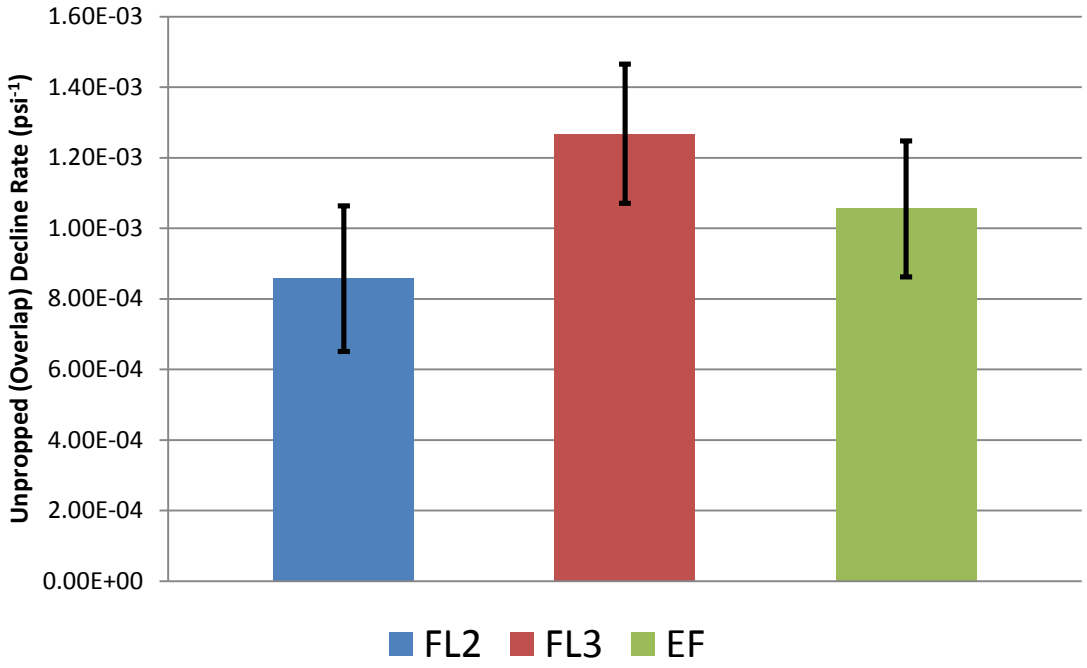

Figure 33 - Decline rate distributions for unpropped (overlap) FL2, FL3, and Eagle Ford fractures

The distribution of the seven unpropped conductivity test decline rates is in between the FL2 and FL3. It is possible that the higher Poisson's Ratio is causing flow channels to close faster perpendicular to the closure stress than in the Fayetteville samples. However, without having a test that isolates the Poisson's Ratio effect, this conclusion may not be valid. Based on these experiments, it is reasonable to say that a higher Young's Modulus lowers the loss of fracture conductivity with increasing closure stress in unpropped fractures. Other effects from sample topography and Poisson's Ratio on the decline rate are still undetermined.

3.4.2 Effect of Rock Properties on Propped Fracture Conductivity

It is already known that factors such as proppant size, strength, and areal concentration have a significant effect on propped fracture conductivity. These variables must be held constant in order to make a valid comparison. As such, for this stage of the analysis, only the two Fayetteville zones have valid comparisons on the cross-zone scale. They were tested with 0.03 lb/ft^2 and 0.1 lb/ft^2 of 30/70 mesh sand for their propped conductivity measurements. With a 0.03 lb/ft^2 areal concentration of 30/70 mesh sand, an approximate proppant monolayer is present on the fracture surface. This eliminates most proppant pack compression effects from conductivity loss. Instead, the majority of conductivity loss will be due to proppant embedment until the closure stress is high enough to cause rock-on-rock interactions again. Figure 34 shows the average propped conductivity values for 0.03 lb/ft^2 of 30/70 on FL2 and FL3. Due to the limited sample size, Figure 35 compares the distribution of the individual sample decline rates to confirm the decline rate difference. The error bars are +/- one standard deviation.

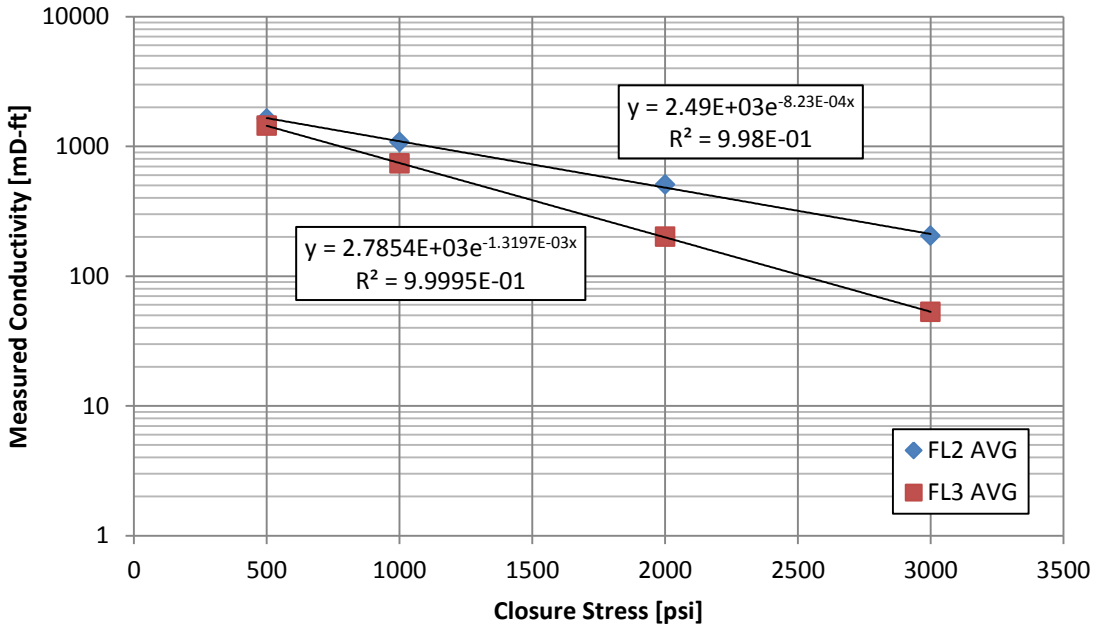

Figure 34 - 0.03 lb/ft^2 - 30/70 mesh average conductivities with exponential fits for FL2 and FL3

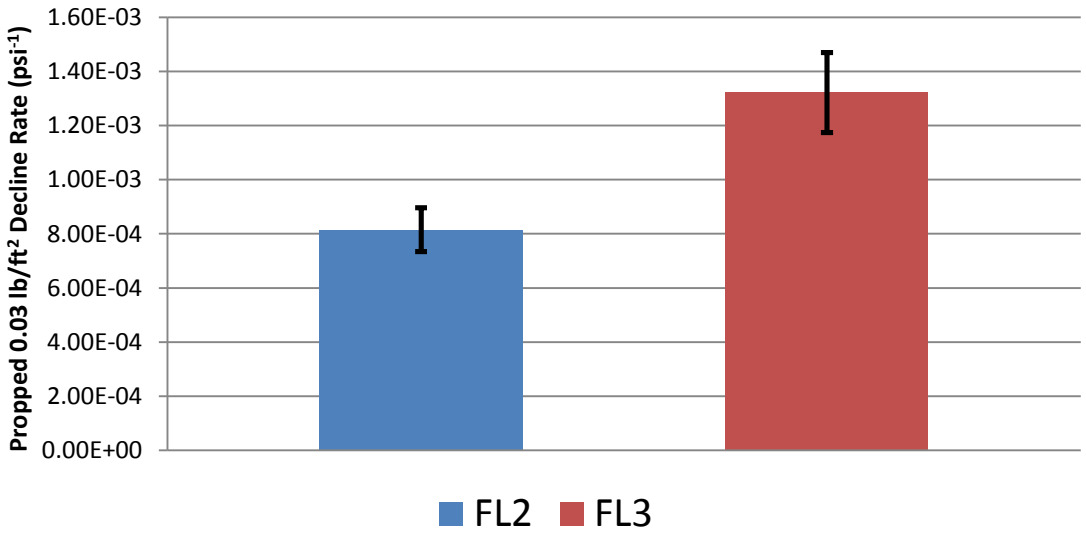

Figure 35 - Decline rate distributions for 0.03 lb/ft^2 - 30/70 mesh propped FL2 and FL3 fractures

In both graphs, there is a significant difference in the decline rates. At 500 psi, the average conductivity of FL2 and FL3 are almost identical, when in the unpropped case, there was a two order-of-magnitude difference between them. In both cases, the addition of a single layer of proppant significantly increased the conductivity from the baseline unpropped case. Because the FL3 is so flat, adding a single layer of proppant creates a level path for the gas flowing through the fracture around the sand grains. In the FL2, the greater roughness increases the tortuosity of the flow path through the fracture. This results in a very similar conductivity at the lowest closure stress.

As the closure stress increases, the proppant begins to embed at different rates in the FL2 and FL3 zones. The relationship between proppant embedment depth and Young's Modulus is known to be a power law relationship (Alramahi and Sundberg, 2012). The relationship for 20/40 mesh high-strength bauxite proppant embedment depth at 5,000 psi and Young's Modulus is as follows:

$$\text{Embedment (mm)} = f(E) = 0.3685E^{-0.549} \quad \text{(3-2)}$$

where E is Young's Modulus in 10^6 psi. This correlation is for a monolayer of a different proppant size and type at a higher closure stress. However, if it is assumed that the correlation scales with proppant sizes and types, then the correlation can be used to estimate the relative embedment as a function of Young's Modulus. If Equation (3-2) is used with the average Young's Moduli of FL2 and FL3, the relationship between the conductivity decline rates can be explained.

$$\frac{\lambda_{FL2}}{\lambda_{FL3}} = \frac{8.23\times10^{-4}}{1.32\times10^{-3}} = 0.623 \approx 0.612 = \frac{0.335}{0.547} = \frac{f(E_{\mathrm{FL2}})}{f(E_{\mathrm{FL3}})} \quad \text{(3-3)}$$

Equation (3-3) shows that the FL2 to FL3 decline rate ratio is very close to the associated proppant embedment ratio. This comparison shows that a higher Young's Modulus prevents proppant embedment, which in turn results in losing less fracture conductivity as closure stress increases. The higher Young's Modulus is also associated with a higher yield stress. This higher yield stress delays the onset of embedment (permanent deformation). This is a dominating effect at monolayer proppant concentrations.

As proppant concentrations increase to a multilayer proppant pack, the differences between rocks properties has little-to-no significant effect on conductivity behavior. The gas flow is able to pass through the proppant pack and bypass many of the fracture surface effects. The final cross-zone conductivity comparison is between FL2 and FL3 with 0.1 lb/ft^2 areal concentration of 30/70 sand. At this concentration, there are approximately 3 layers of proppant, which is a small, multilayer proppant pack. Figure 36 shows the average propped conductivity values for FL2 and FL3. Figure 37 compares the distribution of decline rates of the individual conductivity experiments. The error bars are +/- one standard deviation.

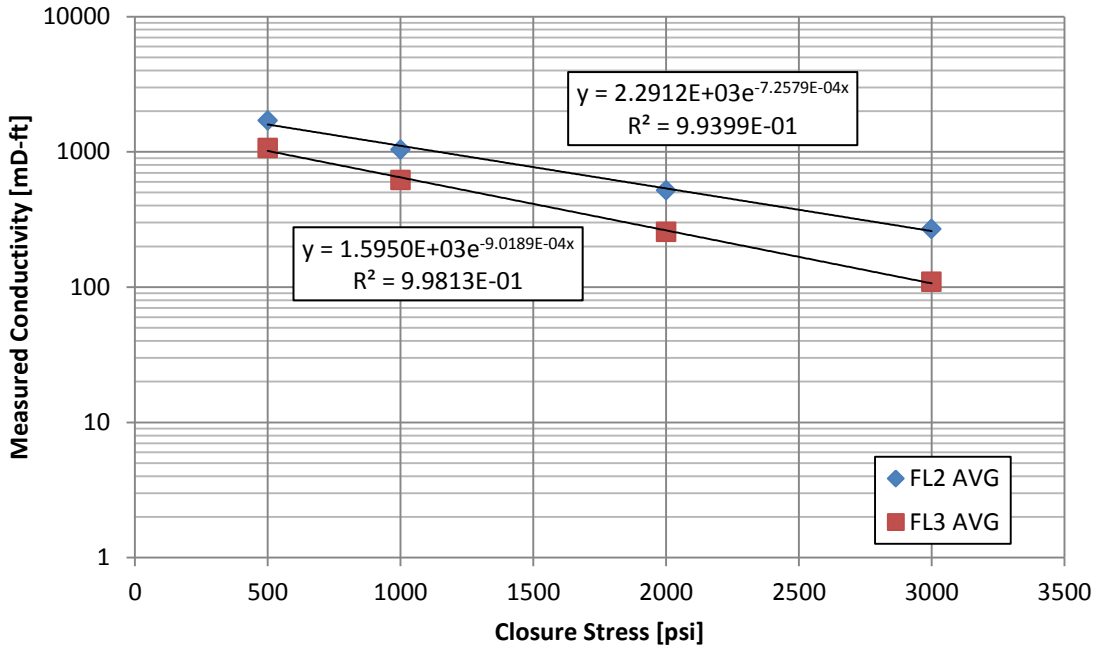

Figure 36 - 0.1 lb/ft^2 - 30/70 mesh average conductivites with exponential fits for FL2 and FL3

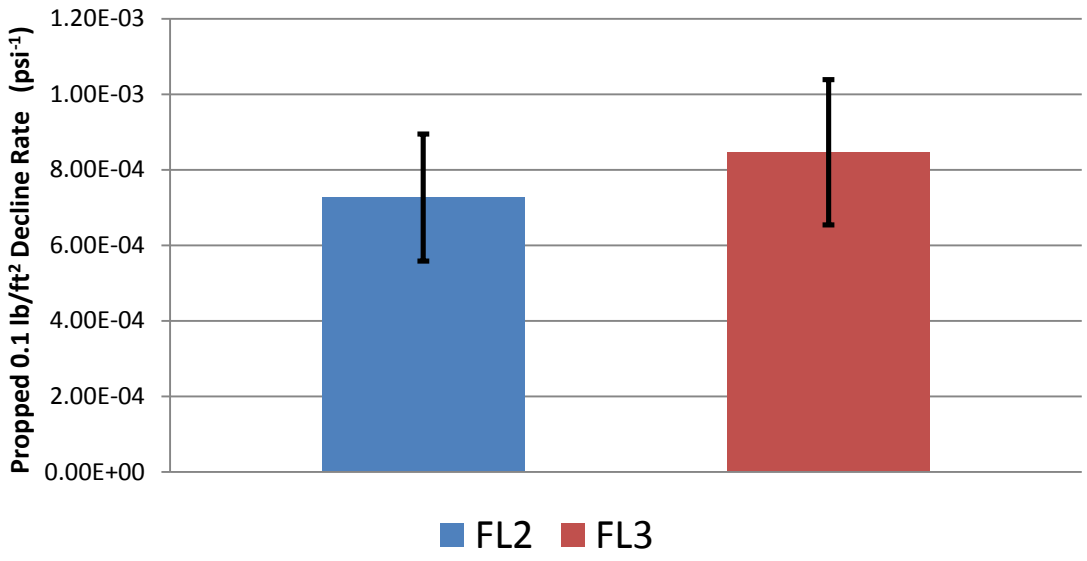

Figure 37 - Decline rate distributions for 0.1 lb/ft^2 - 30/70 mesh propped FL2 and FL3 fractures

The average conductivity exponential fits suggest that the decline rate of FL2 is slightly smaller than that of FL3. As the proppant concentrations increase, the rock properties matter less. The distributions of the individual decline rates for FL2 and FL3 highly overlap, and there is not a statistically significant difference.

The main lesson that can be taken from the cross-shale comparison of propped fracture conductivity is that a higher Young's Modulus reduces proppant embedment, which helps maintain fracture width and thus, fracture conductivity with increasing closure stress. As proppant concentrations increase, the effect of rock properties such as Young's Modulus becomes less important because the conductivity is dominated by proppant effects.

3.4.3 Effect of Rock Properties on Fracture Conductivity in the Eagle Ford

The lessons learned in the cross-shale analysis were then applied to a smaller scale within the seven locations in the Eagle Ford shale. The decline rates of the conductivity measurements were the main focus of this part of the study. There are several interfering factors that could influence the decline rate comparisons:

- Poisson's Ratio is not constant across the seven locations. Variations may have an effect on the conductivity decline rate.
- The variation between Young's Modulus may not be significant to overcome variation in sample geometry. In the cross-shale scale, the changes in geometry were accompanied by a much larger change in Young's Modulus.

- The standard deviation of the Young's Modulus measurements at certain locations is relatively large compared to the range of the average values. This effect was not a factor when comparing across shales.
- The propped conductivity experiments for the Eagle Ford have closure stresses up to 6000 psi. At these higher stresses, exponential declines may not apply.

The combination of these factors makes the statistical significance of any findings within the Eagle Ford zone questionable. Figures 38, 39, and 40 show the relationships between Young's Modulus and the conductivity decline rate for unpropped, 0.1 lb/ft^2, and 0.2 lb/ft^2 proppant concentrations of 30/50 white sand respectively. The error bars are the Young's Modulus measurements' standard deviations at the respective location. All of the figures are scaled identically for easy comparison.

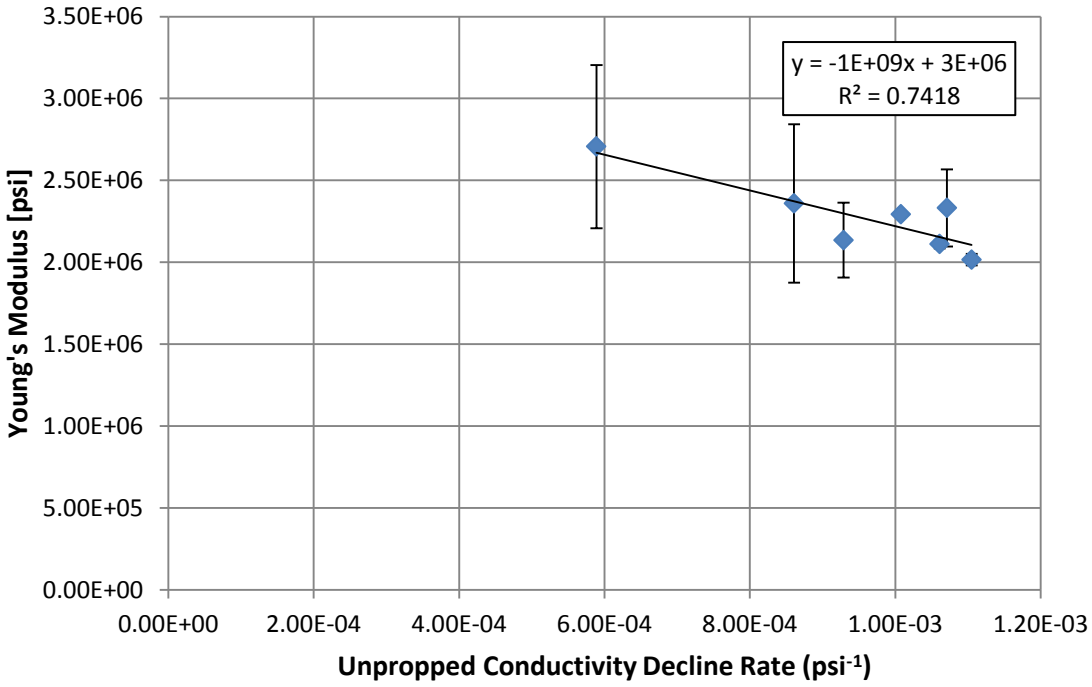

Figure 38 - Eagle Ford unpropped conductivity decline rate vs. Young's Modulus

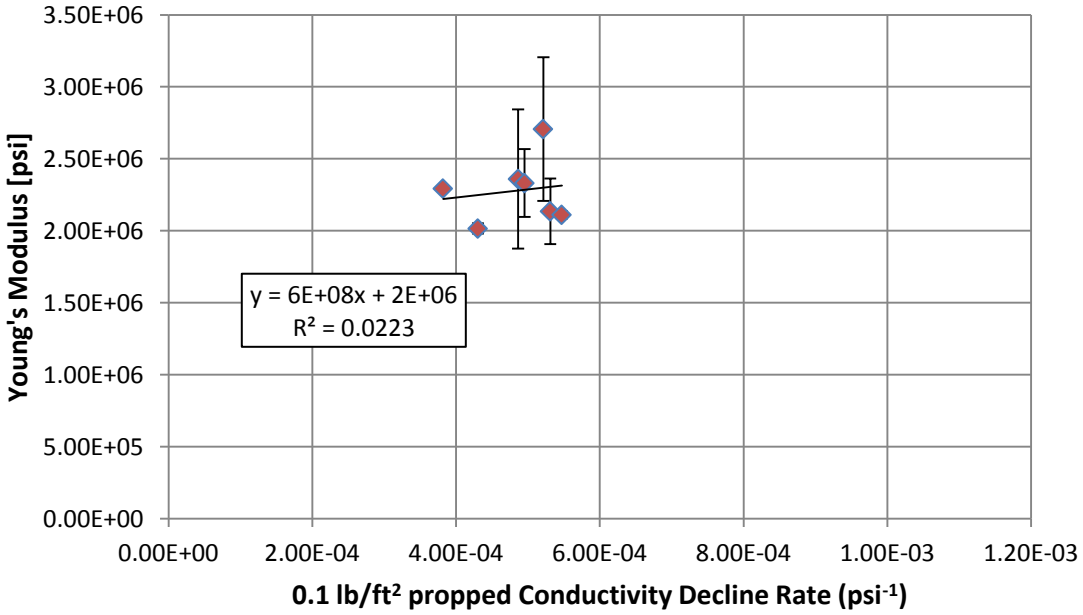

Figure 39 - Eagle Ford 0.1 lb/ft^2 30/50 mesh propped conductivity decline rate vs. Young's Modulus

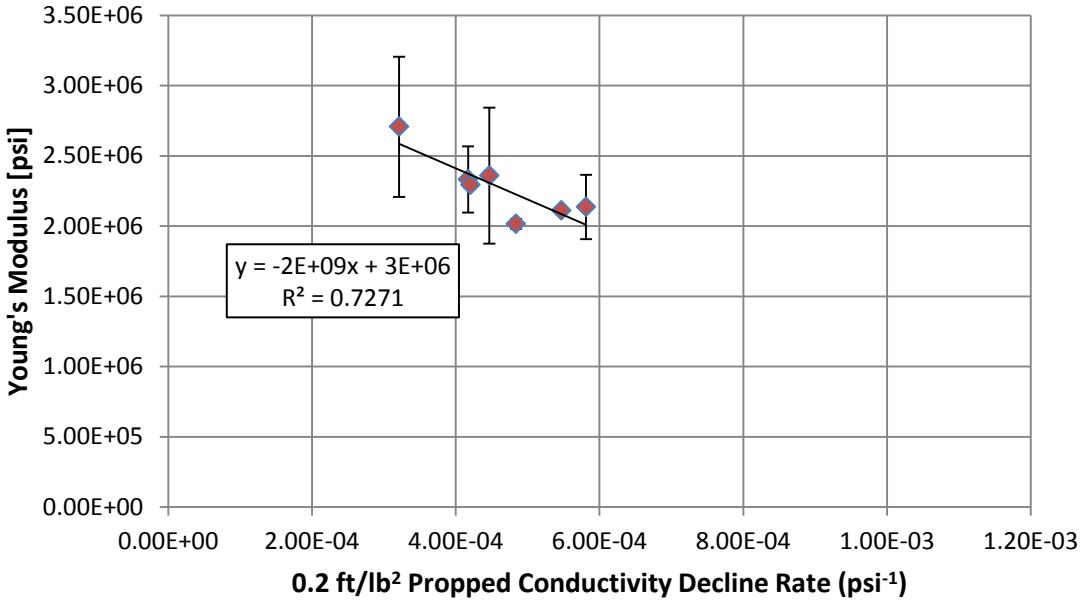

Figure 40 - Eagle Ford 0.2 lb/ft^2 30/50 mesh propped conductivity decline rate vs. Young's Modulus

The unpropped conductivity decline rates decrease as Young's Modulus increases. This is the same trend that was evident in the FL2 and FL3 comparison. This trend does appear to be heavily influenced by the outlier point, however. On the other hand, the 0.1 lb/ft^2 conductivity decline rates do not correlate with Young's Modulus (R^2=0.02). This is expected because a proppant concentration of 0.1 lb/ft^2 is a multilayer proppant pack (~2.5 layers) for this proppant mesh size. At this concentration, the conductivity behavior should be dominated by proppant characteristics and not rock properties. It is odd that there appears to be a correlation (R^2=0.72) with a proppant concentration of 0.2 lb/ft^2. This concentration is an even larger proppant pack (~5

layers). This is likely a false correlation. Overall, these Eagle Ford results are statistically insignificant due to the previously mentioned interfering factors.

These interfering factors make it difficult to accurately quantify the effect of Young's Modulus and other rock characteristics on the decline rates of fracture conductivity in a particular zone. Even with all the statistical ambiguity in the Eagle Ford zone analysis, it still makes sense to presume that a higher Young's Modulus decreases the conductivity decline rate if fracture surface geometry, Poisson's Ratio, etc. are all the same. When the differences in Young's Modulus are relatively small compared to the differences in the cross-shale analysis, it is very hard to measure the effect with only seven conductivity tests.

4. CONCLUSIONS AND RECOMMENDATIONS

4.1 Conclusions

This study presented the findings on the relationship between the laboratory fracture conductivity and the rock characteristics of Eagle Ford, Fayetteville FL2 and Fayetteville FL3 outcrop samples. Triaxial tests were performed in order to measure the Young's Modulus and Poisson's Ratio of the samples. XRD and FTIR tests were performed to determine the mineralogical composition of the outcrop samples. Surface profilometer scans were performed in order to characterize the fracture surface topography. These characteristics were combined with previously-performed fracture conductivity measurements in order to make the following conclusions and observations:

1. Conductivity behavior is controlled by a varying combination of rock and proppant properties.
2. In all fractures, the main factors controlling fracture conductivity are closure stress and proppant concentration, size and strength.
3. In unpropped fractures, the magnitude of the conductivity is dominated by fracture surface topography effects. A rougher surface allows for a larger initial flow path for fluids. A greater Young's Modulus (and the associated higher yield stress) reduces the conductivity lost from this initial value as closure stress increases. Surface geometry can play an important role in determining how conductivity is affected by closure stress by reducing the actual contact area between the two fracture faces.

4. At higher proppant concentrations that involve multilayer proppant packs, the effect of the rock properties on conductivity is negligible compared to the properties of the proppant.
5. In proppant monolayer concentrations, proppant embedment is a major factor in conductivity loss. A greater Young's Modulus can dramatically reduce the conductivity loss due to proppant embedment, particularly in rocks with Young's Moduli less than 2 Mpsi.
6. Combining all of the above: Brittle shale intervals with a high Young's Modulus and a low Poisson's ratio is ideal to create large, complex propped fracture networks. This guideline not only improves proppant placement, but also likely improves fracture conductivity for a given proppant concentration due to the higher Young's Modulus.

4.2 Recommendations

From this point going forward, there are numerous directions that this study can continue:

1. Most of these conclusions are based on observations of two or three shale zones. This work should be expanded to other shales to see if the relationships found in this study hold true in other formations.
2. Conductivity measurements that include the interaction of rock with various fracture fluids should be performed in order to better understand the effect of mineral composition on fracture conductivity.

3. Future conductivity experiments should include surface scans whenever feasible in order to better account for the effect of surface geometry.
4. Current conductivity experiments focus on using proppant sizes and concentrations that directly to those used in the field. This should continue, with the addition of some standardized proppant size and concentration tests across all shales. This will allow for more cross-shale comparisons.

REFERENCES

Alramahi, B., Sundberg, M.I. (2012). Proppant Embedment and Conductivity or Hydraulic Fractures in Shales. US Rock Mechanics / Geomechanics Symposium. Chicago, Illinois. 2012. Copyright 2012 ARMA, American Rock Mechanics Association.

ASTM Standard D4543-08. (2008). Standard Practices for Preparing Rock Core as Cylindrical Test Specimens and Verifying Conformance to Dimensional and Shape Tolerances. ASTM International. West Conshohocken, PA, 2008. DOI: 10.1520/D4543-08. www.astm.org

ASTM Standard D7012-14. (2014). Standard Test Methods for Compressive Strength and Elastic Moduli of Intact Rock Core Specimens under Varying States of Stress and Temperatures. ASTM International. West Conshohocken, PA, 2014. DOI: 10.1520/ D7012-14. www.astm.org

Bandis, S.C., Lumsden, A.C., Barton, N.R. (1983). "Fundamentals of rock joint deformation." International Journal of Rock Mechanics and Mining Sciences & Geomechanics Abstracts 20(6): 249-268.

Barton, N. R., Bandis, S. C., Bakhtar, K. (1985). "Strength, deformation and conductivity coupling of rock joints." International Journal of Rock Mechanics and Mining Sciences & Geomechanics Abstracts 22(3): 121-140.

Briggs, K. (2014). The Influence of Vertical Location on Hydraulic Fracture Conductivity in the Fayetteville Shale. Master's Thesis: Texas A&M University Petroleum Engineering. College Station, TX. Copyright 2014, Kathryn Elizabeth Briggs.

Centurion, S. (2011) Eagle Ford Shale: A Multi-Stage Hydraulic Fracturing, Completion Trends And Production Outcome Study Using Practical Data Mining Techniques. SPE Eastern Regional Meeting, Colombus, Ohio, 2011. Copyright 2011, Society of Petroleum Engineers.

Cooke Jr., C. E. (1973). "Conductivity of fracture proppants in multiple layers." Journal of Petroleum Technology 25(9): 1101-1107.

D'Andrea, D. V., Fischer, R. L., Fogelson, D. E. (1965). Prediction of Compressive Strength from Other Rock Properties. United States Department of the Interior, Bureau of Mines. Report of investigations 6702, Washington D.C.

Donovan, A. D., and T. S. Staerker. (2010). Sequence stratigraphy of the Eagle Ford (Boquillas) Formation in the subsurface of South Texas and outcrops of West Texas. Gulf Coast Association of Geological Societies Transactions, v. 60, p. 861-899.

Fredd, C. N., McConnell, S. B., Boney, C. L., England, K. W. (2001). "Experimental study of fracture conductivity for water-fracturing and conventional fracturing applications." SPE Journal 6(3): 288-298.

Gardner, R., Pope, M. C., Wehner, M. P., Donovan, A. D. (2013). "Comparative stratigraphy of the Eagle Ford group strata in Lozier Canyon and Antonio Creek, Terrell County, Texas." GCAGS Journal 2(1): 42-52.

Guzek, J. (2014). Fracture Conductivity of the Eagle Ford Shale. Master's Thesis. Texas A&M University Petroleum Engineering. College Station, TX. Copyright 2014, James J. Guzek.

Ketter, A. A., Heinze, J. R., Daniels, J. L., Waters, G. (2008, August). "A field study in optimizing completion strategies for fracture initiation in Barnett Shale horizontal wells." *SPE Production & Operations, 23*(3), 373-378.

Makurat, A., Gutierrez, M. (1996). Fracture Flow and Fracture Cross Flow Experiments. SPE Annual Technical Conference and Exhibition. Denver, Colorado, 1996 Copyright 1996, Society of Petroleum Engineers, Inc.

Matthews, H. L., Schein, G. W., Malone, M. (2007). Stimulation of Gas Shales: They're All the Same Right? SPE Hydraulic Fracturing Technology Conference. College Station, TX, 2007. Copyright 2007, Society of Petroleum Engineers.

Mullen, J. (2010). Petrophysical Characterization of the Eagle Ford Shale in South Texas. Canadian Unconventional Resources and International Petroleum Conference. Calgary, Alberta, 2010. Copyright 2010, Society of Petroleum Engineers.

Olsson, W. A., Brown, S. R. (1993). "Hydromechanical response of a fracture undergoing compression and shear." International Journal of Rock Mechanics and Mining Sciences & Geomechanics Abstracts 30(7): 845-851.

Paterson, M. S. and Wong, T. (2005). Experimental Rock Deformation – The Brittle Field, Second Edition. Springer-Verlag Berlin Heidelberg, The Netherlands, 2005. ISBN: 3-540-24023-3.

Penny, G. S. (1987). An Evaluation of the Effects of Environmental Conditions and Fracturing Fluids Upon the Long-Term Conductivity of Proppants. SPE Annual Technical Conference and Exhibition. Dallas, Texas, 1987 Copyright 1987, Society of Petroleum Engineers.

Qinghui Li, Mian Chen, Yan Jin, Yu Zhou, Wang, Fred P., Rixing Zhang. (2013). Rock Mechanical Properties of Shale Gas Reservoir and Their Influences on Hydraulic Fracture. International Petroleum Technology Conference, Beijing, China, 2013. Copyright 2013, International Petroleum Technology Conference.

Quirein, J., Praxnik, G., Galford, J., Chen, S., Murphy, E., Witkowsky, J., (2013). A Workflow to Evaluate Mineralogy, Porosity, TOC, and Hydrocarbon Volume in the Eagle Ford Shale. SPE Unconventional Resources Conference and Exhibition – Asia Pacific, Brisband, Austrailia, 2013. Copyright 2013, Society of Petroleum Engineers.

Rickman, R., Mullen, M., Petre, E. Grieser, B., Kundert, D. (2008). A Practical Use of Shale Petrophysics for Stimulation Design Optimization: All Shale Plays Are Not Clones of the Barnett Shale. SPE Annual Technical Conference and Exhibition, Denver, Colorado, 2008. Copyright 2008, Society of Petroleum Engineers.

Rivers, M., Zhu, D., Hill, A. D., (2012). Proppant Fracture Conductivity With High Proppant Loading and High Closure Stress. SPE Hydraulic Fracturing Technology Conference. The Woodlands, Texas, USA, 2012. Copyright 2012, Society of Petroleum Engineers.

Shelley, R., Saugier, L., Al-Tailji, W., Guliyev, N., (2012). Understanding Hydraulic Fracture Stimulated Horizontal Eagle Ford Completions. SPE/EAGE European Unconventional Resources Conference and Exhibition, Vienna, Austria, 2012. Copyright 2012, Society of Petroleum Engineers.

Zhang, Jujing, Kamenov, A., Zhu, D., Hill, A.D. (2013). Laboratory Measurement of Hydraulic Fracture Conductivityies in the Barnett Shale. SPE Hydraulic Fracturing Technology Conference, The Woodlands, Texas, 2013. Copyright 2013, Society of Petroleum Engineers.

APPENDIX A

COMPLETE EAGLE FORD MECHANICAL RESULTS

EF1 Results

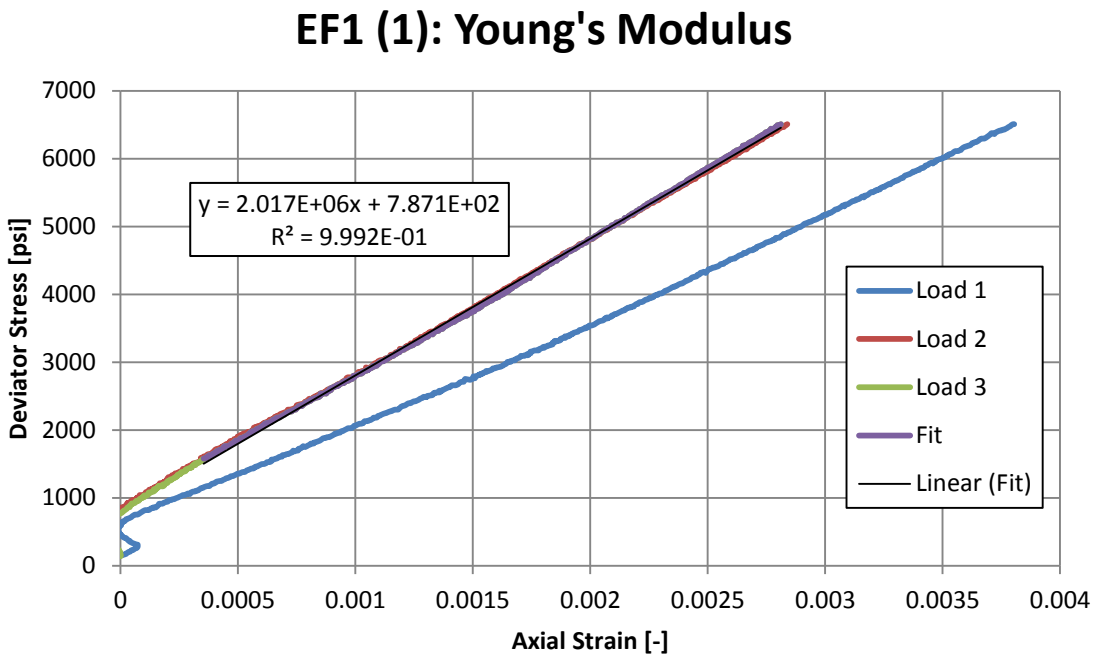
EF1 (1): Young's Modulus
y = 2.017E+06x + 7.871E+02
R² = 9.992E-01
Deviator Stress [psi]
Axial Strain [-]
Load 1
Load 2
Load 3
Fit
Linear (Fit)

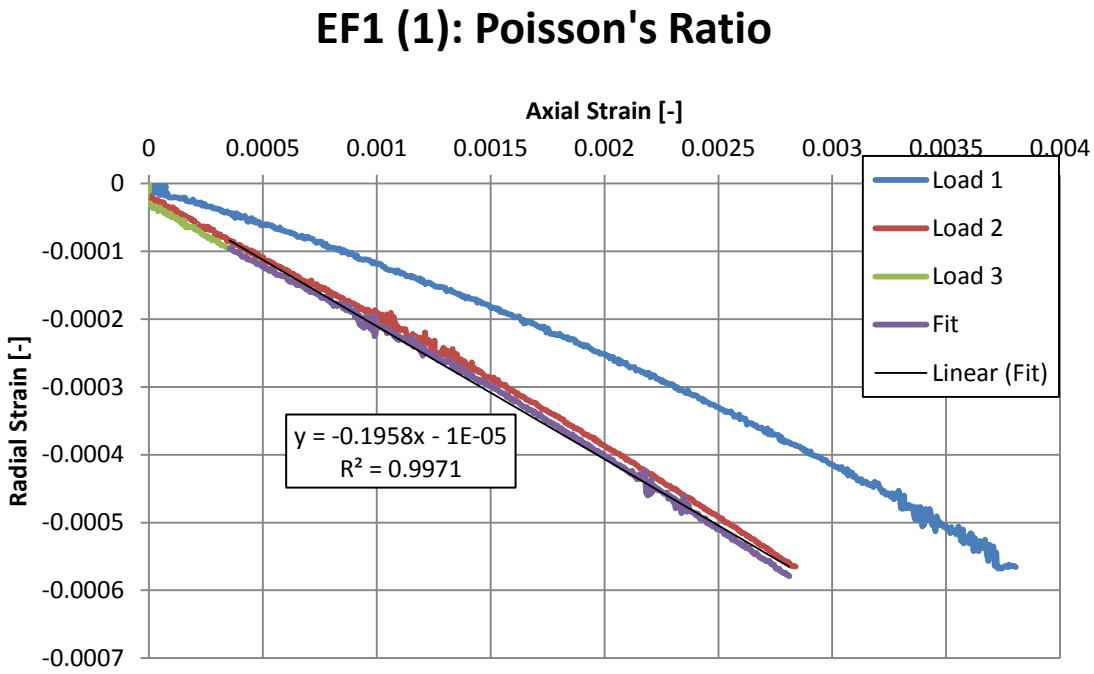
EF1 (1): Poisson's Ratio
y = -0.1958x - 1E-05
R² = 0.9971
Radial Strain [-]
Axial Strain [-]
Load 1
Load 2
Load 3
Fit
Linear (Fit)

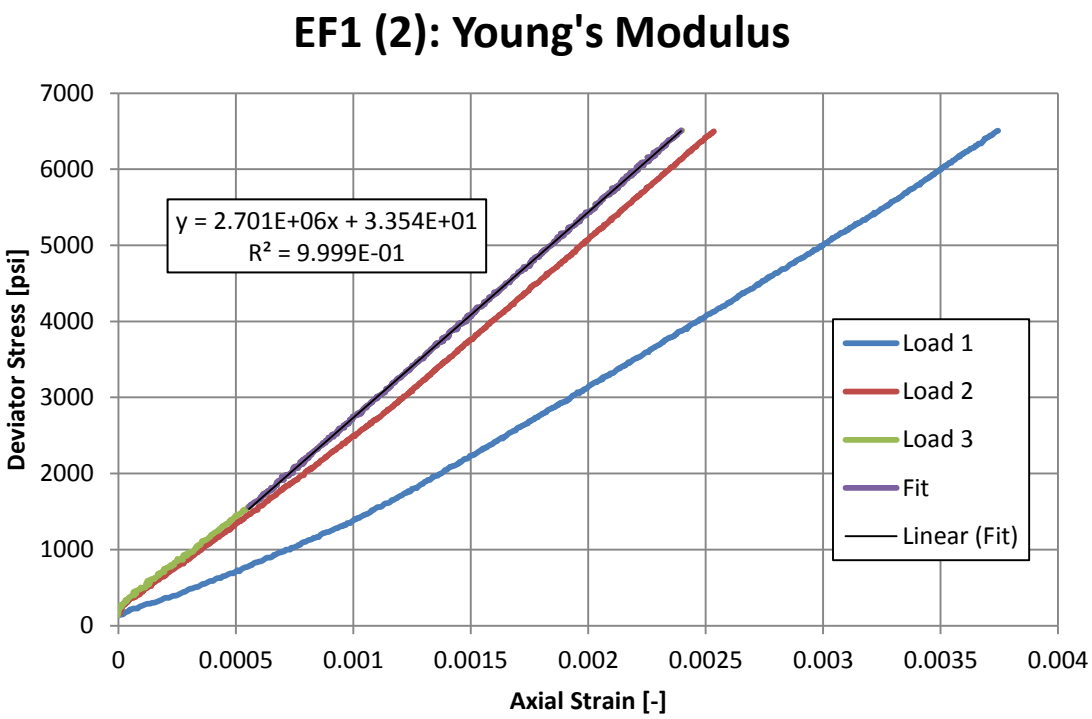
EF1 (2): Young's Modulus
y = 2.701E+06x + 3.354E+01
R² = 9.999E-01
Deviator Stress [psi]
Axial Strain [-]
7000
6000
5000
4000
3000
2000
1000
0
0
0.0005
0.001
0.0015
0.002
0.0025
0.003
0.0035
0.004
Load 1
Load 2
Load 3
Fit
Linear (Fit)

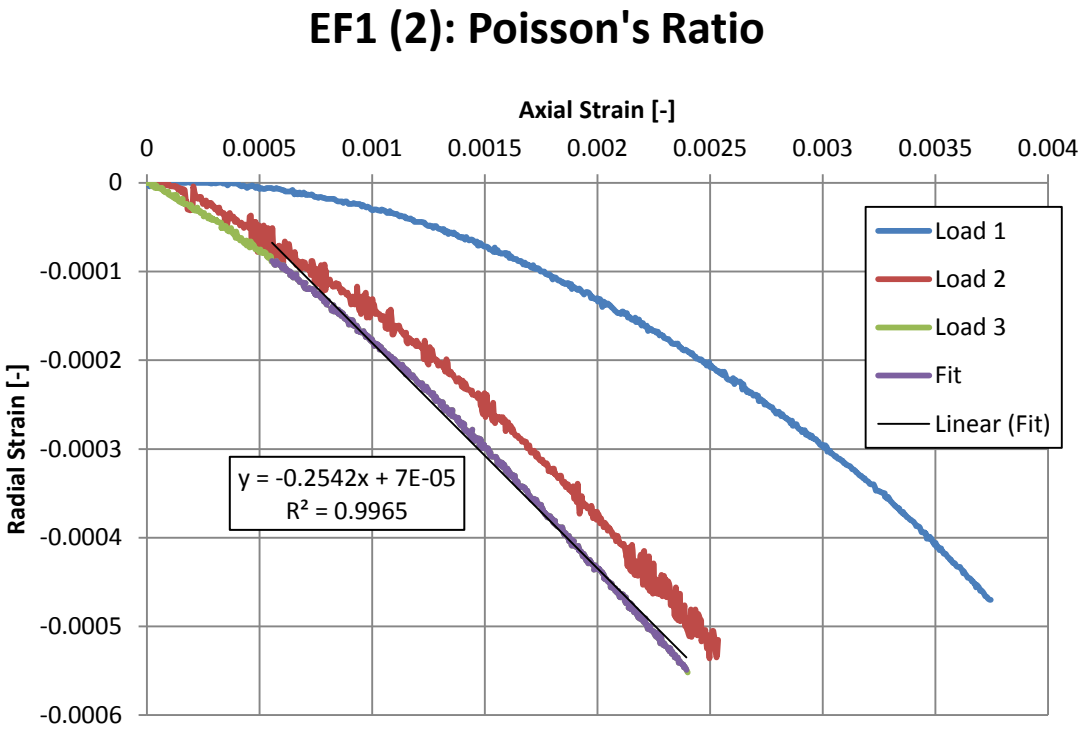
EF1 (2): Poisson's Ratio
Axial Strain [-]
Radial Strain [-]
0
0.0005
0.001
0.0015
0.002
0.0025
0.003
0.0035
0.004
0
-0.0001
-0.0002
-0.0003
-0.0004
-0.0005
-0.0006
y = -0.2542x + 7E-05
R² = 0.9965
Load 1
Load 2
Load 3
Fit
Linear (Fit)

EF2 Results

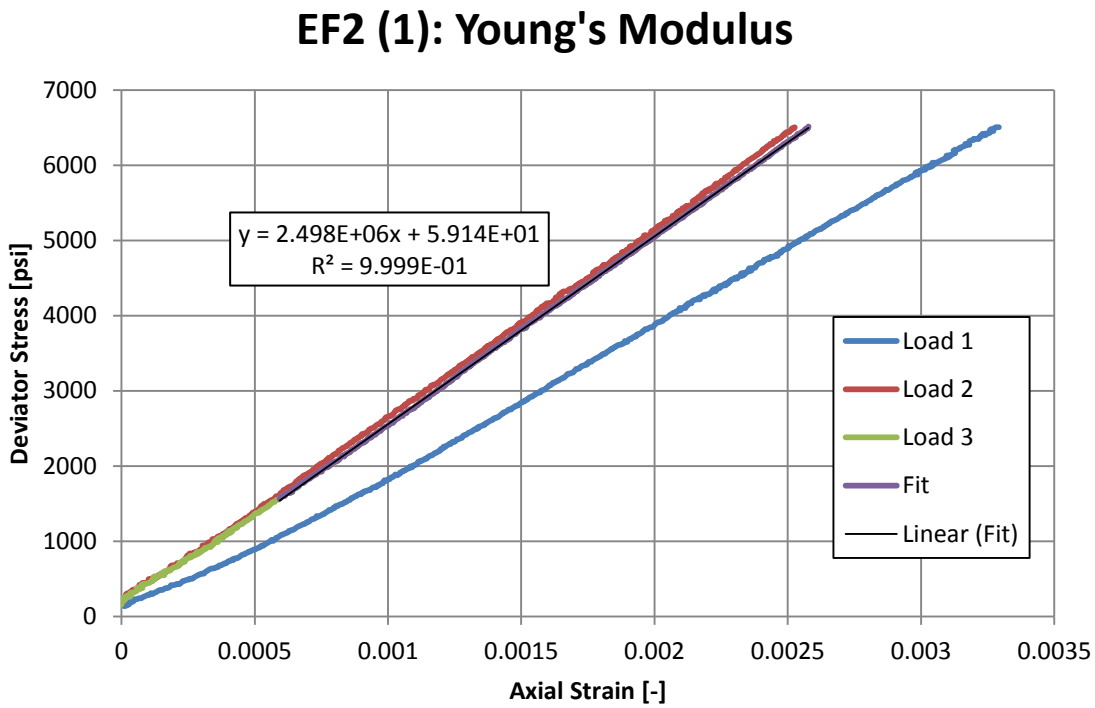
EF2 (1): Young's Modulus
y = 2.498E+06x + 5.914E+01
R² = 9.999E-01
Deviator Stress [psi]
Axial Strain [-]
Load 1
Load 2
Load 3
Fit
Linear (Fit)

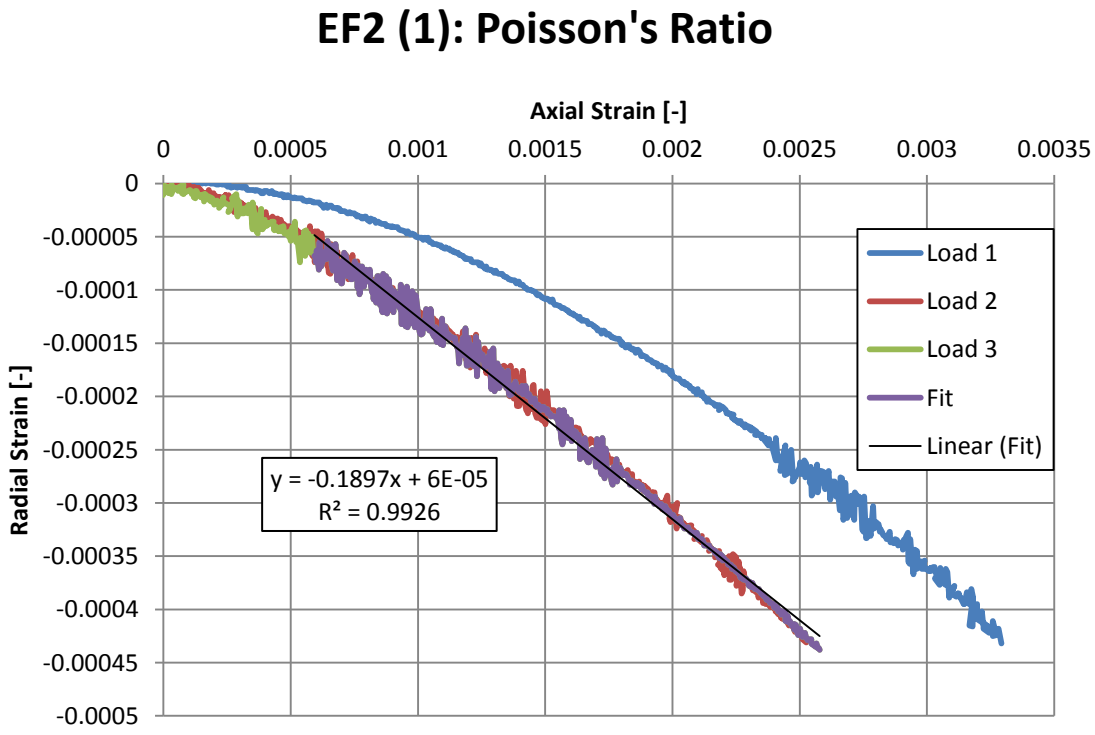
EF2 (1): Poisson's Ratio
y = -0.1897x + 6E-05
R² = 0.9926
Radial Strain [-]
Axial Strain [-]
Load 1
Load 2
Load 3
Fit
Linear (Fit)

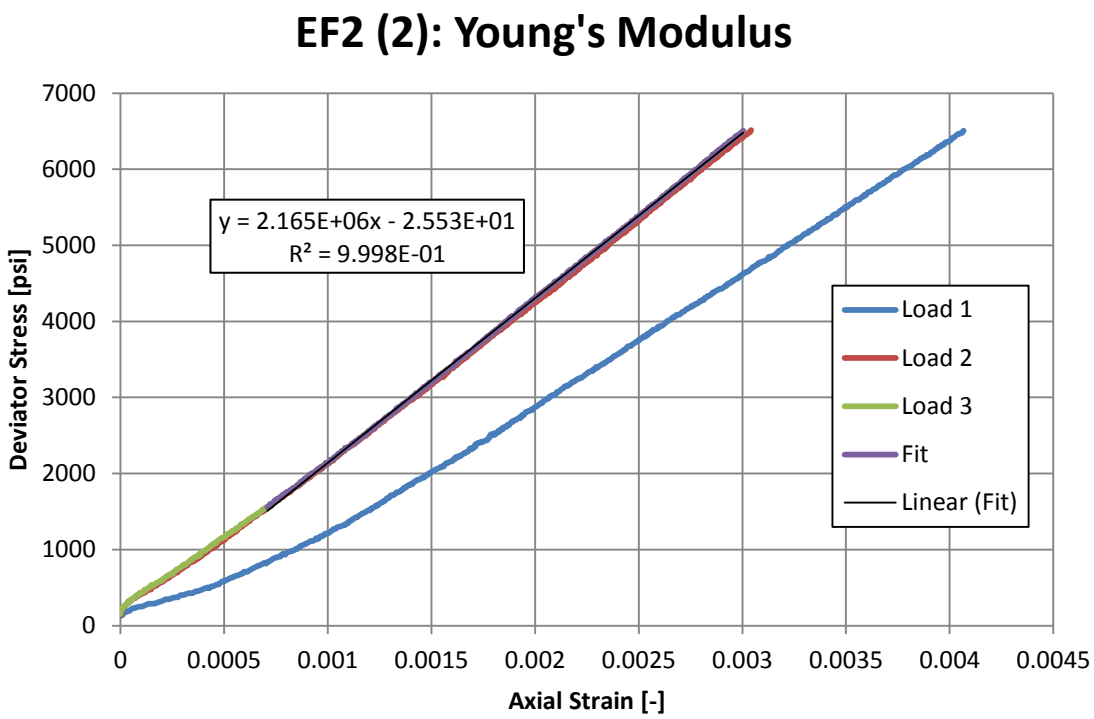
EF2 (2): Young's Modulus
y = 2.165E+06x - 2.553E+01
R² = 9.998E-01
Deviator Stress [psi]
Axial Strain [-]
Load 1
Load 2
Load 3
Fit
Linear (Fit)
7000
6000
5000
4000
3000
2000
1000
0
0
0.0005
0.001
0.0015
0.002
0.0025
0.003
0.0035
0.004
0.0045

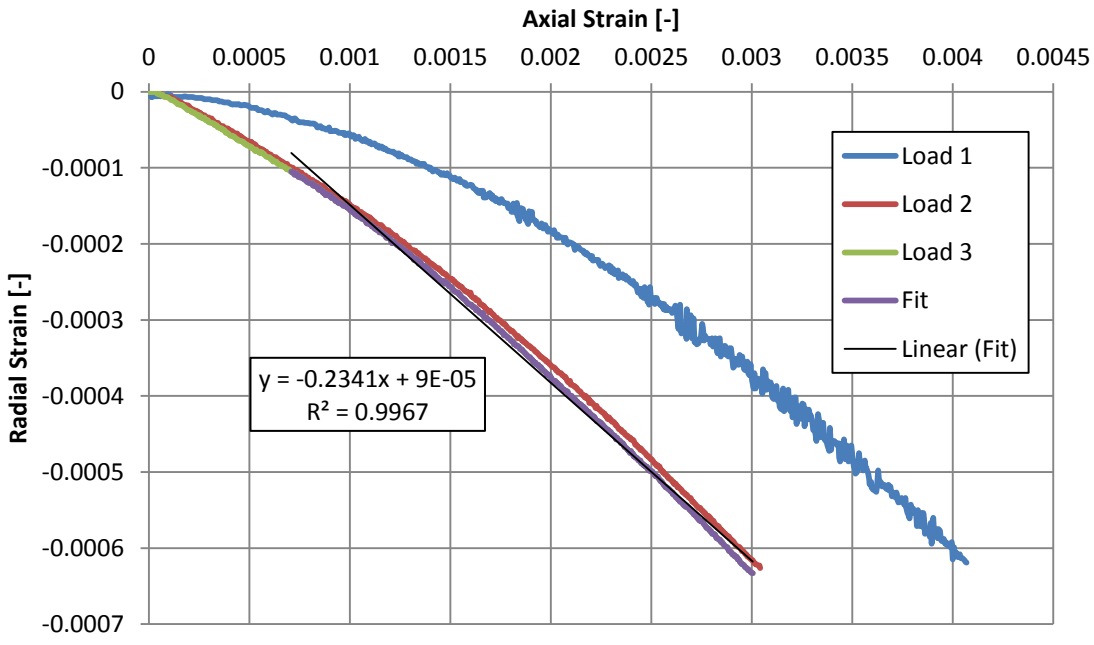
EF2 (2): Poisson's Ratio
Axial Strain [-]
Radial Strain [-]
y = -0.2341x + 9E-05
R² = 0.9967
Load 1
Load 2
Load 3
Fit
Linear (Fit)
0
-0.0001
-0.0002
-0.0003
-0.0004
-0.0005
-0.0006
-0.0007
0
0.0005
0.001
0.0015
0.002
0.0025
0.003
0.0035
0.004
0.0045

EF3 Results

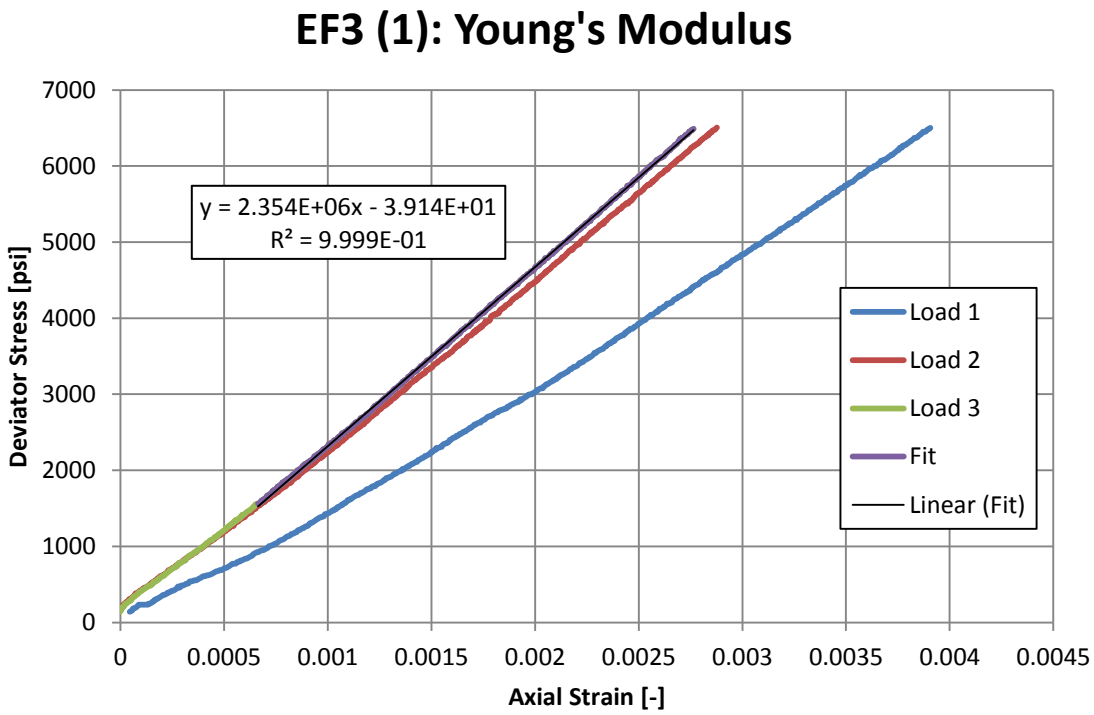
EF3 (1): Young's Modulus
y = 2.354E+06x - 3.914E+01
R² = 9.999E-01
Deviator Stress [psi]
Axial Strain [-]
Load 1
Load 2
Load 3
Fit
Linear (Fit)
0
1000
2000
3000
4000
5000
6000
7000
0.0005
0.001
0.0015
0.002
0.0025
0.003
0.0035
0.004
0.0045

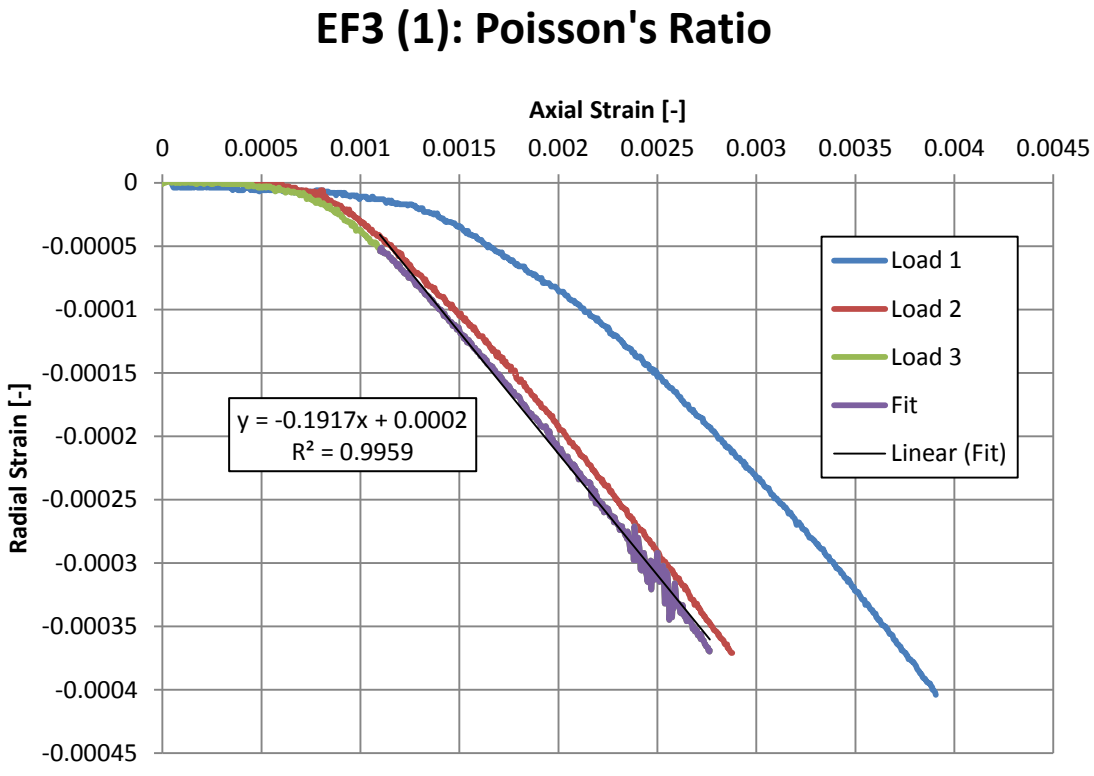
EF3 (1): Poisson's Ratio
Axial Strain [-]
Radial Strain [-]
y = -0.1917x + 0.0002
R² = 0.9959
Load 1
Load 2
Load 3
Fit
Linear (Fit)
0
-0.00005
-0.0001
-0.00015
-0.0002
-0.00025
-0.0003
-0.00035
-0.0004
-0.00045
0.0005
0.001
0.0015
0.002
0.0025
0.003
0.0035
0.004
0.0045

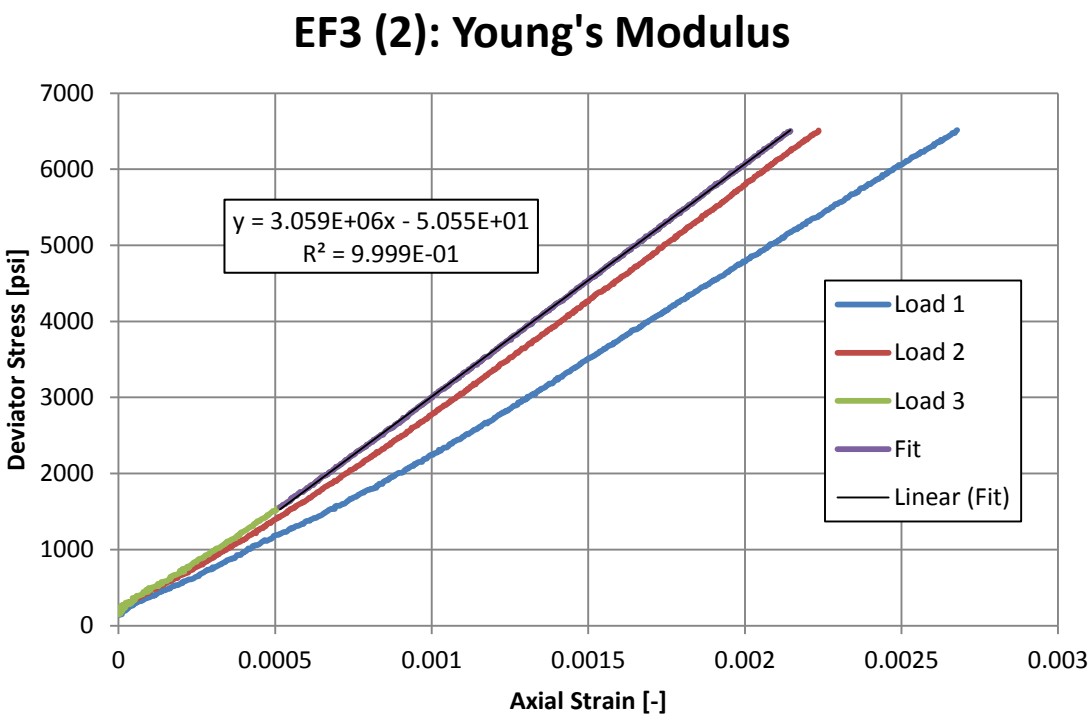
EF3 (2): Young's Modulus
Deviator Stress [psi]
7000
6000
5000
4000
3000
2000
1000
0
0
0.0005
0.001
0.0015
0.002
0.0025
0.003
Axial Strain [-]
y = 3.059E+06x - 5.055E+01
R² = 9.999E-01
Load 1
Load 2
Load 3
Fit
Linear (Fit)

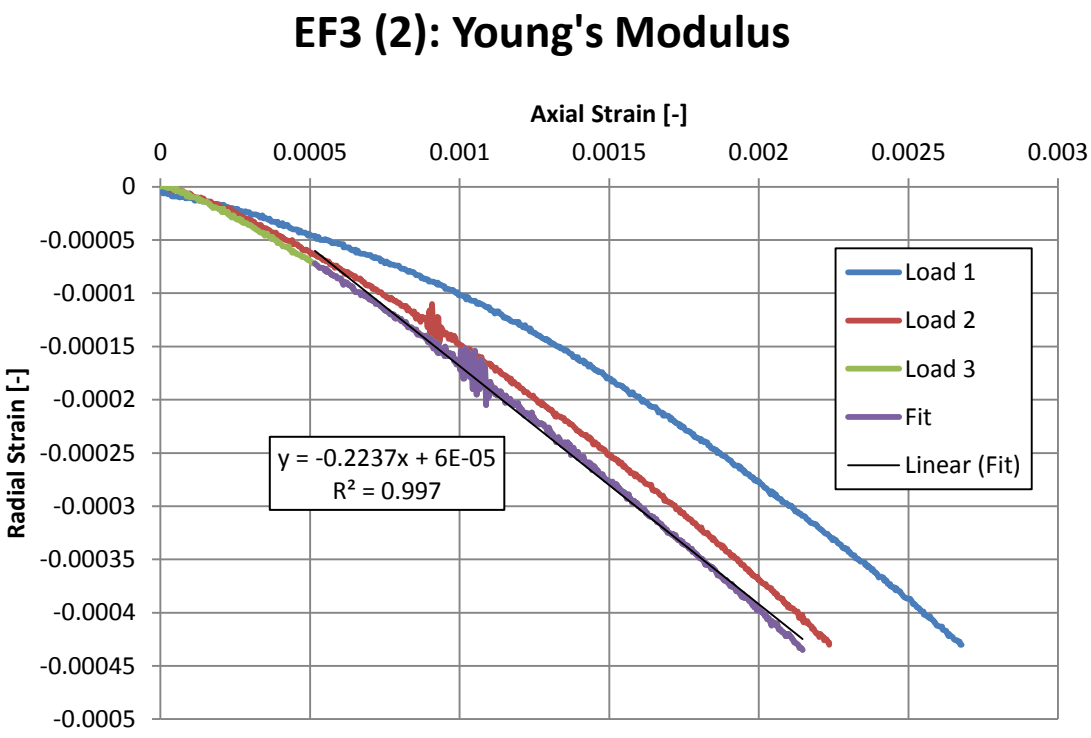
EF3 (2): Young's Modulus
Axial Strain [-]
0
0.0005
0.001
0.0015
0.002
0.0025
0.003
Radial Strain [-]
0
-0.00005
-0.0001
-0.00015
-0.0002
-0.00025
-0.0003
-0.00035
-0.0004
-0.00045
-0.0005
y = -0.2237x + 6E-05
R² = 0.997
Load 1
Load 2
Load 3
Fit
Linear (Fit)

EF4 Results

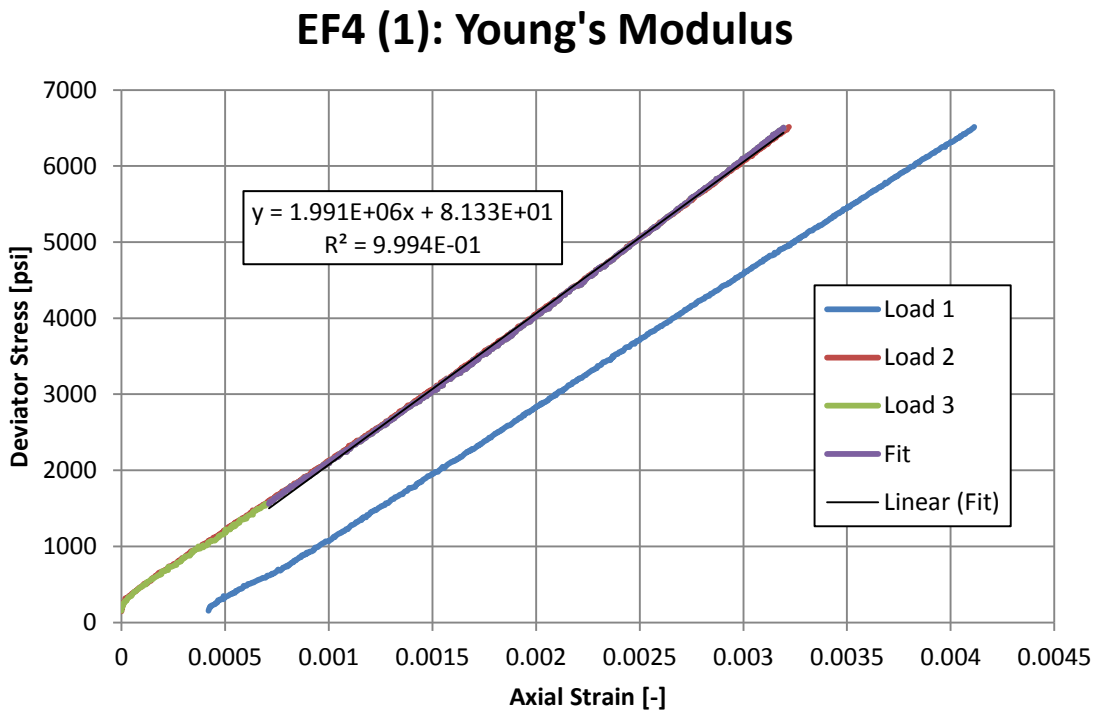
EF4 (1): Young's Modulus
y = 1.991E+06x + 8.133E+01
R² = 9.994E-01
Deviator Stress [psi]
Axial Strain [-]
Load 1
Load 2
Load 3
Fit
Linear (Fit)
0
1000
2000
3000
4000
5000
6000
7000
0.0005
0.001
0.0015
0.002
0.0025
0.003
0.0035
0.004
0.0045

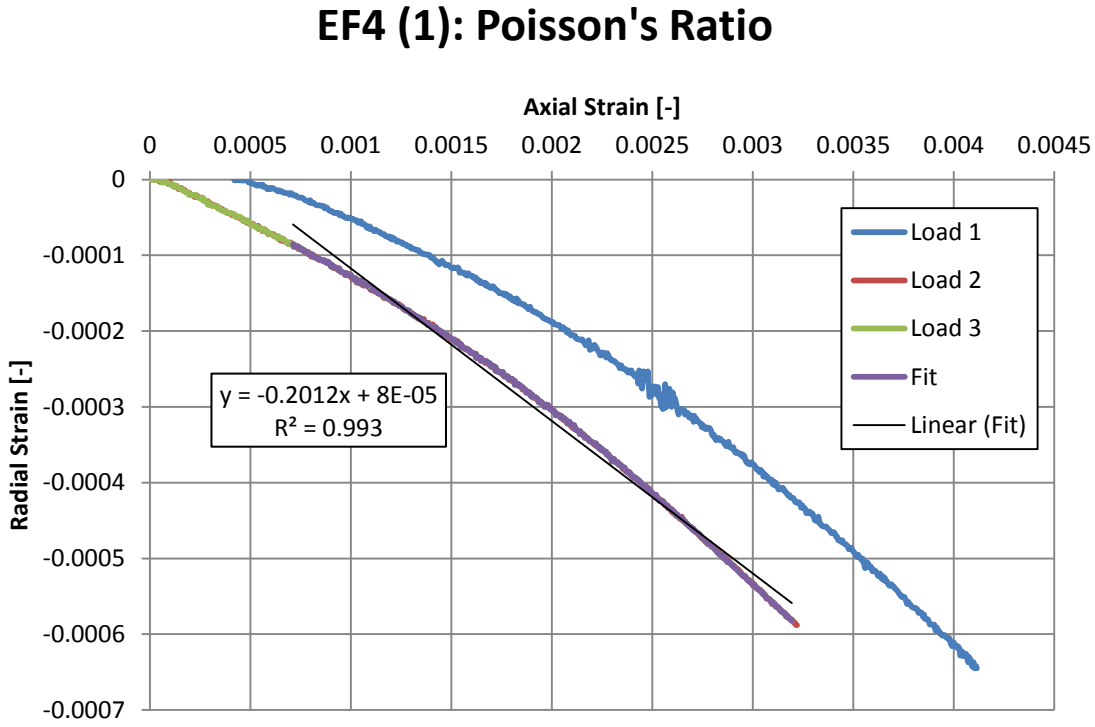
EF4 (1): Poisson's Ratio
Axial Strain [-]
Radial Strain [-]
y = -0.2012x + 8E-05
R² = 0.993
Load 1
Load 2
Load 3
Fit
Linear (Fit)
0
-0.0001
-0.0002
-0.0003
-0.0004
-0.0005
-0.0006
-0.0007
0.0005
0.001
0.0015
0.002
0.0025
0.003
0.0035
0.004
0.0045

EF4 (2): Young's Modulus

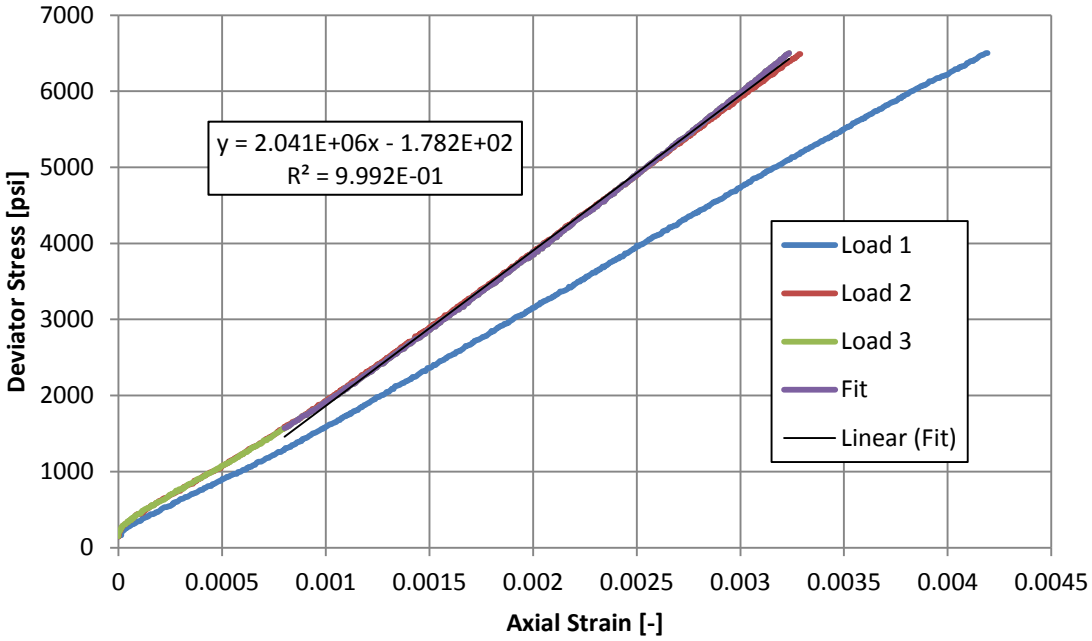

EF4 (2): Poisson's Ratio

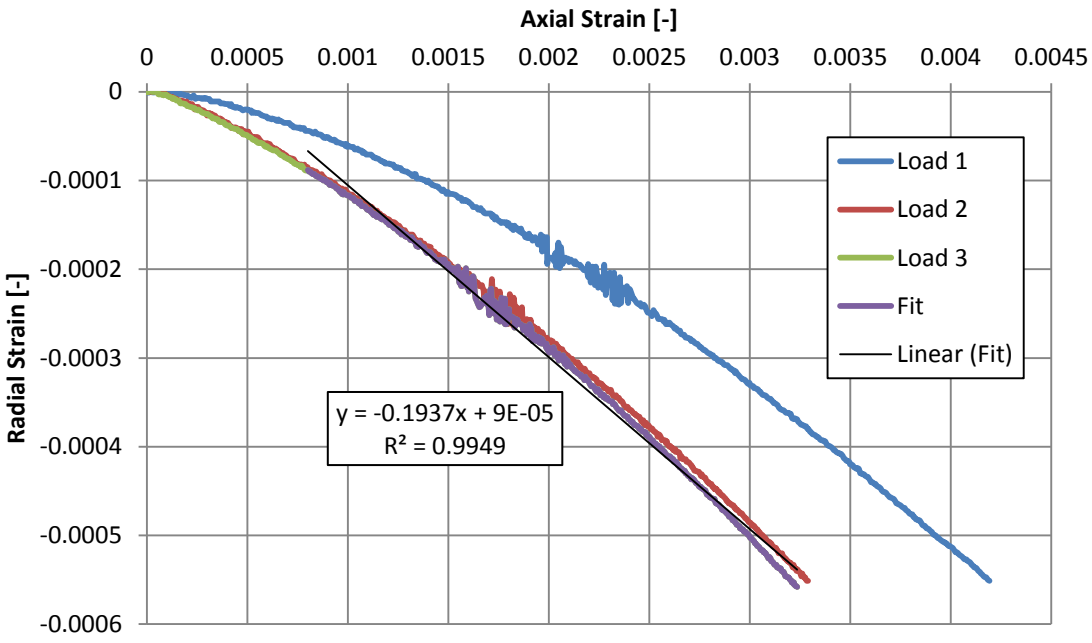

EF5 Results

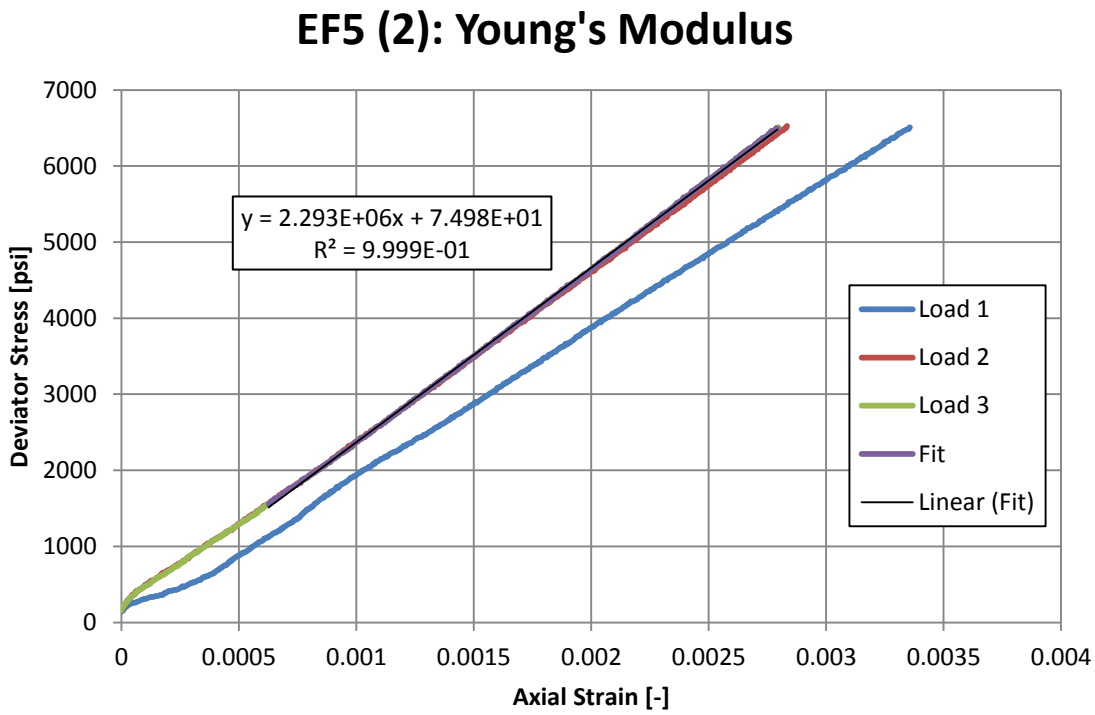
EF5 (2): Young's Modulus
y = 2.293E+06x + 7.498E+01
R² = 9.999E-01
Deviator Stress [psi]
Axial Strain [-]
Load 1
Load 2
Load 3
Fit
Linear (Fit)

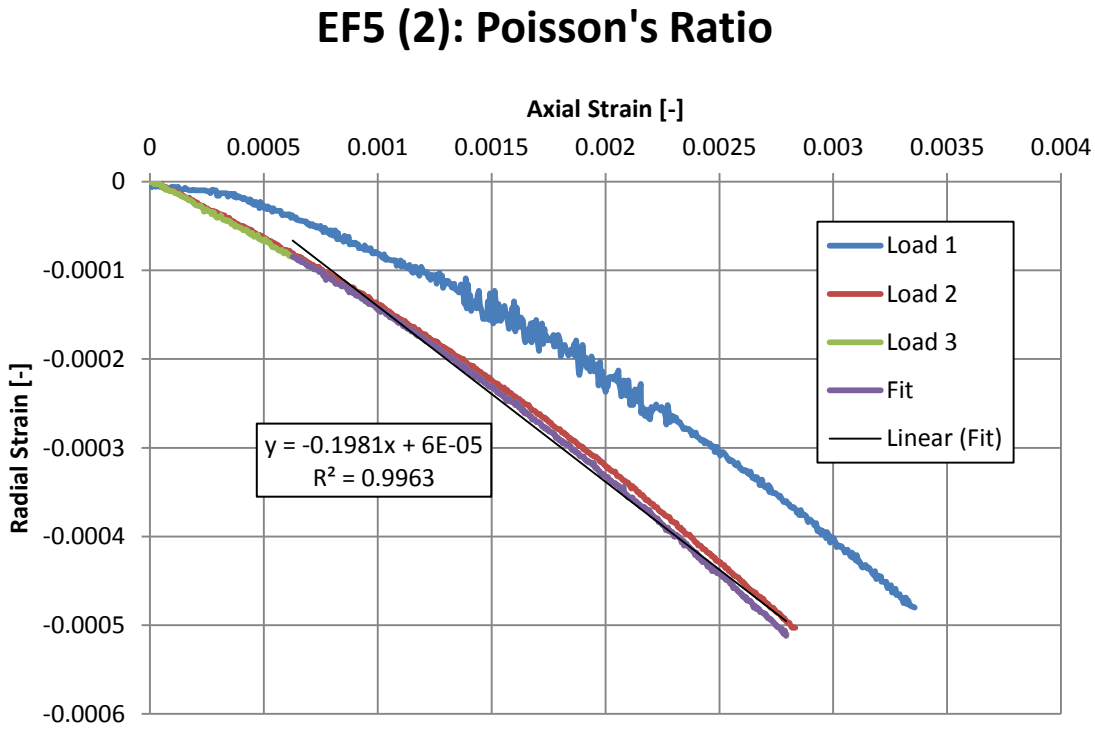
EF5 (2): Poisson's Ratio
y = -0.1981x + 6E-05
R² = 0.9963
Radial Strain [-]
Axial Strain [-]
Load 1
Load 2
Load 3
Fit
Linear (Fit)

EF6 Results

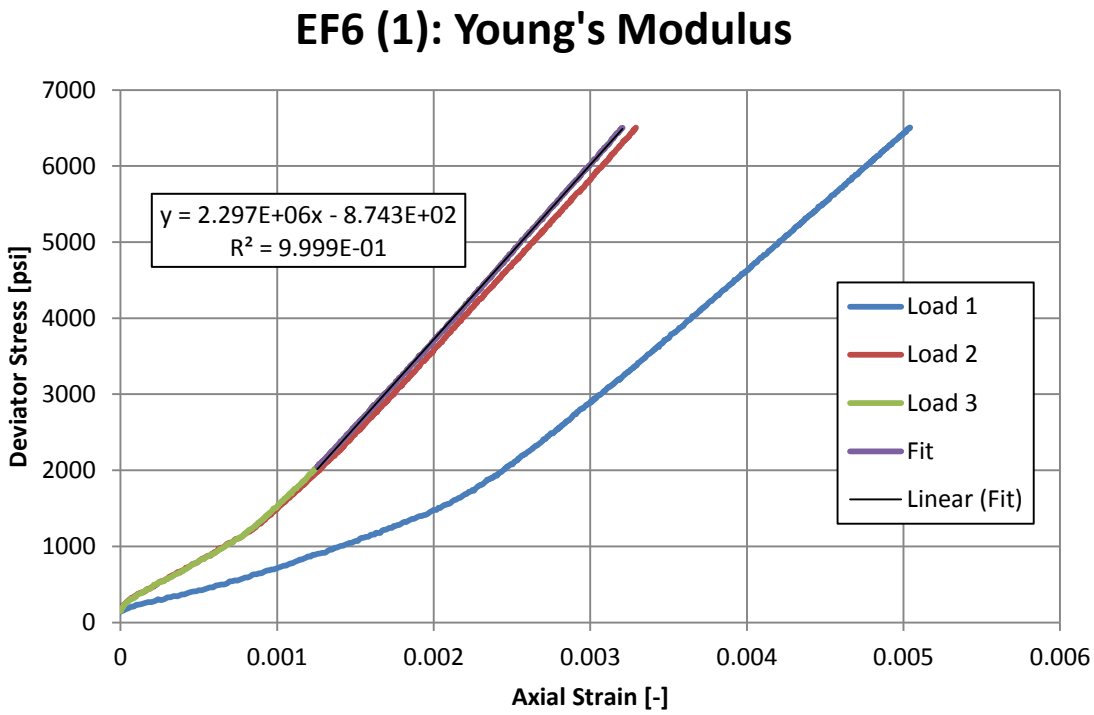
EF6 (1): Young's Modulus
y = 2.297E+06x - 8.743E+02
R² = 9.999E-01
Deviator Stress [psi]
Axial Strain [-]
Load 1
Load 2
Load 3
Fit
Linear (Fit)

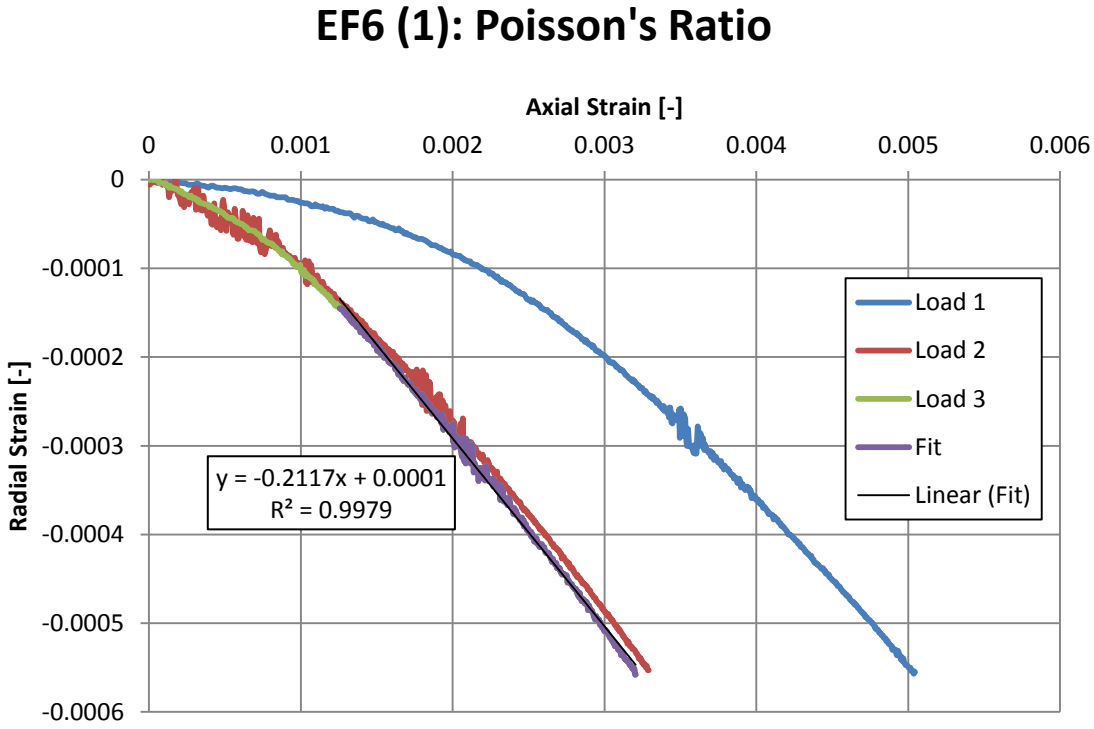
EF6 (1): Poisson's Ratio
Axial Strain [-]
Radial Strain [-]
y = -0.2117x + 0.0001
R² = 0.9979
Load 1
Load 2
Load 3
Fit
Linear (Fit)

EF6 (2): Young's Modulus

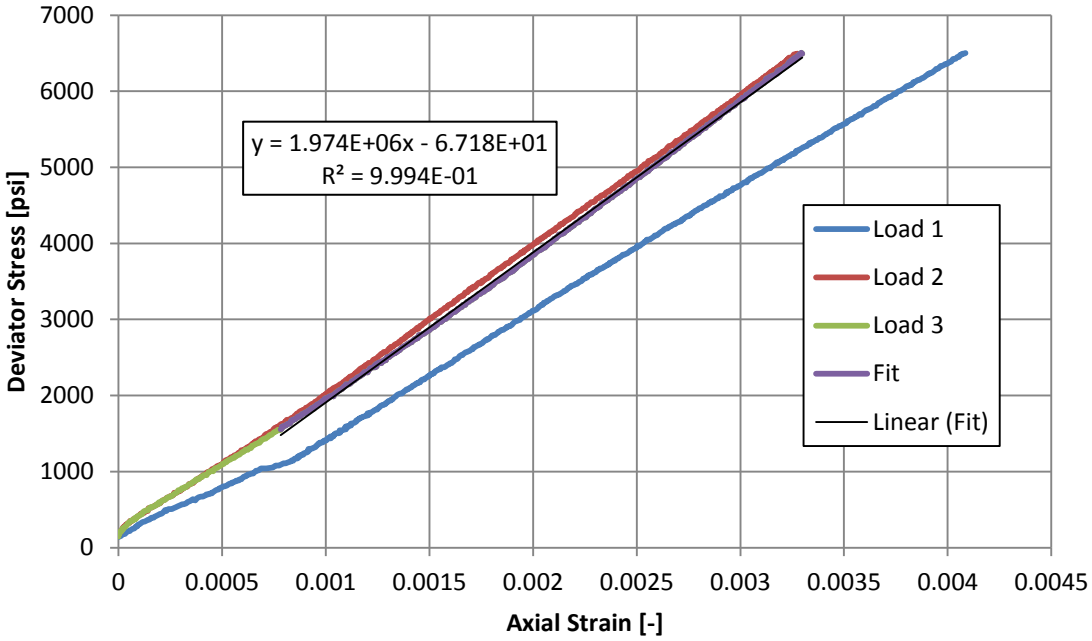

EF6 (2): Poisson's Ratio

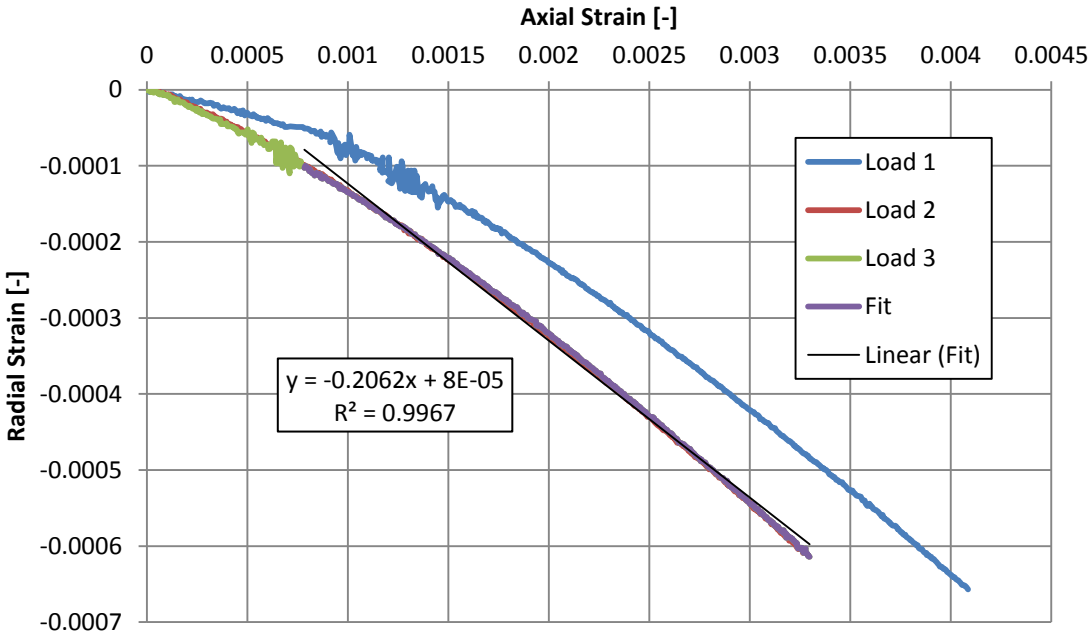

EF7 Results

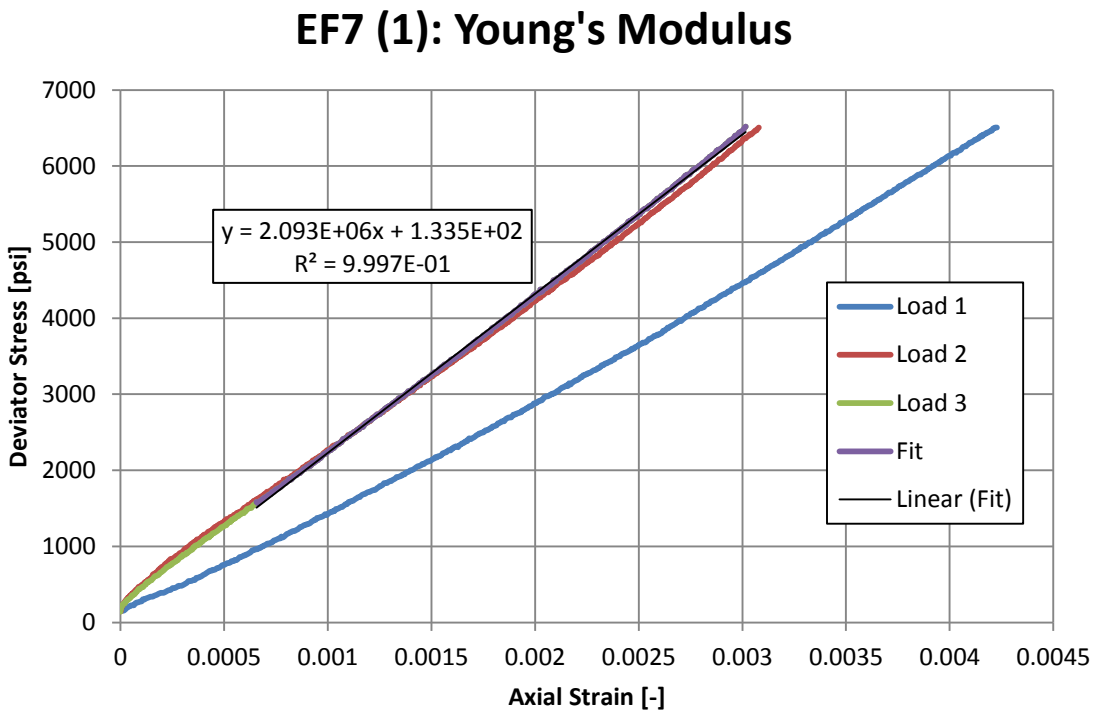
EF7 (1): Young's Modulus
Deviator Stress [psi]
Axial Strain [-]
y = 2.093E+06x + 1.335E+02
R² = 9.997E-01
Load 1
Load 2
Load 3
Fit
Linear (Fit)
0
1000
2000
3000
4000
5000
6000
7000
0
0.0005
0.001
0.0015
0.002
0.0025
0.003
0.0035
0.004
0.0045

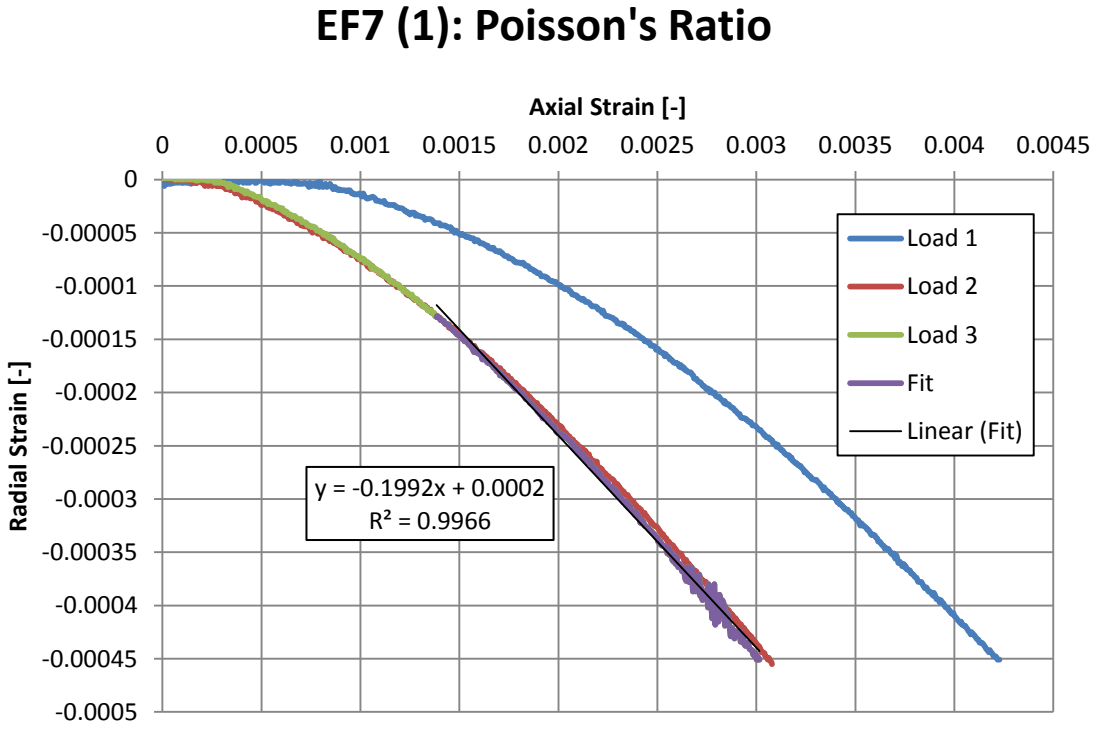
EF7 (1): Poisson's Ratio
Radial Strain [-]
Axial Strain [-]
y = -0.1992x + 0.0002
R² = 0.9966
Load 1
Load 2
Load 3
Fit
Linear (Fit)
0
-0.00005
-0.0001
-0.00015
-0.0002
-0.00025
-0.0003
-0.00035
-0.0004
-0.00045
-0.0005
0
0.0005
0.001
0.0015
0.002
0.0025
0.003
0.0035
0.004
0.0045

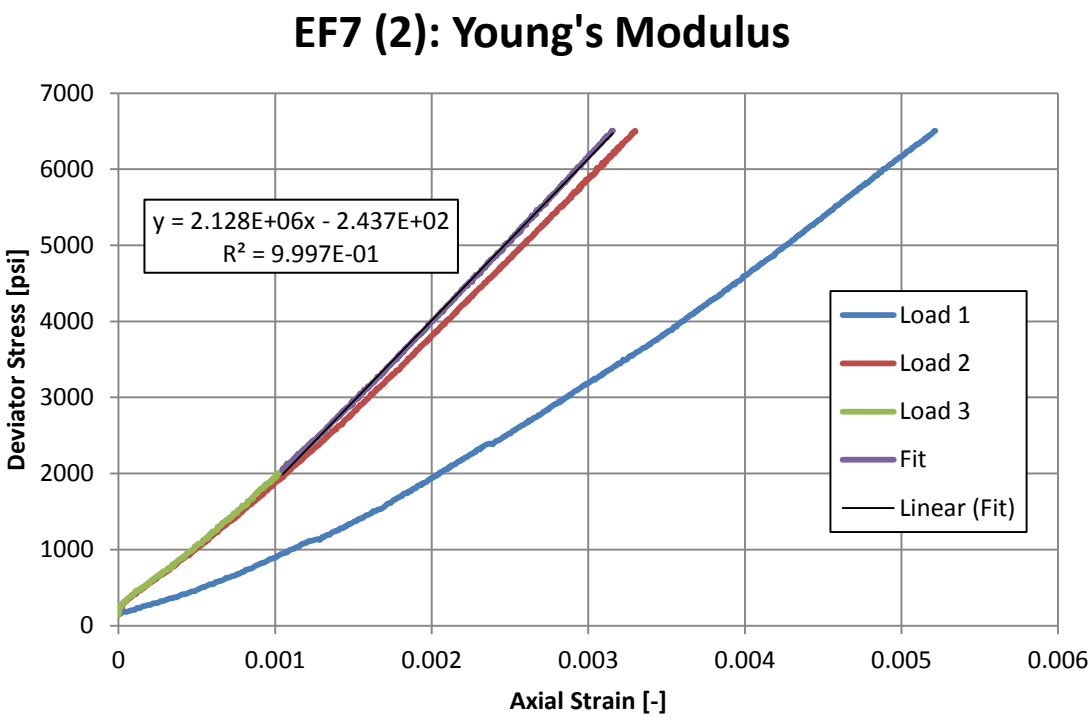
EF7 (2): Young's Modulus
y = 2.128E+06x - 2.437E+02
R² = 9.997E-01
Deviator Stress [psi]
Axial Strain [-]
Load 1
Load 2
Load 3
Fit
Linear (Fit)
7000
6000
5000
4000
3000
2000
1000
0
0
0.001
0.002
0.003
0.004
0.005
0.006

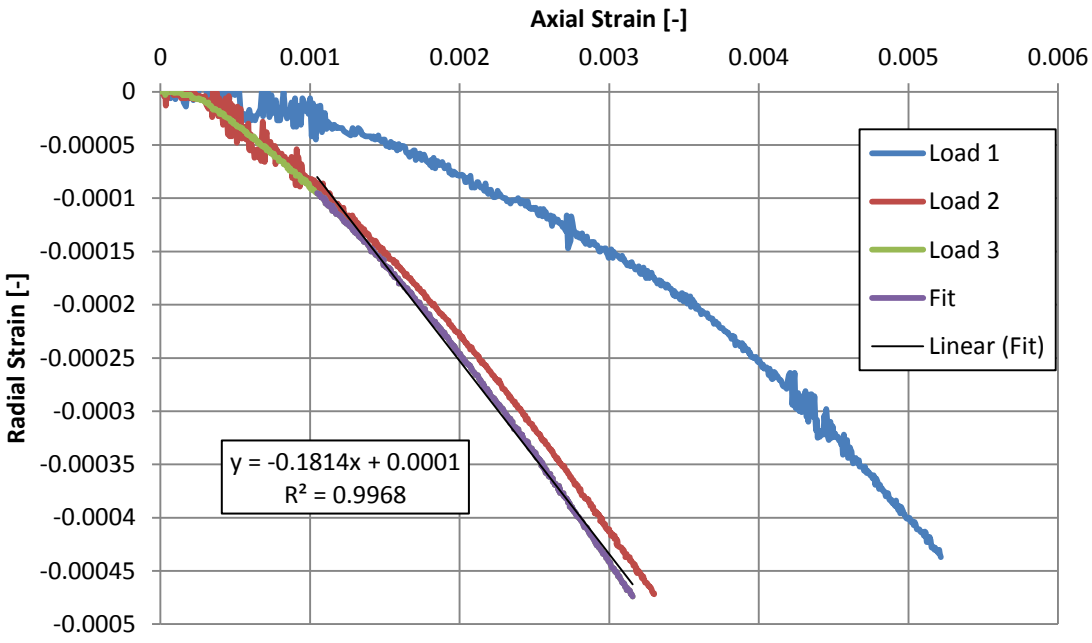
EF7 (2): Poisson's Ratio
Axial Strain [-]
Radial Strain [-]
y = -0.1814x + 0.0001
R² = 0.9968
Load 1
Load 2
Load 3
Fit
Linear (Fit)
0
-0.00005
-0.0001
-0.00015
-0.0002
-0.00025
-0.0003
-0.00035
-0.0004
-0.00045
-0.0005
0
0.001
0.002
0.003
0.004
0.005
0.006

APPENDIX B

COMPLETE FAYETTEVILLE SHALE FL2 MECHANICAL RESULTS

FL2 (1): Young's Modulus

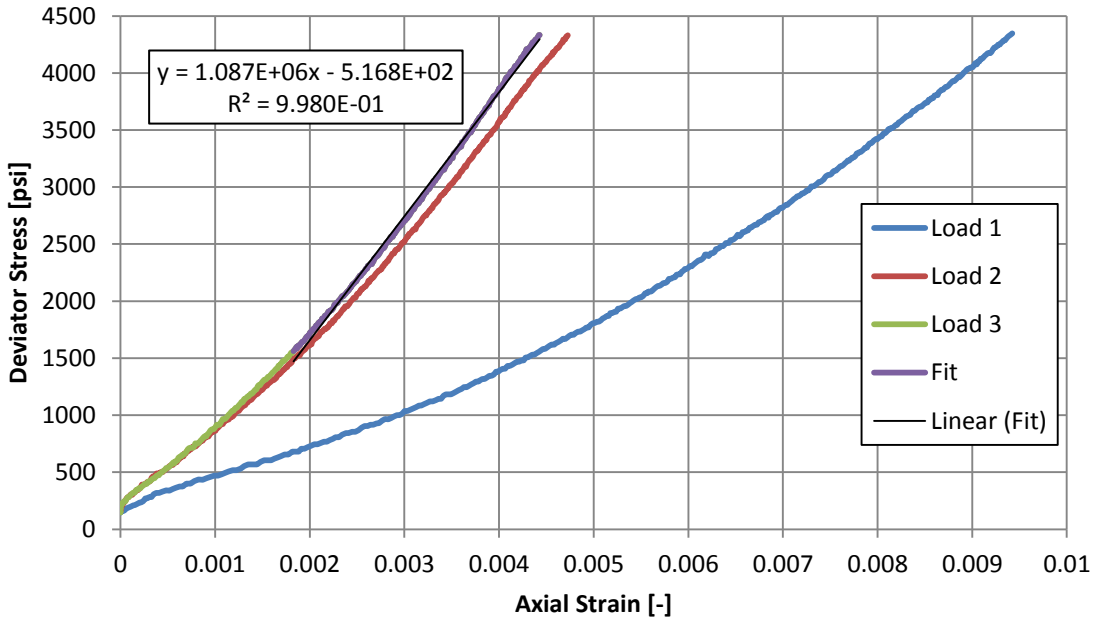

FL2 (1): Poisson's Ratio

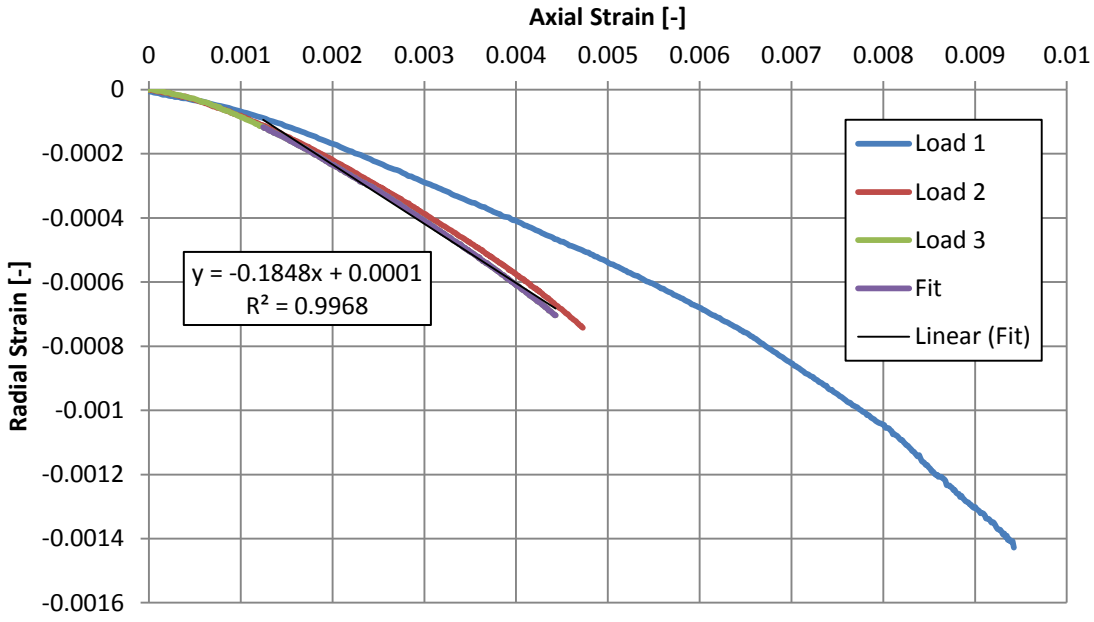

FL2 (2): Young's Modulus

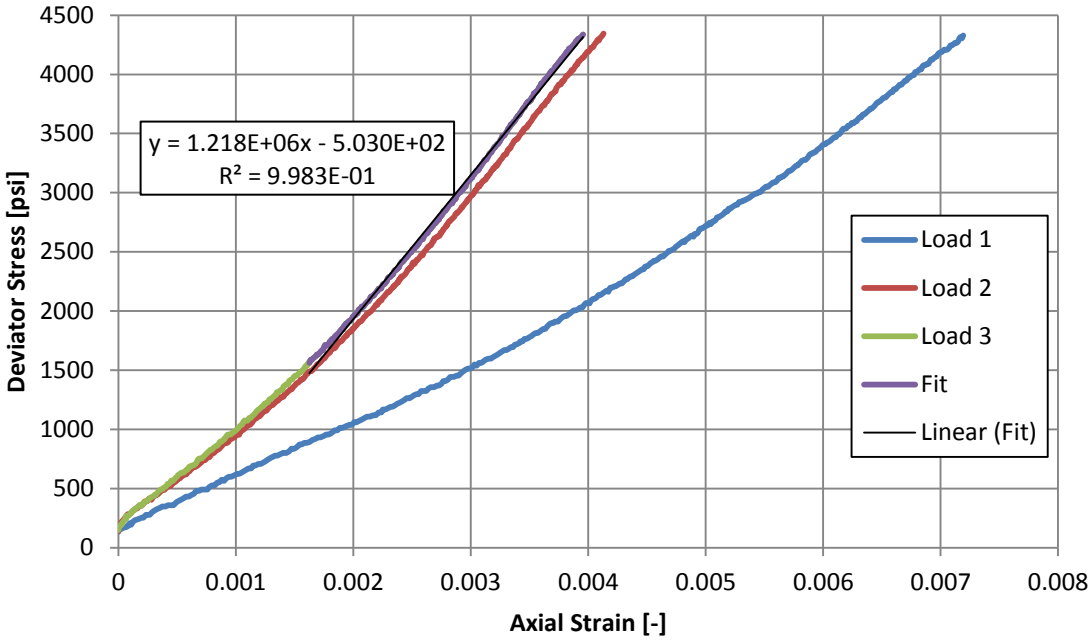

FL2 (2): Poisson's Ratio

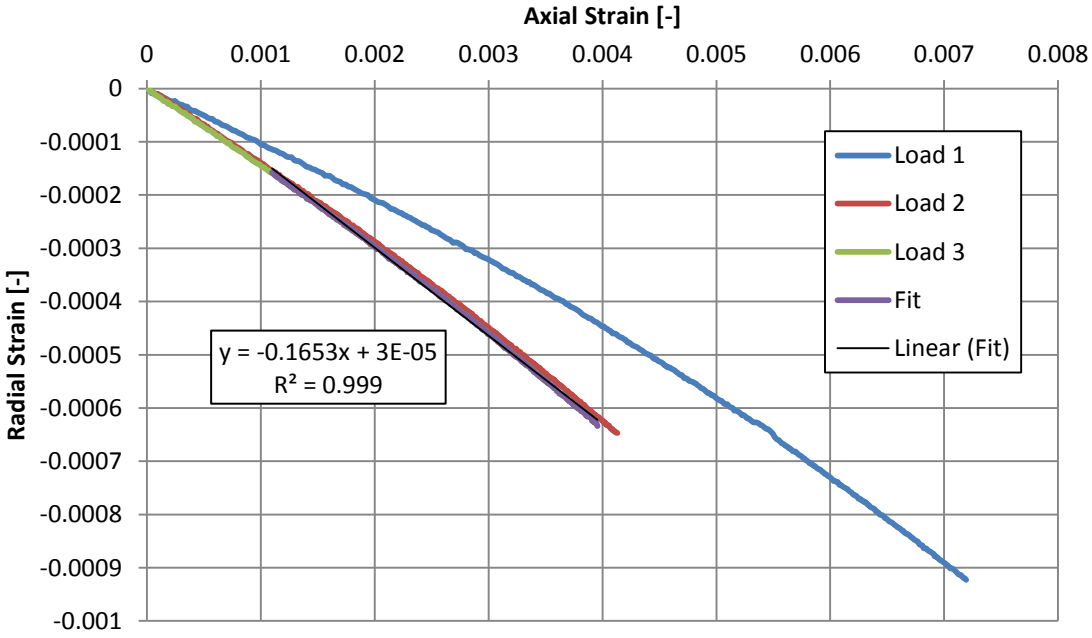

FL2 (3): Young's Modulus

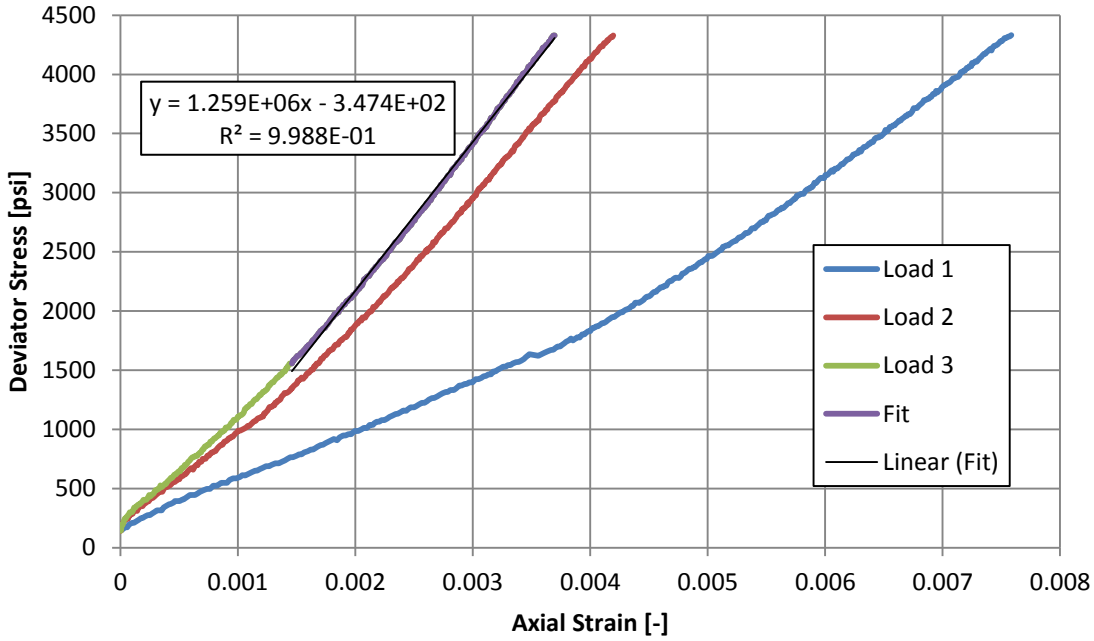

FL2 (3): Poisson's Ratio

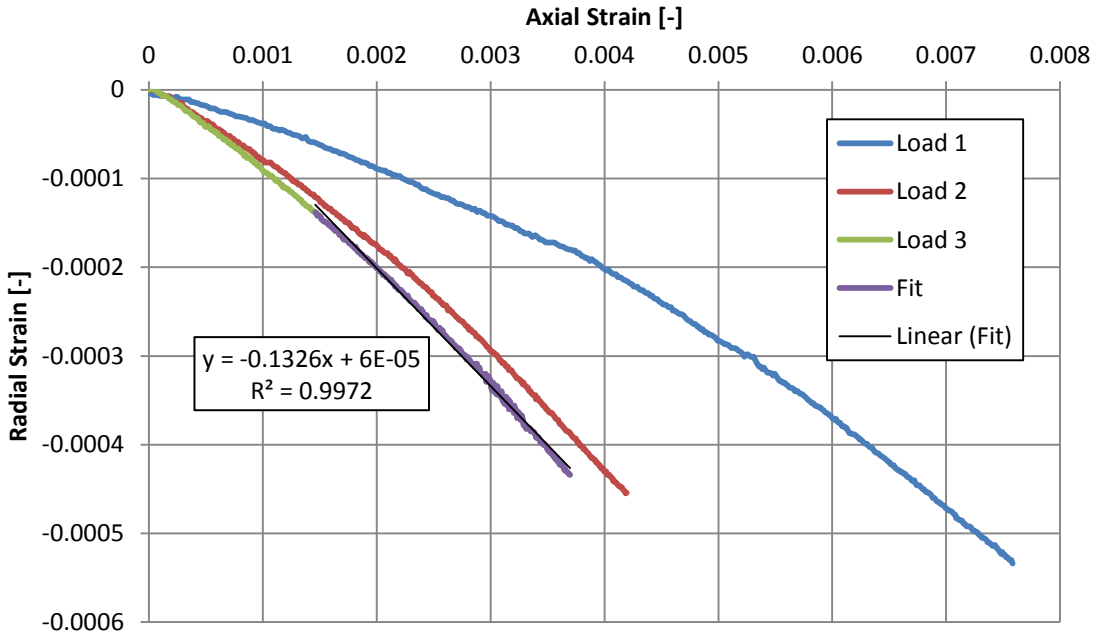

APPENDIX C

COMPLETE FAYETTEVILLE FL3 MECHANICAL RESULTS

FL3 (1): Young's Modulus

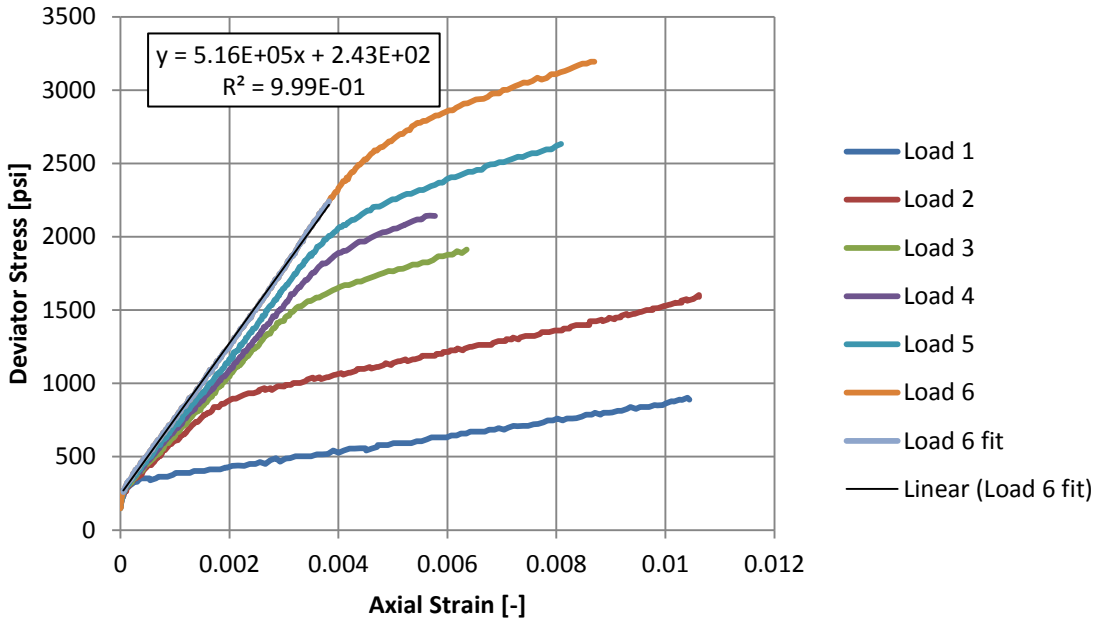

FL3 (1): Poisson's Ratio

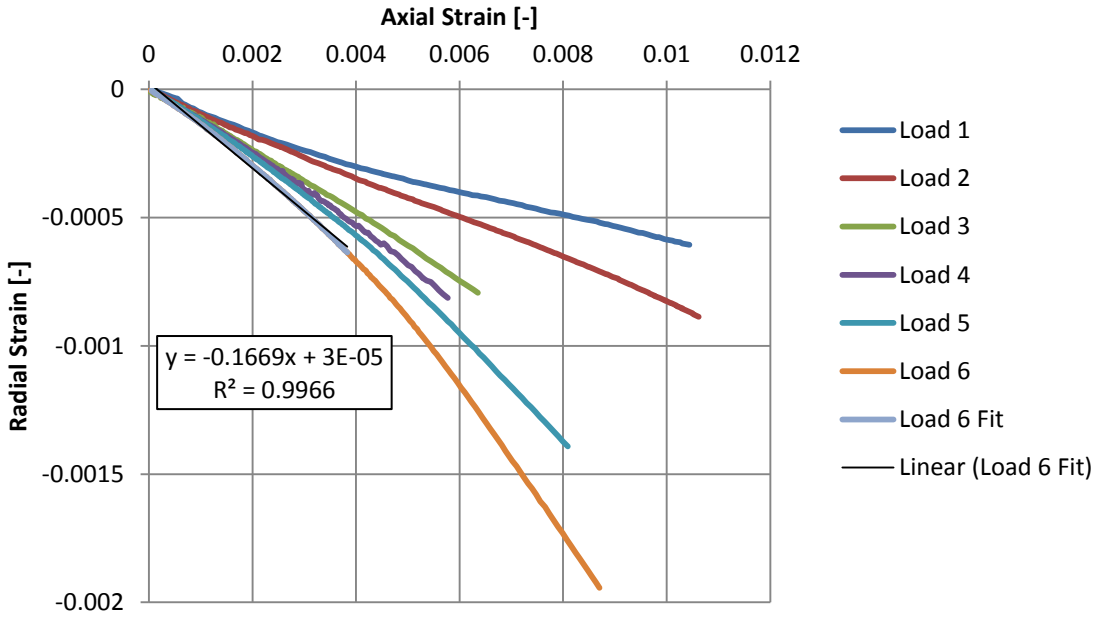

FL3 (2): Young's Modulus

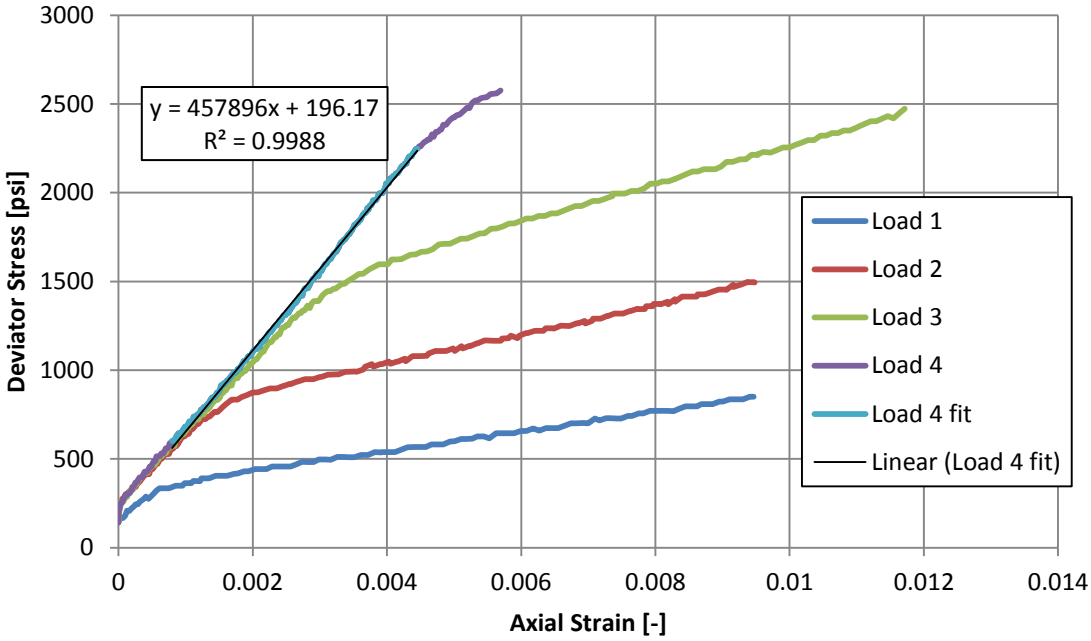

FL3 (2): Poisson's Ratio